

# **Solidification study of commercial magnesium alloys**

Mohammad Nazmul Khan

A Thesis  
in

The Department  
of  
Mechanical and Industrial Engineering

Presented in Partial Fulfillment of the Requirements  
for the Degree of Master of Applied Science (Mechanical Engineering) at  
Concordia University  
Montreal, Quebec, Canada

October 2009

© Mohammad Nazmul Khan, 2009

# **ABSTRACT**

Solidification study of commercial magnesium alloys

Mohammad Nazmul Khan

In this thesis, the solidification behavior of AZ91D, AM60B and AE44 commercial magnesium alloys has been studied experimentally by differential scanning calorimeter (DSC) and optical microscopy. The effect of different cooling rates on the transition temperatures and microstructures were analyzed. It was found that the effect of cooling rate on the solidus temperature is more significant than on the liquidus. The solidus temperature decreases clearly with increasing cooling rates, but for the liquidus temperature there is slightly increasing trend. The latent heat of solidification was also calculated and found that it increases when the cooling rate increases. Thermodynamic calculations were made using FactSage along with VLGM database and were compared with the experimental findings as well as with the literature data. Thermodynamic calculations were also utilized to understand the microstructures as well as the phase distribution. The microstructural details of as-cast and post-DSC samples have also been investigated using optical microscope. Finally, a relationship between cooling rate and transition temperature and solidification enthalpy has been established based on the general power law. Using this relationship it is possible to predict the transition temperatures and solidification enthalpies of these alloys at high cooling rates.

## ACKNOWLEDGEMENTS

First and foremost I would like to express my sincere gratitude and appreciations to my supervisor Dr. Mamoun Medraj without whom this thesis would not have seen the light. His cool and optimistic attitude towards my research progress was always encouraging. I would like to thank Dr. Jeff Wood, my co-supervisor at University of Western Ontario, for his continuous support and helpful discussion.

The financial support from the AUTO21 is gratefully acknowledged. I am also thankful to Meridian Technologies for their support. I would also like to thank all the members of Dr. Medraj's research group, especially Mohammad Aljarrah, for the kind help and cooperation.

Finally, I would like to thank my mother for her love, support and constant encouragement. Last but not least, I would like to thank my wife, Johora for her invaluable support and encouragement.

# Table of content

List of figures.....	vii
List of tables.....	xi
Chapter 1: Introduction.....	1
1.1 Objectives.....	5
Chapter 2: Literature review.....	6
2.1 Magnesium and Magnesium alloys.....	6
2.2 Magnesium alloys designation.....	11
2.3 Commercial Mg alloys.....	12
2.4 Solidification study .....	14
2.5 Solidification characteristics of Mg alloys.....	17
2.6 Thermal Analysis Technique.....	22
2.6.1 DTA/DSC.....	22
2.6.2 Principle of DSC.....	24
2.6.2.1 Power compensated DSC.....	25
2.6.2.2 Heat Flux DSC.....	26
2.6.3 DSC Signal interpretation.....	27
2.6.4 Heat Transfer Model (HTM).....	28

Chapter 3: Methodology.....	31
3.1 Approach.....	31
3.2 Thermal Analysis using DSC.....	31
3.3 Metallography.....	33
3.4 Thermodynamic Calculation.....	34
3.5 Analytical Model for Extrapolation to Higher Cooling Rate.....	35
 Chapter 4: Result and Discussion.....	 36
4.1 Thermal analysis results.....	36
4.1.1 Experimental Results of AZ91D alloy.....	36
4.1.2 Experimental Results of AM60B alloy.....	41
4.1.3 Experimental Results of AE44 alloy.....	45
4.1.4 Latent Heat of Solidification .....	50
4.2 Thermodynamic calculation.....	51
4.2.1 Calculation of Solidification Curve.....	51
4.2.2 Phase Distribution of the Alloys.....	58
4.3 Microstructural analysis.....	68
4.3.1 AZ91D.....	67
4.3.2 AM60B.....	71
4.3.3 AE44.....	74
4.4 Extrapolation of the Latent Heat of Solidification and Phase Transition Temperatures.....	 77

Chapter 5: Conclusions, Contribution and Recommendation for Future Work.....	83
5.1 Conclusions.....	83
5.2 Contributions.....	84
5.3 Recommendation for Future Work.....	84
References.....	86

## Lists of Figure

Figure 1	Fuel economy versus vehicle weight	2
Figure 2	Mg-Al binary phase diagram	9
Figure 3	Effect of aluminum content on ductility. Sand cast sample, as cast condition	10
Figure 4	Effect of Al content on grain size of pure Mg	10
Figure 5	Liquidus temperature vs. cooling rate for three different alloys	15
Figure 6	Phase transformation temperature at different cooling rates	15
Figure 7	Plot of primary $\alpha$ -Al, Primary eutectic, Mg <sub>2</sub> S <sub>1</sub> and solidus temperature in AA5182 at different cooling rates	16
Figure 8	The effect of scanning rate on the latent heat of pure Co	17
Figure 9	Fraction solidified as a function of temperature, Mg-Al alloys	18
Figure 10	(a) Lamellar, (b) fibrous, (c) partially divorced and (d) fully divorced morphologies in Mg-Al alloys of various compositions	19
Figure 11	DTA scan for melting and freezing at 5K/min for Ag-15% Cu under equilibrium condition. Label 'i' indicates 'important' and 'n' indicates 'not important'	23
Figure 12	The principle of power compensated Differential Scanning Calorimeter Analysis	25
Figure 13	The principle of heat flux Differential Scanning Calorimeter Analysis	26
Figure 14	Definition of zero line, baseline, and characteristic temperatures	28
Figure 15	Schematic view of a heat flux DSC, with quantities used in the heat transfer model	29
Figure 16	Flow chart illustrating the methodology of the current work	33

Figure 17	A DSC spectra for AZ91D at 5°C/min scanning rate	37
Figure 18	DSC spectra of AZ91D alloy at different cooling rates (after subtraction the baseline)	37
Figure 19	Transformation temperature of AZ91D at different cooling rates	39
Figure 20	Solidification curve of AZ91D at different cooling rates drawn from the experimental data using HTM	40
Figure 21	A DSC spectra for AM60B at 5°C/min scanning rate	41
Figure 22	DSC spectra of AM60B alloy at different cooling rates after subtraction the baseline	42
Figure 23	Transformation temperature of AM60B at different cooling rates	44
Figure 24	Solidification curve of AM60B drawn from the experimental data using HTM	45
Figure 25	A DSC spectra of the AE44 alloy at 5°C/min scanning rate	46
Figure 26	DSC spectra of AE44 alloy at different cooling rate after subtracting the baseline	46
Figure 27	Transformation temperature of AE44 at different cooling rate	48
Figure 28	Solidification curve of AE44 drawn from the experimental data using HTM	49
Figure 29	Change of Latent Heat of Solidification of the alloys at different cooling rates	50
Figure 30	Comparison between experimental and calculated solidification curves of AZ91D alloy	52
Figure 31	Comparison between experimental and calculated transition temperatures of AZ91D alloy	53

Figure 32	Comparison between experimental and calculated solidification curves of AM60B alloy	54
Figure 33	Comparison between experimental and calculated transition temperatures of AM60B alloy	55
Figure 34	Comparison between experimental and calculated solidification curves of AE44 alloy	56
Figure 35	Comparison between experimental and calculated transition temperatures of AE44 alloy	57
Figure 36	Equilibrium phase distribution of AZ91D alloy	59
Figure 37	Scheil phase distribution of AZ91D alloy	60
Figure 38	Equilibrium phase distribution of AM60B alloy	62
Figure 39	Scheil phase distribution of AM60B alloy	63
Figure 40	Equilibrium phase distribution of AE44 alloy	64
Figure 41	Scheil phase distribution of AE44 alloy	65
Figure 42	(a)(b)(c): AS cast microstructure of AZ91D (d)(e)(f): Post-DSC microstructure of AZ91D, DSC cooling rate 5°C/min	69
Figure 43	(a)(b)(c): Post-DSC microstructure of AZ91D, DSC cooling rate 25°C/min; (d)(e)(f): Post-DSC microstructure of AZ91D, DSC cooling rate 45°C/min	70
Figure 44	(a)(b)(c)(d): AS cast microstructure of AM60B	72
Figure 45	(a)(b)(c)(d): Post-DSC microstructure of AM60B, DSC cooling rate 5°C/min	73
Figure 46	(a)(b)(c)(d): Post-DSC microstructure of AM60B, DSC cooling rate	74

45°C/min

Figure 47	(a)(b)(c): As cast microstructure of AE44, Figure 44(d)(e)(f): Post-DSC microstructure of AE44, DSC cooling rate 5°C/min	75
Figure 48	(a)(b): Post-DSC microstructure of AE44, DSC cooling rate 10°C/min	76
Figure 49	(a)(b): Post-DSC microstructure of AE44, DSC cooling rate 20°C/min	76
Figure 50	Extrapolation of latent heat of solidification of AZ91D to high cooling rate in double logarithmic graph	78
Figure 51	Extrapolation of latent heat of solidification of AM60B to high cooling rate in double logarithmic graph	79
Figure 52	Extrapolation of latent heat of solidification of AE44 to high cooling rate in double logarithmic graph	79
Figure 53	Extrapolation of transition temperatures of AZ91D to high cooling rate in double logarithmic graph	81
Figure 54	Extrapolation of transition temperatures of AM60B to high cooling rate in double logarithmic graph	82
Figure 55	Extrapolation of transition temperatures of AE44 to high cooling rate in double logarithmic graph	82

## List of Tables

Table 1	Current and potential application of magnesium alloys in vehicles parts	3
Table 2	Physical properties of pure magnesium (99.9 wt %)	6
Table 3	The major alloying elements and their effects in magnesium	8
Table 4	ASTM codes for magnesium's alloying elements	12
Table 5	The nominal composition of the alloys	13
Table 6	Liquidus and solidus temperature of AZ91 alloy under different cooling rates	21
Table 7	DSC experimental conditions	32
Table 8	Transition temperatures and latent heat of solidification of AZ91D alloy	38
Table 9	Experimental solidification sequence of AZ91D alloy	40
Table 10	Transition temperatures and latent heat of solidification of AM60B alloy	43
Table 11	Experimental solidification sequence of AM60B alloy	45
Table 12	Transition temperatures and latent heat of solidification of AE44 alloy	47
Table 13	Experimental solidification sequence of AE44 alloy	49
Table 14	Sequence of Phase formation during equilibrium and Scheil solidification of AZ91D alloy	60
Table 15	Sequence of Phase formation during equilibrium and Scheil solidification of AM60B alloy	63
Table 16	Sequence of Phase formation during equilibrium and Scheil solidification of AE44 alloy	65
Table 17	Equilibrium solidification simulation results of the alloys	66

Table 18	Scheil solidification simulation results of the alloys	66
Table 19	The scaling parameters of latent heat of solidification	78
Table 20	Liquidus temperature extrapolation parameters	80
Table 21	Solidus temperature extrapolation parameters	80

# CHAPTER 1

## *Introduction*

---

Energy crisis and global warming are the two most common challenges for present-day scientists. In a report of Agency for Natural Resources and Energy in 2004, it was mentioned that passenger transports are responsible for about 60% of total energy consumption in the transport sector, and particularly the use of private cars contributed significantly to annual energy consumption [1]. Figure 1 illustrates the relationship between vehicle weight and fuel consumption. The transportation industry is one of the major sources of environmental pollution, particularly the CO<sub>2</sub> emission produced by the vehicles. Hence, the North American and European car producers have committed themselves to reduce CO<sub>2</sub> emission through decreasing the fuel consumption of vehicles [2]. Therefore, reducing the weight of the structural materials used in transport equipment is a big challenge for the automobile manufacturers for a sustainable society in the future. According to Friedrich and Schumann [3] if the weight of a vehicle is reduced by 10%, it can bring a drop in the fuel consumption of roughly by 5%, provided that engine and gearbox performance are properly adapted. All these are the driving forces to search for a lighter material for the automotive industry.

Magnesium is the lightest structural metal, resulting in high specific strength and stiffness, therefore, very attractive for the automotive industry [4]. Magnesium also has a number of other desirable features including strong abilities for vibration damping and noise reduction, excellent liquid state formability and radiation insulation. Hence it is recognized as an environmental

friendly engineering metal [5]. Therefore, magnesium alloys are becoming popular in the automobile industry as a means of reducing weight, increasing fuel efficiency and decreasing greenhouse gas emissions.

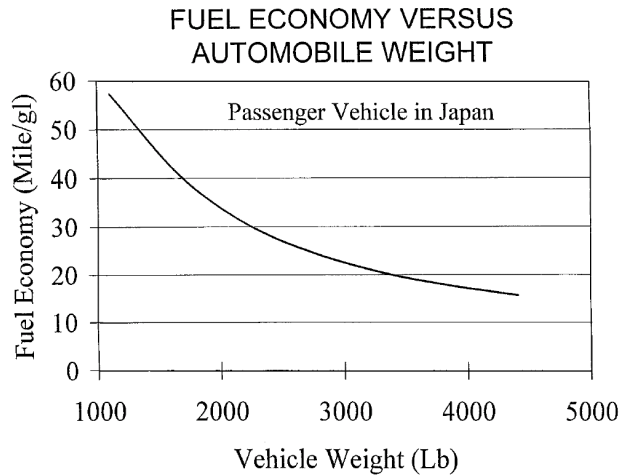


Figure 1: Fuel economy versus vehicle weight [7]

At present, enterprises in the automobile industry around the world have applied magnesium alloys in more than 100 types of die-casting parts, which has become the major driving force in the growth of the application of magnesium alloys [2]. The growth rate for automotive magnesium components has averaged 18% per annum since the year 1990. The usage of magnesium reaches 4.3 kg per vehicle in 2001 from less than 1 kg per vehicle in 1990 [6]. Ford, General Motors (GM) and DaimlerChrysler, the Big Three in the automotive industry, are motivated to increase the use of magnesium to exceed 100 kg per vehicle by 2020 from the current level [5]. The current magnesium components, including instruments panels, steering wheel armatures, steering column supports, seats, valve covers, and transfer cases, are mainly manufactured with the conventional magnesium alloys. A list of parts that are currently produced using magnesium alloys or potentially could be produced given in Table 1.

Magnesium alloys components are usually produced by various casting processes. Magnesium casting processes may be divided into three major groups: sand casting, permanent mold casting and high-pressure die-casting. Similar to other commonly cast materials; selection of casting processes is determined by the size, required tolerance, and quantity.

Table 1: Current and potential application of magnesium alloys in vehicles parts [2]

Engine and transmission (drive train) parts	Interior parts	Chassis components	Body Components
<ul style="list-style-type: none"> <li>-Gear box</li> <li>-Intake Manifold</li> <li>-Crankcase</li> <li>-Cylinder head cover</li> <li>-Oil pump housing</li> <li>-Oil sump</li> <li>-Transfer case</li> <li>-Support</li> </ul>	<ul style="list-style-type: none"> <li>-Steering wheel cores</li> <li>-Seat components, rear seat</li> <li>-Instruments panel</li> <li>-Steering column components</li> <li>-Brake and clutch pedal brackets</li> <li>-Air bag retainer</li> </ul>	<ul style="list-style-type: none"> <li>-Road wheels</li> <li>-Suspension arms (front and rear)</li> <li>-Engine cradle</li> <li>-Rear support</li> </ul>	<ul style="list-style-type: none"> <li>-Inner bolt lid section</li> <li>-Cast door inner</li> <li>-Cast A/B pillars</li> <li>-Sheet components</li> <li>-Extruded component</li> </ul>

The most common casting method for magnesium alloys production is high pressure die casting (HPDC). HPDC is a fully automatic, large volume, high productivity process for the production of complex, thin walled near-net-shape castings, with part weights ranging from a few grams to more than 15kg [4, 8]. During HPDC the mold is filled rapidly (5 to 100m/s) by forcing the molten metal through a narrow gate [9]. The metal solidifies with a high cooling rate (100 to 1000°C/s), resulting in a fine grained microstructure. HPDC has traditionally been utilized in the production of gear box housings, steering wheel frame, sealing flange etc; but presently feasible products manufactured are complex automotive front-end structures and instruments panels etc. [8, 9].

Solidification is a crucial stage of casting production. It has been studied for many years for practical reasons. Fundamental knowledge of solidification characteristics and of the resulting microstructure is a prerequisite to understand the mechanical behavior of the component. Controlling the as-solidified microstructure often provides the alloy designer with the greatest influence over the final alloy performance and should be considered paramount to the intelligent, rapid design of improved alloys. Much of this knowledge is yet to be discovered, therefore, the researchers are working on it with appropriate research equipments designed for studying solidification, microstructure and microstructure evolution [10]. So far, a large variety of solidification analyzing techniques has been developed. Calorimetric techniques are most suitable for the solidification study [11]. Differential Scanning Calorimetry (DSC) is one of the state of the art equipments to study solidification behavior of metals and alloys. In the present work, a Setaram Setsys 1200 DSC has been used for the calorimetric analysis.

Computational thermochemistry, which is based on the CALPHAD (Calculation of Phase Diagram) method, is a current means of obtaining quantitative data to guide the development of alloys or the optimization of materials processing [12]. Through calculating the phase distributions and phase compositions, it facilitates the tracking of individual alloys during solidification. It also allows the simulation of phase transformations during solidification of alloys using the two simple extreme models of solidification: equilibrium solidification and Scheil solidification. In addition, this allows a better understanding of the dissolution of alloying elements in pure metal and phase precipitation at different composition and temperatures [13]. Therefore, in this research a thermodynamic software, FactSage [18] along with VLGM database, a recent magnesium alloy database, has been used to characterize the solidification

behavior of magnesium based alloys. Comparisons have been made between the thermodynamic predictions and experimental results to increase the understanding of the magnesium alloys solidification.

## **1.1 Objectives**

With the intension of understanding the casting behavior of the magnesium alloys, the aim of this thesis is to study the solidification behavior and resultant microstructure of magnesium based alloys through experimental investigation using DSC, optical microscope as well as thermodynamic prediction of solidification. The alloys analyzed in the present work include the industry dominant AZ91D and AM60B alloys and an experimental alloy, AE44.

Specifically, the objectives of this research are:

- Experimental investigation of the solidification behavior of AZ91D, AM60B and AE44 magnesium alloys at different cooling rates using DSC to determine temperatures and enthalpies of phase transformations.
- Construction of the solidification curves from the experimental data using Heat Transfer Model (HTM)
- Microstructure analysis of as-cast and post-DSC sample using optical microscopy
- Thermodynamic calculation of solidification curves using both equilibrium and Scheil model and comparing the computational with the experimental results
- Calculation of the phases evolution and transition temperatures
- Development of an analytical model for the prediction of transition temperatures and solidification enthalpies at extremely high cooling rates

# CHAPTER 2

## *Literature Review*

---

The following literature survey is focused on solidification, microstructural analysis and thermodynamic calculations performed on magnesium alloys.

### 2.1 Magnesium and Its Alloys

Magnesium is light and fragile in pure form and hardly used as a construction material in pure form. Therefore, magnesium **must be** alloyed with other metals to influence a wide variety of properties, both to increase the manufacturability and the product properties. Table 2 shows the physical properties of pure magnesium.

Table 2: Physical properties of pure magnesium (99.9 wt %) [14]

<b>Property</b>	<b>Value</b>
Melting point	650°C±2
Boiling point	1107°C±10
Latent heat of fusion	0.37 MJ/Kg
Latent heat of evaporation	5.25 MJ/Kg
Heat of combustion	25.1 MJ/Kg
Specific heat at 20°C	1030 J/(kg K)
Specific heat at 600°C	1178 J/(kg K)
Electrical resistivity at 20°C	4.45 μΩ cm
Thermal conductivity at 25°C	155 W/(kg K)
Linear coefficient of thermal expansion at 20°C	25.2*10 <sup>-6</sup> K <sup>-1</sup>
Density	

at 20°C	1.738 g/cm <sup>3</sup>
at 600°C	1.622 g/cm <sup>3</sup>
at 650°C (solid)	1.65 g/cm <sup>3</sup>
at 650°C (liquid)	1.58 g/cm <sup>3</sup>
Volume change during solidification	4.2%
Volume change during cooling 650°C- 20°C	5%

There are about 25 metals with an appropriate atomic size to form alloys with magnesium, but there is, in reality, few appropriate alloying elements. The solubility is often restricted by the relative valency effect and because of the chemical affinity for elements such as silicon and tin, which leads to the formation of stable compounds [15]. Those elements which dissolve are expected to modify the ductility, the elastic properties and to strengthen the alloy by solid solution hardening. When intermetallics are formed, they restrict the ductility and often such alloys can only be used as casting alloys. The formation of intermetallics can also be exploited to improve the creep resistance providing that the precipitates can form with the right size and distribution. In addition, the precipitation sequence and precipitation process are critical in determining the suitability of an alloy for applications in which creep resistance is necessary. So, there are only about ten elements which can be considered as alloying elements and the favorable alloying elements for the magnesium alloys are aluminum, zinc, manganese, zirconium, silver, yttrium and rare earth elements, in contrast copper, nickel, and iron are considered harmful impurities that need to be controlled properly to insure the quality of magnesium alloys [9]. The major alloying elements and their effects are mentioned in Table 3. Based on the major alloying element, magnesium alloys are normally classified into two types – alloys containing aluminum and alloys containing zirconium. In the current work, some aluminum containing magnesium alloys have been studied.

Table 3: The major alloying elements and their effects in magnesium alloys [9, 15-17]

Aluminum	Provides hardness and strength at room temperature, widens the freezing range and makes the alloy easier to cast
Zinc	Provides strength but increases microporosity, reduces corrosion resistance
Manganese	Helps in offsetting effect of trace element on corrosion and provide toughness. To certain extent reduces micro-galvanic corrosion but at high concentrations affect corrosion resistance
Yttrium	Provides strength, increases corrosion resistance, but expensive
Silver	Provides strength but reduces corrosion resistance
Cerium	Provides moderate elevated temperature properties, helps in castability
Neodymium	Increases elevated temperature properties, assists in castability
Heavy Rare Earths	Improves room and elevated temperature mechanical properties, increases fluidity
Zirconium	Works as a grain refiner

Aluminum is the most commonly used alloying element in Mg alloys and forms the basis of the die-casting alloys. Figure 2 shows the Mg-Al phase diagram. The maximum solubility of aluminum in magnesium ranges from about 2.1 wt.% at 25°C to 12.6 wt.% at the eutectic temperature of 437°C. The eutectic composition is 32.3 wt.% and the eutectic is between  $\alpha$ -(Mg) and the intermetallic  $\gamma$ -phase, which is  $Mg_{17}Al_{12}$ . Hence all the commercial magnesium alloys have aluminum content below the maximum solid solubility and therefore solidify with a primary  $\alpha$ -(Mg) phase [18].

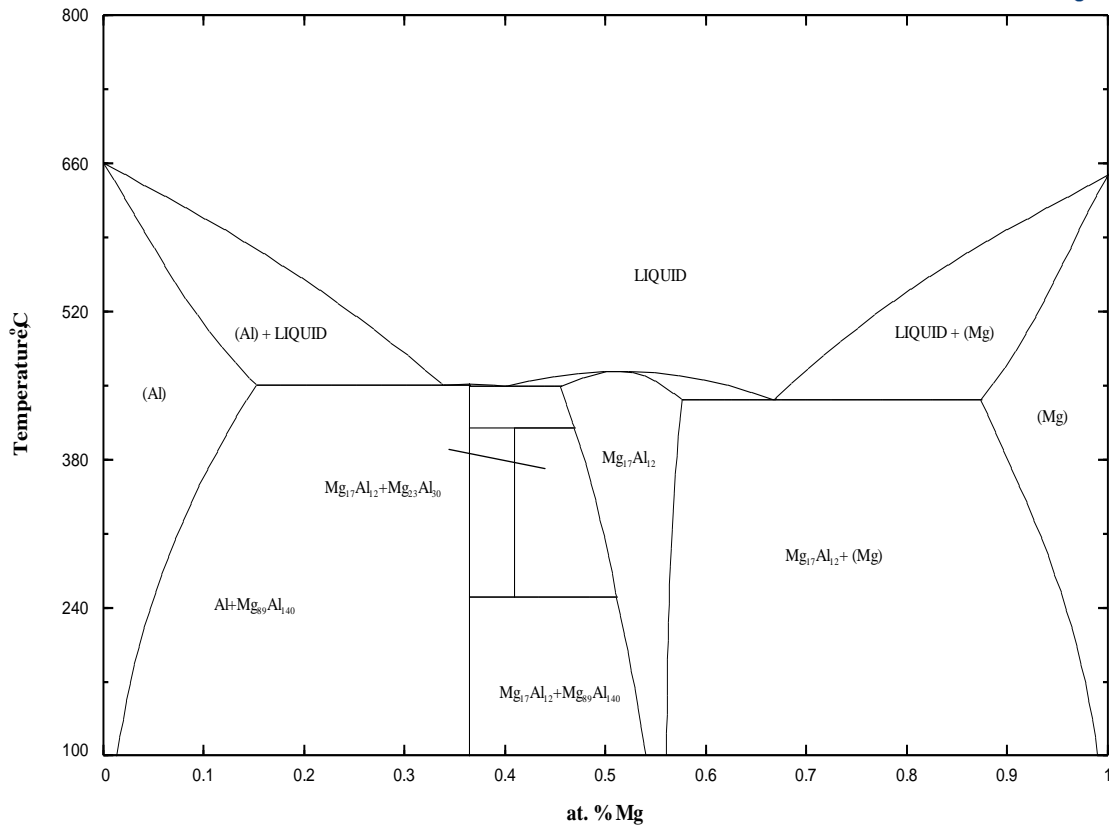


Figure 2: Mg-Al binary phase diagram [19]

According to Beck [21] an aluminum content of 6% yields optimum combination of strength and ductility when the other alloying elements are maintained the same as shown in Figure 3. In addition, aluminum also works as a grain refiner and its grain refining effect is shown in Figure 4.

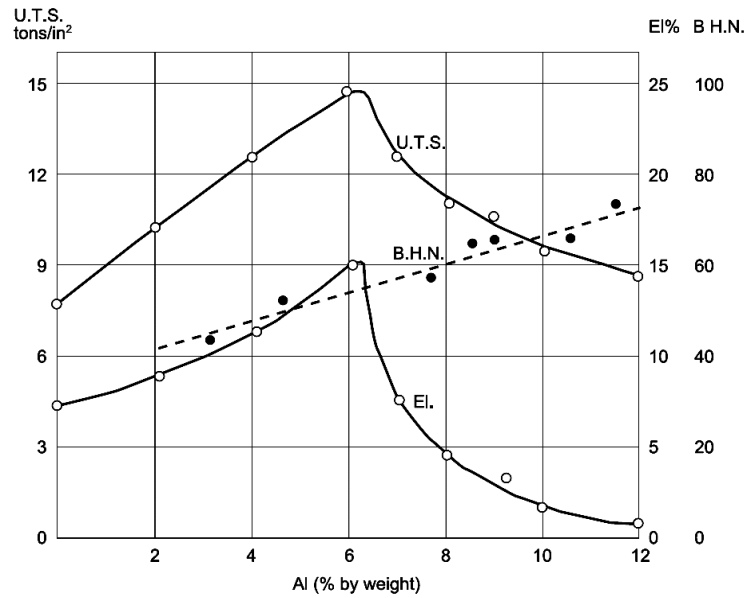


Figure 3: Effect of Al content on ductility (sand cast sample, as cast condition) [21];

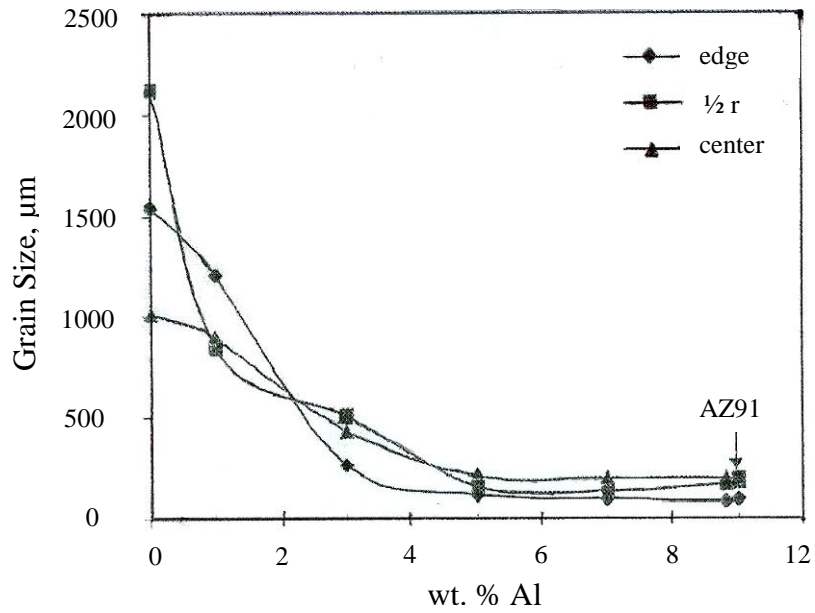


Figure 4: Effect of Al content on grain size of pure Mg [22]

Among the other alloying elements, Manganese is usually not employed alone but with other elements such as Al. In this case compounds such as  $MnAl$ ,  $MnAl_6$  or  $MnAl_4$  are formed [9, 15]. Further, Mn reduces the solubility of iron and produces relatively innocuous compounds as well as increases the yield strength and improves salt water corrosion resistance of Mg-Al and Mg-Al-Zn alloys. Zinc, however, helps in improving room temperature strength, corrosion resistance, and in precipitation hardenability in some alloys [9, 15]. Rare-earth elements, such as cerium, lanthanum, neodymium, gadolinium, and praseodymium, are added to Al containing alloys of magnesium for improved creep resistance as well as to reduce casting porosity [16, 17]. They are added in the form of mischmetal, which has a naturally occurring combination of rare earth elements and is available in the form of lumps of various sizes.

## **2.2 Magnesium Alloys Designation**

The naming method for magnesium alloys has been created and adopted by the American Society for Testing and Materials (ASTM). In this method, the alloys are designated by an alphanumeric code. The two letters are the letter abbreviations given to the two alloying elements with the highest weight percent, and the numbers are the weight percent of these alloying elements rounded to the nearest whole number. A fifth digit is sometimes given and is used to distinguish between alloys that have the same two principal alloying elements with the same concentration. Table 3 lists the abbreviations for the most commonly used alloying elements.

Table 4: ASTM codes for magnesium's alloying elements [9, 10, 23, 24]

Letter Alloying Element	Alloying element	Letter Alloying Element	Alloying element
A	Aluminum	L	Lithium
B	Bismuth	M	Manganese
C	Copper	N	Nickel
D	Cadmium	P	Lead
E	Rare Earths	Q	Silver
F	Iron	R	Chromium
H	Thorium	S	Silicon
J	Strontium	T	Tin
K	Zirconium	W	Yttrium

### 2.3 Commercial Mg Alloys

The most commonly used commercial magnesium alloys for automotive applications are Mg-Al-Zn (AZ) and Mg-Al-Mn (AM) based alloys due to their high strength and elongation, great fracture toughness, and excellent manufacturability, including castability and machinability. In addition, the standardized Mg-Al-Si (AS) and Mg-Al-Re (AE) alloys are also used for their capability of providing improved creep resistance. In the present work, the solidification characteristics and microstructure have been analyzed of three commercial alloys from three different groups. The Mg-Al-Zn alloy AZ91D is the most widely used magnesium die-casting alloy with high strength properties. In addition, excellent pouring characteristics with very good flow and die-filling abilities made AZ91D suitable for standard components in automotive applications. On the other hand, the Mg-Al-Mn alloy AM60B has better elongation and impact

strength than other magnesium alloys. These alloys are substantially used for safety related automotive parts [3]. Mg-Al-Re alloy, AE44 is a new high pressure die casting magnesium alloy, which has attractive high temperature mechanical properties, as well as die castability and corrosion resistance and is being considered for structural components such as automotive front engine cradle [25, 26, 58]. The nominal compositions of these three alloys are mentioned in Table 5.

Table 5: The nominal composition of the alloys (wt%) [9,10,23,24]

<b>Element</b>	<b>AZ91D</b>	<b>AM60B</b>	<b>AE44</b>
Al	8.3%-9.7%	5.5%-6.5%	3.9%-4.1%
Zn	0.35%-1%	0.22% max	0.2%
Mn	0.15% min	0.25%-0.6%	0.25%
Si	0.1% max	0.1% max	-
Fe	0.005% max	0.005% max	-
Cu	0.03 max	0.01% max	-
Ni	0.002% max	0.002% max	-
Rare Earth	-	-	3.95 %-4.2%
Other	0.02% max	0.003% max	-
Mg	Bal.	Bal.	Bal.

## 2.4 Solidification Studies

The growth of a stable phase of material from the unstable liquid phase is called solidification. During solidification, diverse microstructures can appear which influence greatly the mechanical properties of the material. The knowledge of solidification and resultant microstructure is fundamental to the alloy development process. Experimental investigations as well as thermodynamic calculations are two good routes to understand the solidification behavior of the alloys. Although equilibrium phase diagrams are the source for understanding of the phase formation and solidification behavior of alloys, the solidification structure of the casting alloys varies from the prediction of the phase diagram, as most of the commercial casting process involves a wide variety of cooling rates which forces the alloys to solidify under non-equilibrium conditions [27]. For most cases, the Scheil equation [71,72] gives a good description of the process which is based on the assumption that no back diffusion occurs in the solid phases. Diffusion in the liquid phase is very fast so the liquid phase has a uniform composition; an equilibrium occurs at the interface between the liquid and solid states [28,71,72].

Since the cooling rate at real casting process is extremely high, it may affect the transition temperatures and latent heat of solidification. The effect of cooling rates on the transition temperatures for different kind of alloys such as Al, Ni and Cu was studied by many researchers [29-33] and some findings have been shown in the Figures 5 to 7 to get an idea about the effect of cooling rates on metals and alloys. These studies reveal that the transition temperatures, the liquidus and the solidus temperatures, are somewhat influenced by the cooling rates and its effect on the solidus temperature is more than that on the liquidus.

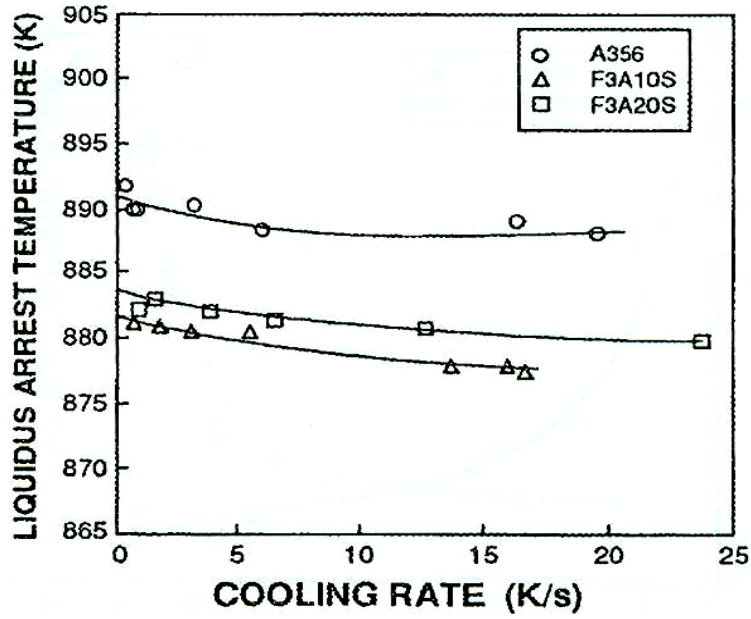


Figure 5: Liquidus temperature vs. cooling rate for three different Al-Si alloys [31]

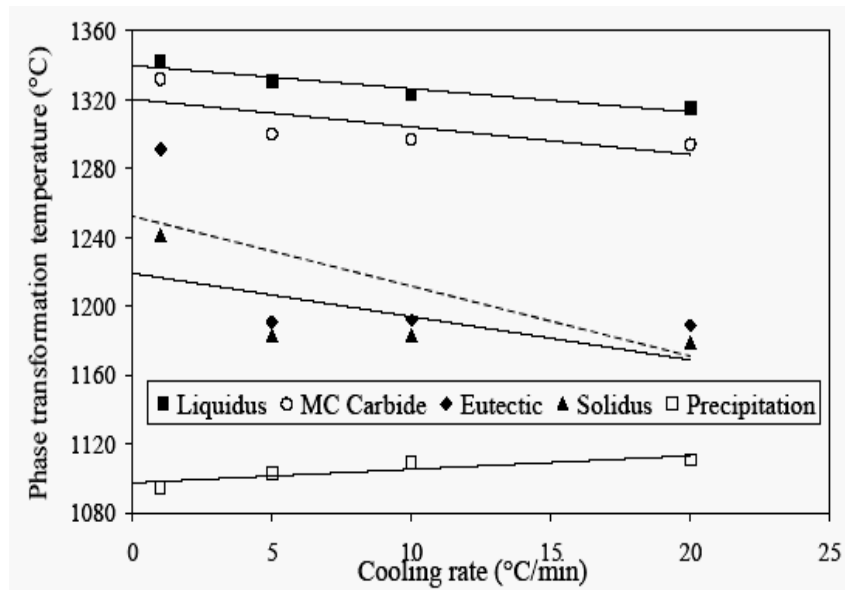


Figure 6: Phase transformation temperatures of Inconel 738LC nickel based super alloy at different cooling rates [35]

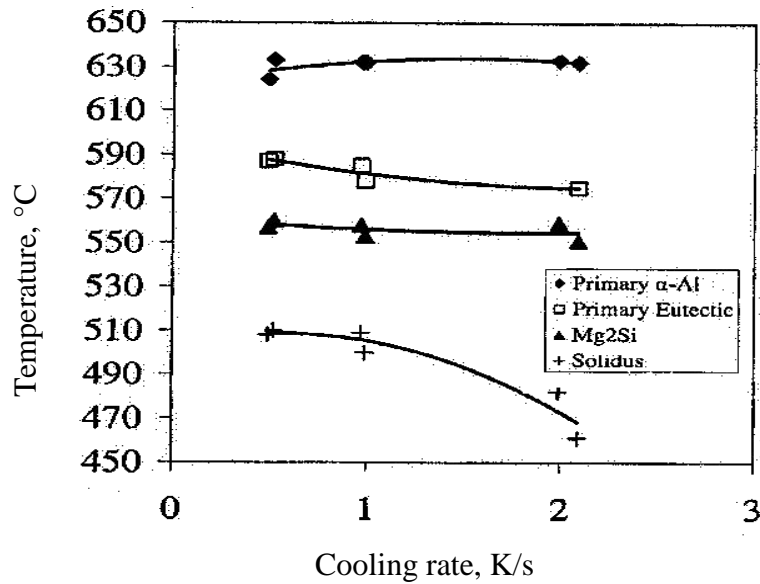


Figure 7: Plot of phase transformation temperatures of primary  $\alpha$ -Al, Primary eutectic, Mg<sub>2</sub>Si and solidus temperature in AA5182 aluminum alloy at different cooling rates [33]

On the other hand, to get the value for latent heat of fusion of multi-component alloys that solidify in a given temperature range (mushy zone) is not an easy task. In the mushy zone (the region between the liquidus and solidus temperature), the melt is neither in a totally liquid phase nor in a totally solid phase, but is a mixture containing a fractional amount of both liquid and solid. Changes in heat content in a solidifying material are directly proportional to the amount of solidification which has taken place, and are closely related to the thermodynamic forces driving the solidification process [36]. DSC is being used as a means of getting the latent heat information of the metals and alloys. Latent heat of solidification is measured from the DSC signal by measuring the total peak area after subtracting the base line. Figure 8 shows the dependence of the latent heat of fusion on the cooling rates studied by Kuang et al. [37] on pure Co using DSC. The latent heat of fusion has increasing trend as the cooling rate increases.

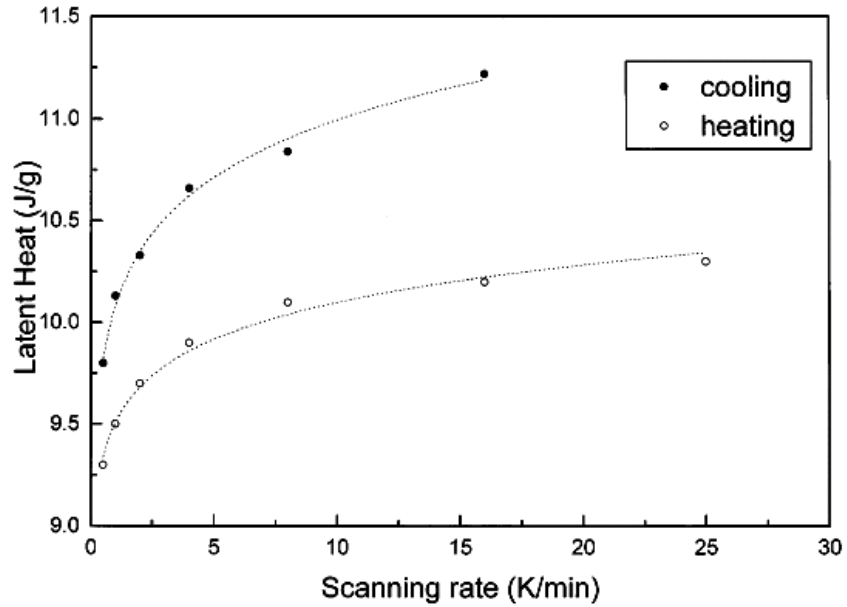


Figure 8: The effect of scanning rates on the latent heat of pure Co [37]

The final microstructure during solidification of alloys depends on the initial nucleation, the growth characteristics of primary phase and the final eutectic solidification [29]. The size and shape of the primary phase affects the size of the eutectic pockets that form upon solidification, and this will change the morphology of the eutectic [29, 30]. However, the cooling rate influences the final microstructure of the alloys by controlling the initial nucleation and grain size.

## 2.5 Solidification Characteristics of Magnesium Alloys

The solidification behavior of magnesium alloys is affected by alloying elements, grain refiners, and cooling rate during solidification. The growth morphologies of both the primary dendrites and the eutectic are highly dependant on the aluminum content and cooling rate [38]. All the commercial magnesium alloys start forming magnesium solid solution at the early stage of solidification which is denoted as  $\alpha$ -(Mg). The nucleation of the primary phase is sometimes

controlled by the addition of grain refiners. Most commercial magnesium products are produced by HPDC, which has a very high cooling rate and resulted in a high driving force for nucleation [39]. This causes increased nucleation and therefore creates a large number of primary grains thus reduces the need for an effective grain refiner. Figure 9 shows a typical fraction solidified as a function of the temperature for Mg-Al based alloys with different Al-contents. For most commercial Mg-Al alloys, it is common to observe eutectic constituents even when the Al-content is as low as 2 wt%.

Understanding the eutectic solidification also plays an important role in alloy development. This solidification event controls the size, shape and distribution of the more brittle  $\gamma$ -Mg<sub>17</sub>Al<sub>12</sub> phase in the final microstructure, which, in turn, likely to influence both the ductility and creep strength of the alloy [39]. Furthermore, being the final state of solidification process, eutectic growth affects the feedability at a crucial stage, when feeding is interdendritic and large pressure differentials are required to draw liquid through the dendritic network [40].

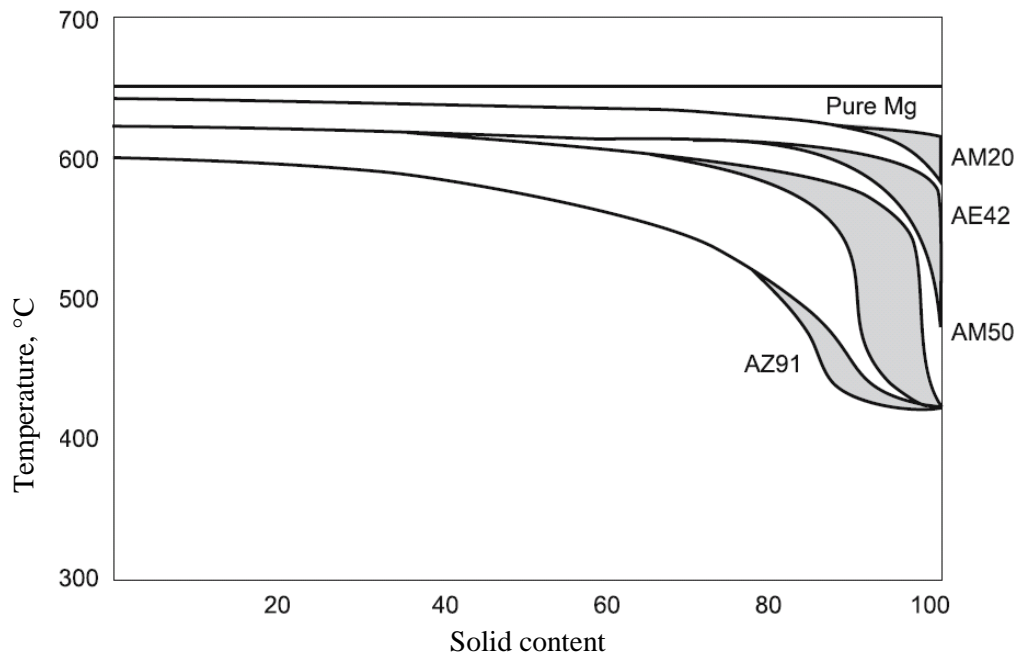


Figure 9: Solid content as a function of temperature for Mg-Al alloys [39]

Although in most commercial alloys the eutectic is a fully or partially divorced eutectic, it has been found to form lamellar, fibrous, and granular morphologies as well [29]. The lamellar and fibrous eutectic morphologies form in alloys with more than 12wt% Al. These morphologies are not likely to form in commercial alloys as the aluminium content in the commercial magnesium alloys is up to 9wt%. On the other hand, when the Al content is decreasing partially or fully divorced morphology is found, which is very common in commercial die-casting magnesium alloys [29]. Figure 10 shows the different morphologies of the  $[\alpha\text{-Mg} + \gamma\text{-Mg}_{17}\text{Al}_{12}]$  eutectic.

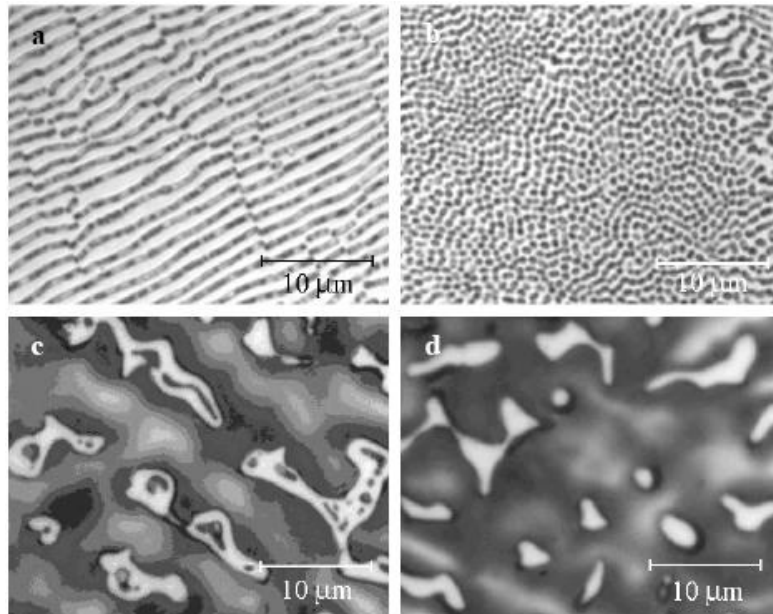


Figure 10: (a) Lamellar, (b) fibrous, (c) partially divorced and (d) fully divorced morphologies in Mg-Al alloys of various compositions [29]

Fully divorced morphologies are usually formed in die-casting where the cooling rate is extremely high such as 600°C/min, while partially divorced morphologies are more likely at lower cooling rates. In the fully divorced morphology (Figure 10-d), the eutectic-(Mg) coats the

primary dendrites and the intermetallic phase exists as massive particles or a thin layer between the coated dendrites [29]. The partially divorced eutectic (Figure 10-c) is similar; however not all the eutectic-(Mg) coats the primary dendrites - a small amount solidifies as islands inside the intermetallic phase.

Cooling rate plays an important role on the microstructure of the eutectic of commercial magnesium alloys. Slow cooling condition (near equilibrium) shows a partially divorced eutectic structure plus lamellar  $\gamma\text{-Mg}_{17}\text{Al}_{12}$  precipitates. It is believed that the lamellar  $\gamma\text{-Mg}_{17}\text{Al}_{12}$  structure is formed after solidification via discontinuous precipitation from  $\alpha\text{-Mg}$  supersaturated solid solution [42]. Such lamellar precipitates do not appear at higher solidification rates involved in magnesium casting. This is supported by the fact that the tendency to form divorced eutectic structure is enhanced at higher cooling rate, while the eutectic structure at lower cooling rate assumes a partially divorced morphology which turns to a completely divorced morphology in the die casting structure [42,43]. There is also a correlation between the average grain size and the cooling rate, although less pronounced. In general, the grain size decreases with increasing cooling rate. As discussed earlier, the grain size may be further influenced by deliberate grain refining additives.

Solidification behavior of the commercial magnesium alloys has been studied by many researchers [27,29-31,34,35,38-40,42-46] using different techniques such as DTA, DSC and TGA. Luo et al. [27] published some experimental results of the solidification behavior of different magnesium alloys including AZ, AM, AS and AE series under non-equilibrium and near equilibrium condition using DTA. They concluded that the effect of the cooling rate on the liquidus temperature is less significant than on the solidus temperature as shown in Table 6.

Table 6: Liquidus and solidus temperature of AZ91 alloy under different cooling rates [25]

Cooling rate (dT/dt, °C/s)	0.03	0.06	0.4	7.8	20.6	41.1
Liquidus (TL, °C)	600.2	600	599.5	598	595.5	593.8
Solidus (TS, °C)	435	435	430	320	-	-

Another researcher, Bassani et al. [44] also analyzed the solidification behavior of magnesium alloys through experimental investigation using DSC and revealed information such as phase transformation, enthalpy, and kinetics of dissolution of non-equilibrium phases at different heating and cooling rates. Han et al. [45] studied the solidification behavior of different commercial magnesium alloys such as AZ91D, AM60B, AS41 and AS21 using thermodynamic modeling and optical microscope. They mentioned that all of the investigated alloys solidified as primary  $\alpha$ -(Mg) dendrites with eutectic as well as intermetallic phases forming in the interdendritic regions. They also noticed that the eutectic, which is comprised of  $\alpha$ -(Mg) and  $\gamma$ -Mg<sub>17</sub>Al<sub>12</sub>, is present as divorced eutectic microstructure. Riddle et al. [46] carried out non-equilibrium thermal analysis on AM50A, AM60B, ZE41A and EZ33A magnesium alloys solidification using DTA as well as optical microscopy, scanning electron microscopy (SEM) and energy dispersive spectroscopy (EDS). They mentioned for the AM alloys, solidification began with  $\alpha$ -(Mg) dendrites followed by a fully divorced  $\gamma$ -Mg<sub>17</sub>Al<sub>12</sub> eutectic transformation and the existence of various Al-Mn-(Si) phases. According to their work, for the AM60B alloy the start of solidification, beginning of eutectic transformation and end of solidification were at 622.8°C, 435.1°C and 431.4°C respectively, which is consistent with the results of Luo et al. [27].

## 2.6 Thermal Analysis Technique

There are many techniques available for investigating the solidification behavior of metals and alloys. There are standardized techniques such as differential scanning calorimetry (DSC), differential thermal analysis (DTA) and thermo-gravimetric analysis (TGA). DSC is one of the modern apparatus for measuring both the qualitative and quantitative analysis of heat change. On the other hand, DTA measures only the qualitative analysis of heat exchange and TG measures the mass changes.

### 2.6.1 DTA/DSC

The differential thermal analyzer (DTA) is designed to measure the difference in temperature between two samples which are subject to the same heating/cooling regimen [47]. One of the two samples is a reference sample, commonly an inert material over the range of temperature being investigated. The sample and reference are required to have similarities and it can be advantageous to select reference materials with thermal similarities, such as thermal conductivity and heat capacity. In order to explain the features of a DTA curve, the enthalpy vs. temperature curve for Ag-15% Cu alloy and the  $dH_S/dT_S$  vs.  $T_S$  curve for the same alloy have been shown in Figure 11. The explanations obtained from this example apply to the DSC curve as well because they have the same meaning as those obtained from DTA. Figure 11(b) shows that an isothermal step is observed in enthalpy that corresponds to the eutectic melting. Upon completion of the eutectic melting, all of the Cu-rich phase has melted and the enthalpy curve rises with heating due to the continued melting of the Ag-rich phase.

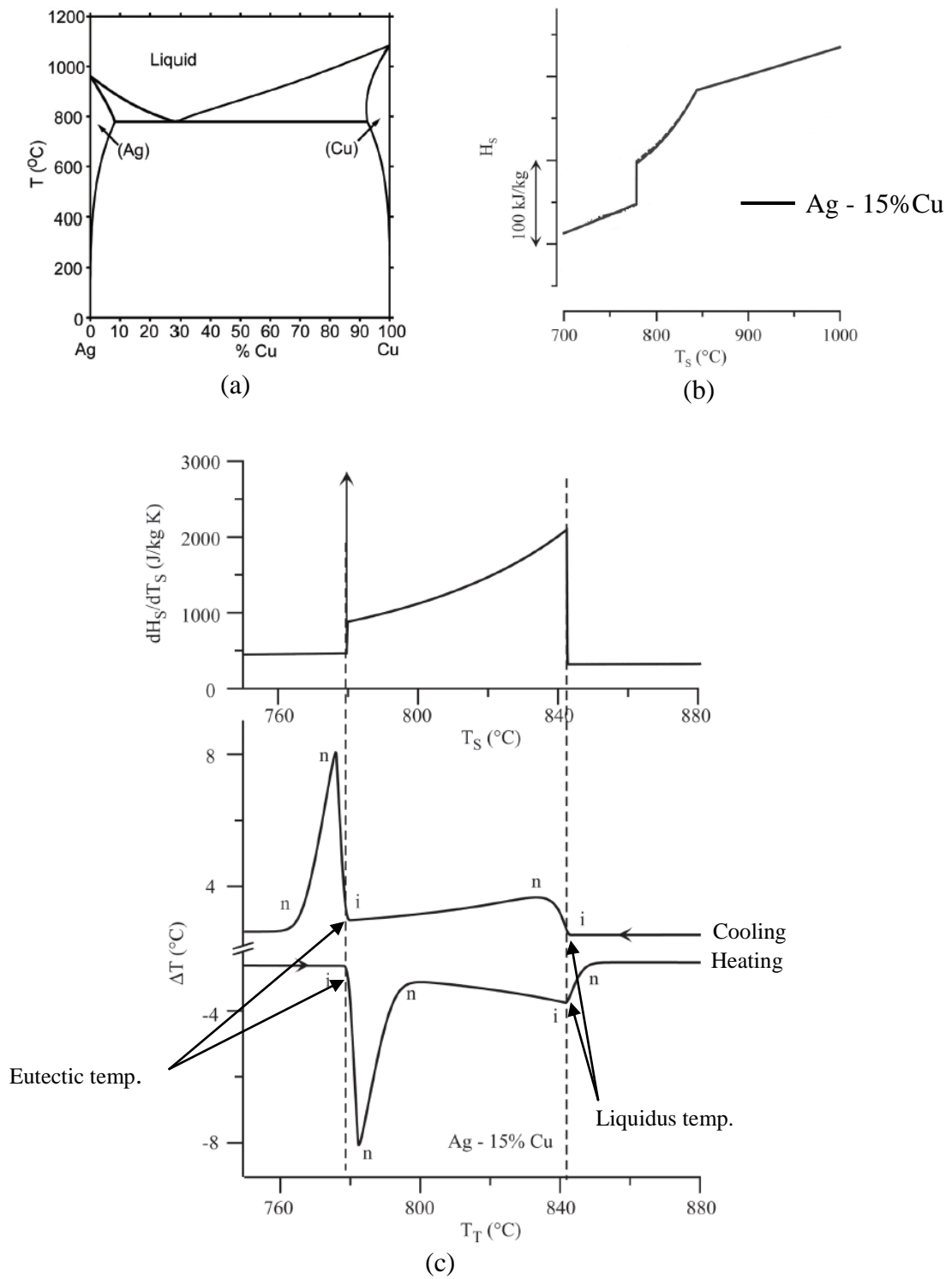


Figure 11: (a) Ag-Cu phase diagram, (b) enthalpy vs. temperature curve for Ag-15% Cu alloy (c)  $dH_S/dT_S$  vs.  $T_S$  curve and computed DTA scan for Ag-15% Cu alloy [52]

The  $dH_S / dT_S$  vs.  $T_S$  curve in Figure 11(c) shows that there are only two temperatures that have significance: the delta function at 779°C (eutectic temperature) and the vertical jump at 842°C (liquidus temperature). The significant temperatures ‘i’ correspond to the liquidus and the eutectic temperatures. In contrast, the heat transfer details produce other features ‘n’ on the DTA scans which bear no direct relation to the above two temperatures. In addition, there is the asymmetry of the interpretation of the melting and freezing scans, such as the peak on melting near the liquidus temperature is important but the peak just below the liquidus on cooling is unimportant. So, these points on the DTA scans are labeled with: ‘i’ = important or ‘n’ = not important depending on how well they approximate these two temperatures.

The differential scanning calorimeter (DSC) is based on many of the principles of the DTA. The difference between the DTA and DSC is that the DSC measures the heat input or heat removal required to keep the sample and the reference at the same temperature [48]. These devices are well documented and used throughout the world for measuring material’s physical properties such as transition temperatures, latent heat and specific heat. The DSC experiment requires the use of extremely small samples which would be on the order of few milligrams to one gram. This small sample size allows for the approximation of a uniform temperature over the entire sample, and for relatively rapid heating and cooling [49], which is required for the current work.

### **2.6.2 Principle of DSC**

Differential scanning calorimetry is a technique for determining the variation in the heat flow given out or taken in by a sample when it undergoes temperature scanning in a controlled atmosphere. When any transformation is taking place in a material with heating or cooling it is accompanied by an exchange of heat; DSC enables the temperature of this transformation to be

determined and the heat from it to be quantified [50]. It can be used to determine transition temperatures, melting and boiling point, crystallization time and temperature, percent crystallinity, heat of fusion and reaction, specific heat, rate and degree of cure, reaction kinetics and purity [51]. There are two types of DSC systems in common use: power compensated DSC and heat flux DSC.

### 2.6.2.1 Power compensated DSC

In power compensation DSC, the temperatures of the sample and reference are controlled independently using separate, identical furnaces. The temperatures of the sample and reference are made identical by varying the power input to the two furnaces. The difference in power used to heat the sample and reference is a measure of the enthalpy or heat capacity changes in the sample relative to the reference. Figure 12 shows a schematic diagram of power compensated DSC.

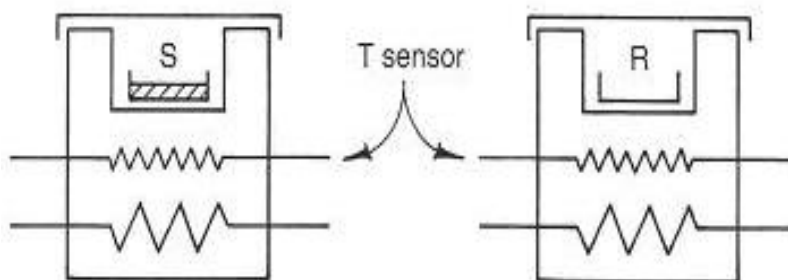


Figure 12: The principle of power compensated Differential Scanning Calorimeter Analysis [48]

### 2.6.2.2 Heat flux DSC

In heat flux DSC the sample and the reference are heated in one furnace. The difference in sample temperature and reference temperature is proportional to the heat flow between the sample and the reference.

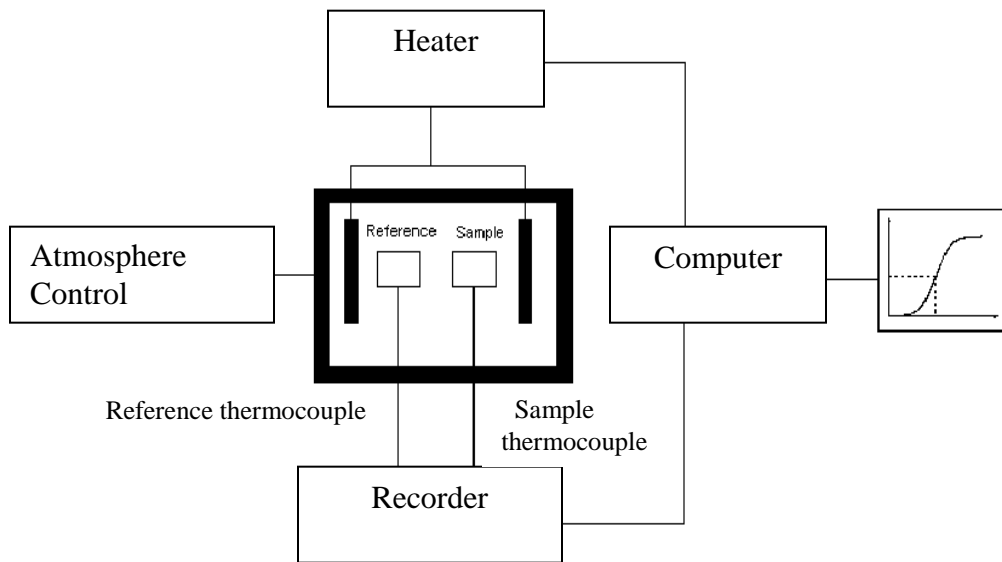


Figure 13: The principle of heat flux Differential Scanning Calorimeter Analysis [49]

Temperatures are measured in a thin plate in contact with those, thereby measuring the difference in heat flow from crucible which gives a signal proportional to the difference in heat capacities between the sample and reference. A schematic diagram of heat-flux DSC is shown in Figure 13.

Comparing with power compensated DSC, heat flux DSC is simple, and inexpensive and usually built to operate at higher temperatures ( $>1000^{\circ}\text{C}$ ) required for metallurgical work [48].

### 2.6.3 DSC Signal Interpretation

Understanding DSC measurements require a considerable amount of skill in thermal analysis. Some important explanations related with the DSC scan are shown in the Figure 14. The Zero line is the curve measured with the instrument empty, i.e. without samples and without sample containers (crucibles), or with the sample containers (crucibles) empty. The (interpolated) base line is the line constructed in such a way that it connects the measured curve before and after a peak, as if no peak had developed. A peak in the curve appears when the steady state is disturbed by some production or consumption of heat by the sample [51]. Peaks associated with endothermic process are plotted upwards (positive direction of heat addition to the system).  $T_i$ , initial peak temperature, begins where the curve of measured values begins to deviate from the baseline and  $T_e$ , extrapolated peak onset temperature, is drawn through the almost linear section of the ascending peak slope intersects the baseline [51].  $T_p$ , peak maximum temperature, is the difference between the DSC curve and the interpolated baseline is a maximum [51]. This is not necessarily the absolute maximum of the DSC curve.  $T_c$ , extrapolated peak completion temperature and  $T_f$  is final peak temperature, where the DSC curve returns to the baseline [51]. It is not always easy to detect accurately by naked eye the onset and completion of melting of ternary or more complicated systems. Well-prepared sample, multiple evacuation process and inert atmosphere are used to get precise DSC spectra. The records obtainable from DSC scans provide a more accurate way of establishing the solidification curves.

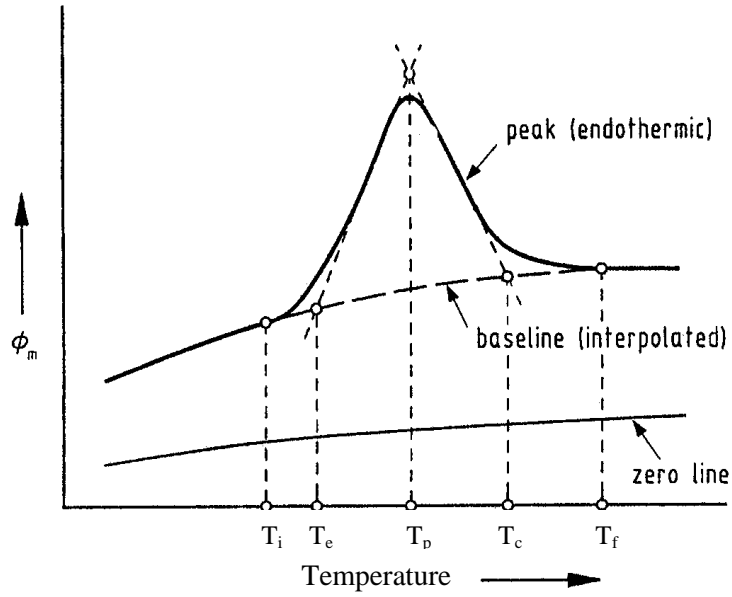


Figure 14: Definition of zero line, baseline, and characteristic temperatures [51]

### 2.6.4 Heat Transfer Model (HTM)

The solidification curve established from the DSC measurement is based on the heat transfer between the sample and the reference as shown in Tian equation [25]. Heat flow produced through transformation inside the sample is given by:

$$\Phi_r = -\Phi - (C_s - C_r) \frac{dT_r}{dt} - R_{fs} C_s \frac{d\Phi}{dt} \dots\dots\dots(1)$$

Where  $\Phi = \Phi_{fr} - \Phi_{fs}$  is the heat flow difference between the sample and the reference which is directly measured from DSC experiment,  $t$  is the time. The heat transfer resistance ( $R$ ) and the heat capacity ( $C$ ) of the reference ( $R_{fr}$ ,  $C_r$ ) and the sample cell ( $R_{fs}$ ,  $C_s$ ) will be approximated to be identical ( $R=R_{fr}=R_{fs}$ ;  $C=C_r=C_s$ ). The temperatures  $T_r$  and  $T_s$  are assumed to be uniform inside the cells. A schematic diagram of the DSC equipment and the heat transfer model quantities is shown in Figure 15.

The heat flow generated by exothermic or endothermic reactions,  $\Phi_r$  and phase transition of the sample can be expressed by heat evolution  $h$ , which occurs in the sample:

$$\Phi_r = \frac{dh}{dt} \dots\dots\dots(2)$$

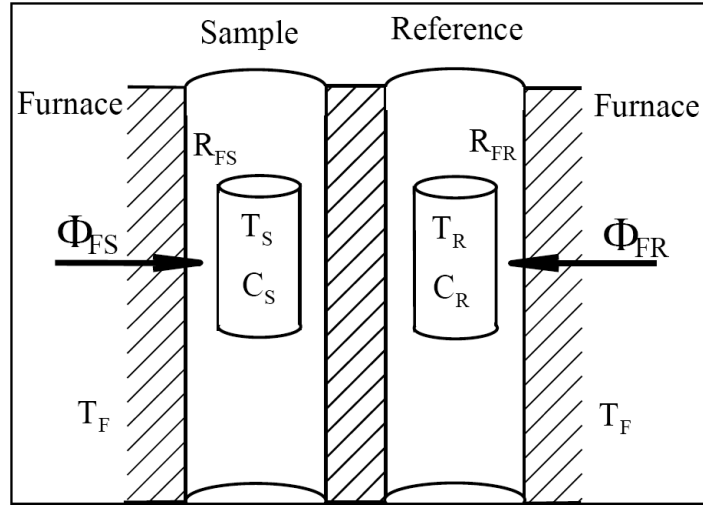


Figure 15: Schematic view of a heat flux DSC, with quantities used in the heat transfer model [53]

Chen et al. [54] assumed a linear dependence of the rate of heat evolution during solidification on the rate of solid phase fraction;

$$\frac{dh}{dt} = H \frac{d(1-f_l)}{dt} \dots\dots\dots(3)$$

The heat of solidification  $H$  or the total latent heat of solidification is assumed to be constant.

Finally equation (3) can be modified as:

$$H \frac{d(1-f_l)}{dt} = -\Phi - RC \frac{d\Phi}{dt} \dots\dots\dots(4)$$

The terms  $H$  and  $RC$  were treated as two adjustable parameters determined from the measured DSC curve of the sample by Chen et al [54]. The latent heat of solidification,  $H$  is obtained by integration of the area under DSC curve after the baseline was subtracted, and the term  $RC$  was iteratively obtained from the after reaction part of the DSC curve as no phase transformation occurs there [54].

# CHAPTER 3

## *Methodology*

---

This chapter explains the details about thermal analysis technique by DSC, metallography, thermodynamic calculation of solidification and analytical model for extrapolation of transition temperatures and enthalpies.

### **3.1 Approach**

The main focus of this work was to investigate the solidification behavior of AM60B, AZ91D and AE44 magnesium alloys experimentally using DSC and optical microscopy along with thermodynamic calculation. The methodology of the work is illustrated in Figure 16.

### **3.2 Thermal Analysis Using DSC**

Thermal investigation of the alloys was performed using a Setaram Setsys DSC-1200 instrument. Temperature calibration of the DSC equipment was done using pure magnesium and aluminium. The samples were cut and mechanically polished to remove any possible contaminated surface layers. Afterwards, they were cleaned with 1vol% nital solution ( $\text{HNO}_3$  in ethanol) and placed in a graphite crucible with a lid cover to contain magnesium vapors and protect the apparatus. To avoid oxidation, three evacuations followed by rinses with argon were done. The DSC measurements were carried out under flowing argon atmosphere with scanning rates of  $5^\circ\text{C}/\text{min}$  to  $45^\circ\text{C}/\text{min}$ . Different cooling rates were tried to see the effect of cooling rate on transition points, enthalpy and solidification behavior. The weight of the samples were kept around 30~60

mg. The reproducibility of every measurement was confirmed by collecting the data during three heating and cooling cycles. The estimated error between the repetitive heating and cooling is  $\pm 1^\circ\text{C}$  or less.

Table 7: DSC experimental conditions

Item	Conditions
Heating rate ( $^\circ\text{C}/\text{min}$ )	5 to 45
Cooling rate ( $^\circ\text{C}/\text{min}$ )	5 to 45
Temperature range ( $^\circ\text{C}$ )	100 to 700
Inert gas	Flowing argon
Weight of sample (mg)	30-60

All the required data were recorded from the cooling region of the DSC spectra. In the spectra, onset temperature for the solidification was obtained from the point of the intersection between the extrapolated baseline and the linear section of the ascending peak slope. The temperature at which the DSC signal returned to the baseline corresponds to the solidus temperature. The enthalpy, which is the area under the DSC peak, was measured after the subtraction of the baseline. The baseline was obtained using empty crucibles in the sample and reference pans. Finally, the solidification curves were drawn from the DSC data using the Heat Transfer Model (HTM).

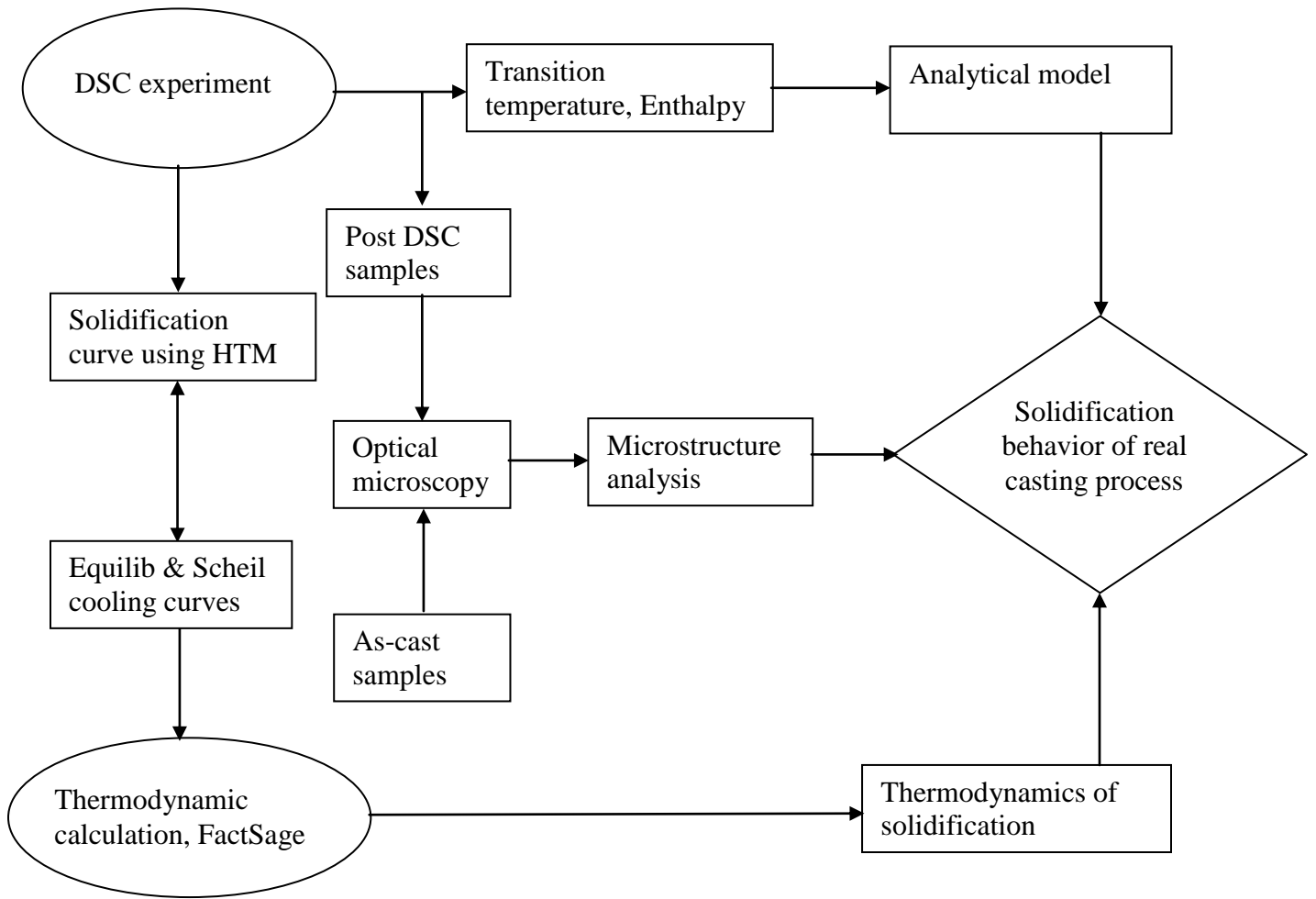


Figure 16: Flow chart illustrating the methodology of the current work

### 3.3 Metallography

Sample preparation and metallography of magnesium alloys can be a daunting task. The soft nature of the magnesium matrix and the substantially harder intermetallic phases cause the most problem during polishing. Magnesium alloys also readily react with water, thus restricting the

use of many polishing media and suspensions. This leads to difficulty in eliminating scratches, controlling relief between phases, and creates potential for matrix deformation.

For optical microscopy, the samples were first cut and then mounted in resin by cold curing. Grinding was performed using silicon carbide (SiC) grinding papers up to 1200 grit. Samples were rinsed thoroughly before moving to a smaller grit SiC. Prior to polishing, the sample was rinsed with ethanol and cleaned for several minutes using an ultra-sonic cleaner. Samples were hand polished with 6  $\mu\text{m}$  diamond suspension and the velvet polishing cloths were used at a maximum wheel speed of 150 rpm. Slower wheel speeds were used because higher speeds tend to cause excessive pullout of the intermetallic phases resulting in more scratches. The samples were polished until scratches appear as uniform as possible. The samples were then thoroughly cleaned in ethanol and placed in an ultra-sonic cleaner for several minutes. Then the polishing procedure was repeated with the 3  $\mu\text{m}$  size diamond suspension. At the end, after ultra-sonic cleaning, a final polish was performed with a 1  $\mu\text{m}$  diamond solution.

Finally, the samples were etched using the following etchants (acetic glycol): 20ml acetic acid, 1ml  $\text{HNO}_3$  (conc.), 60ml ethylene glycol and 20ml water. Etching was performed by applying the etchant on the surface for a short period (5/10 seconds). The change in the microstructure of the post-DSC samples was observed and compared with the as-cast samples. Different phases present in the microstructure were identified based on what is reported in the literature.

### **3.4 Thermodynamic Calculation of Solidification**

Solidification curves of the three alloys have been drawn both in equilibrium and Schiel models using FactSage. These calculations were compared with the experimental results. Phase distribution diagrams have been calculated to understand solidification sequence and phase

content at different stage of solidification. Phase distribution diagram shows the relative amount of each phase as well as the formation and decomposition temperatures. The proportion of different phases at any temperature of interest can be read from this diagram.

### **3.5 Analytical Model for Extrapolation to Higher Cooling Rate**

Based on the DSC experimental results an analytical model was developed for transition temperatures and enthalpies to investigate the effect of extremely high cooling rate. A general power law has been used to establish the relationship between cooling rates and transition temperatures as well as between cooling rates and enthalpy. This is based on what has been reported in many articles such as [37, 66-69]. After the relationship has been developed, calculations were made to get information at extremely high cooling rates and compared with available experimental data.

# CHAPTER 4

## *Results and Discussions*

---

This chapter discusses the experimental and analytical results of the current work.

### **4.1 Thermal Analysis Results**

Experimental investigations were carried out using the DSC at different cooling rates from 5°C/min to 45°C/min at a cooling rate step of 5°C. The data output from each experiment includes heat flow and temperature. These data were then analyzed to draw the solidification curves after subtracting the baseline. The values of transition temperatures and solidification enthalpies were obtained from the cooling spectrum only.

#### **4.1.1 Experimental Results of AZ91D Alloy**

The DSC curve of AZ91D sample obtained at 5°C/min scanning rate is shown in Figure 17. The spectrum has two exothermic peaks both during cooling and heating. The first cooling peak represents the formation of primary  $\alpha$ -(Mg) phase and the second peak stands for the eutectic transformation. The experiment was carried out on the same alloy up to 45°C/min at a cooling rate step of 5°C. After subtracting the baseline some of the DSC spectra are superimposed and shown in Figure 18.

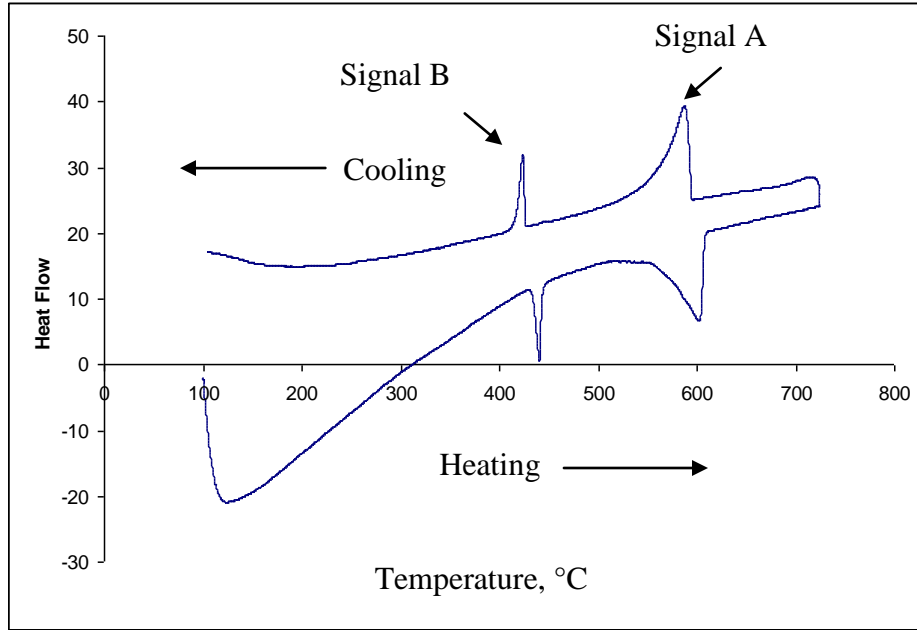


Figure 17: DSC spectra of AZ91D at 5°C/min scanning rate

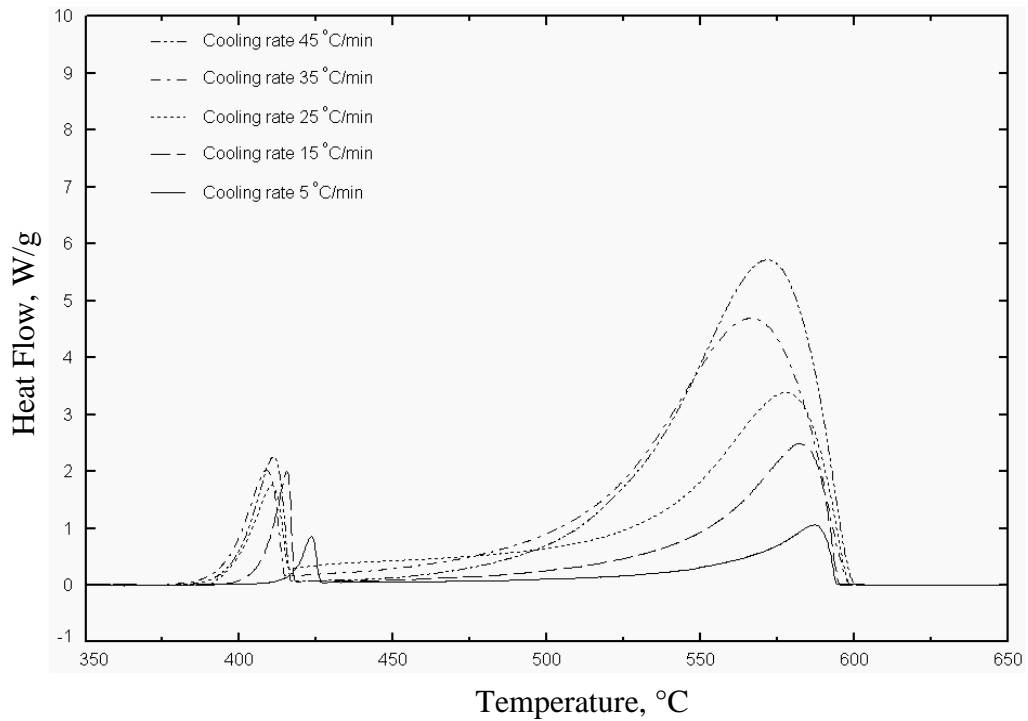


Figure 18: DSC spectra of AZ91D alloy at different cooling rates (after subtracting the baseline)

The DSC software allows in getting the information such as transition temperatures directly from the spectra. The onset of the first peak stands for the liquidus temperature and the onset of the second peak corresponds the eutectic temperature. The transition temperatures and latent heat of solidification were recorded in Table 8. The transformation temperatures are plotted in the Figure 19 and the latent heat of solidification of all the three alloys are summarized in section 4.1.4.

The liquidus temperature obtained at 5°C/min cooling rate is 595°C and it increases a little with increasing the cooling rates. The maximum variation observed in liquidus temperature is +7°C. However, the cooling rates have reverse effect on both eutectic and solidus temperatures. The eutectic formation temperature observed at 5°C/min cooling rate is 426.3°C and it drops up to 414.4°C with increasing the cooling rate. Finally, the solidus temperature observed at 5°C/min cooling rate is 423.2°C and the maximum drop off is 14.7°C. The solidification range at slowest experimental cooling rate is 172°C and it reaches to a maximum of 192°C at higher cooling rate.

Table 8: Transition temperatures and latent heat of solidification of AZ91D alloy

Cooling rate, °C/min	Liquidus temp. °C	Eutectic temp. °C	Solidus temp. °C	Latent heat of solidification, J/g
5	595.0	426.3	423.2	370.4
10	593.7	422.6	419.3	433.8
15	595.1	417.8	415.3	499.1
20	598.9	417.0	414.4	556.3
25	598.6	416.2	410.4	604.0
30	602.4	419.8	416.6	661.4
35	601.0	414.4	408.5	708.2
40	598.3	415.8	410.5	741.1
45	599.8	415.3	410.9	757.5

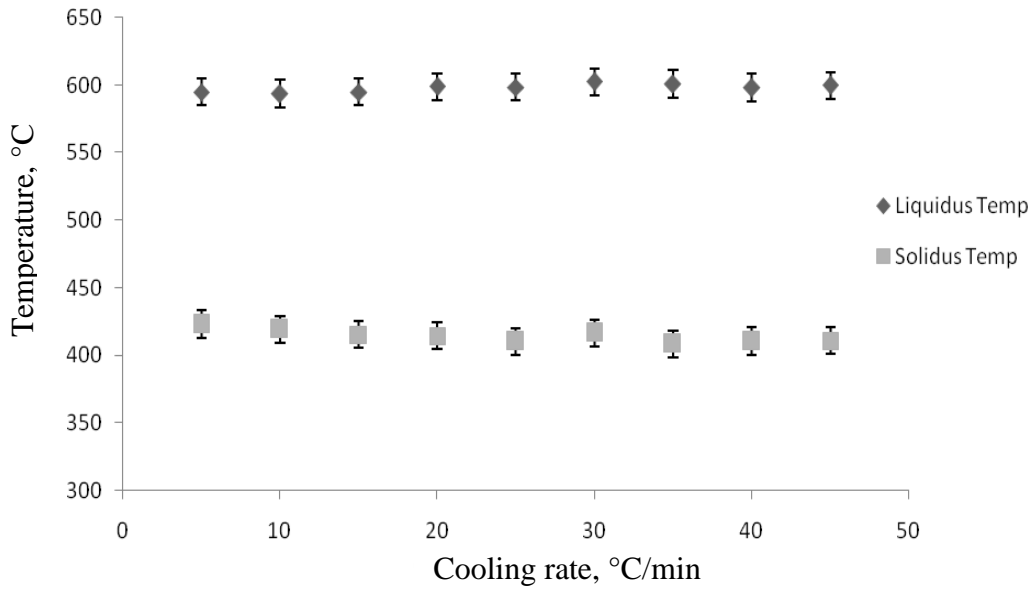


Figure 19: Transformation temperature of AZ91D at different cooling rates

The solidification curves of this alloy calculated using HTM model are shown in Figure 20. The fraction of liquid starts to decrease when  $\alpha$ -(Mg) precipitates at around 600°C and continues to decrease markedly down to 550°C. At that temperature almost 50% of the liquid turns into solid and after that solid formation becomes slower. At around 425°C the observed sharp kink represents the eutectic formation. From Figure 20 it is also obvious that the alloy ends up with larger amount of eutectic as the cooling rate increases. Other phases that form during solidification of this alloy might be very small in quantity and must have very weak signals and thus could not be detected in the DSC experiment. The solidification sequences showed in Table 9 are obtained from DSC experiment as well as supported by literature [27]. A more details solidification sequence has obtained from thermodynamic calculation and discussed in section 4.2.2

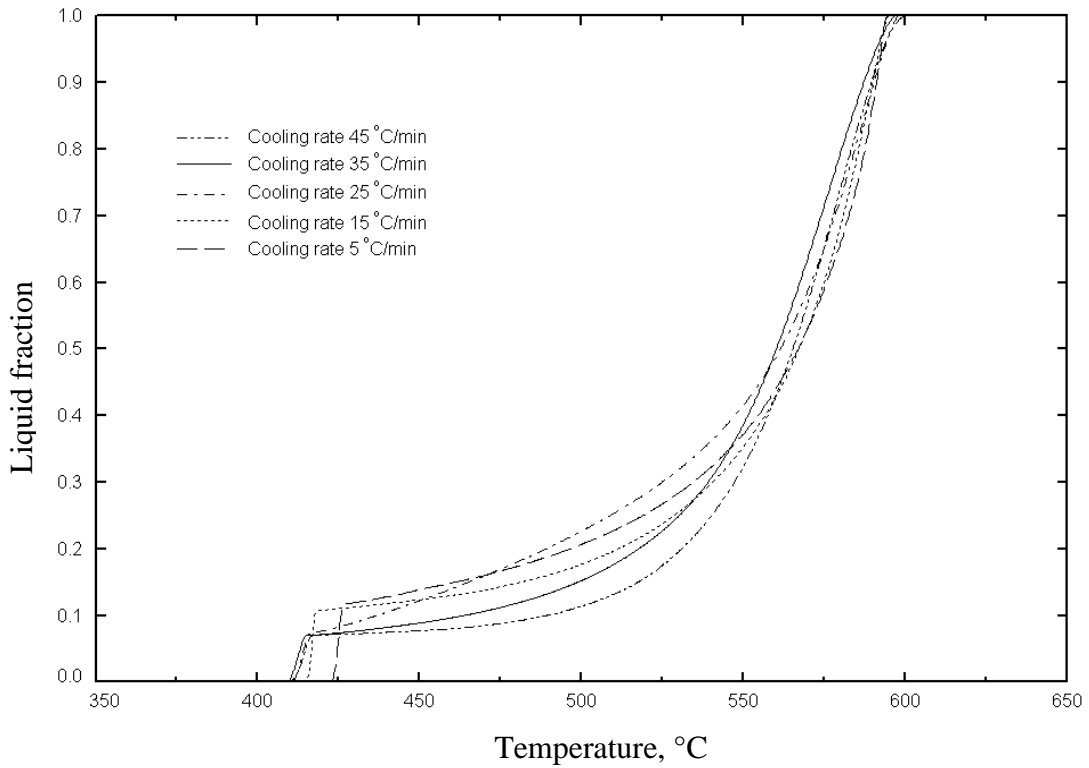


Figure 20: Solidification curves of AZ91D at different cooling rates drawn from the experimental data using HTM

Table 9: Experimental solidification sequence of AZ91D alloy

Temperature	Transformation
TL (593°C - 602°C)	Start of $\alpha$ -(Mg) nucleation: $L \longrightarrow \alpha\text{-(Mg)} + L$
TL-TE	Growth of $\alpha$ -(Mg) phase: $L \longrightarrow \alpha\text{-(Mg)} + L$
TE (408°C - 419°C)	Eutectic reaction: $L \longrightarrow \alpha\text{-(Mg)} + \gamma\text{-Mg}_{17}\text{Al}_{12}$

### 4.1.2 Experimental Results of AM60B Alloy

The solidification characteristics of AM60B are analogous to that of AZ91D. The DSC curve of the AM60B sample obtained at 5°C/min is shown in Figure 21. The first cooling peak stands for the formation of primary  $\alpha$ -(Mg) phase and the second represents the eutectic transformation. The experiment was carried out on the same alloy up to 45°C/min at a cooling rate step of 5°C. The DSC spectra at different cooling rates are shown in Figure 22.

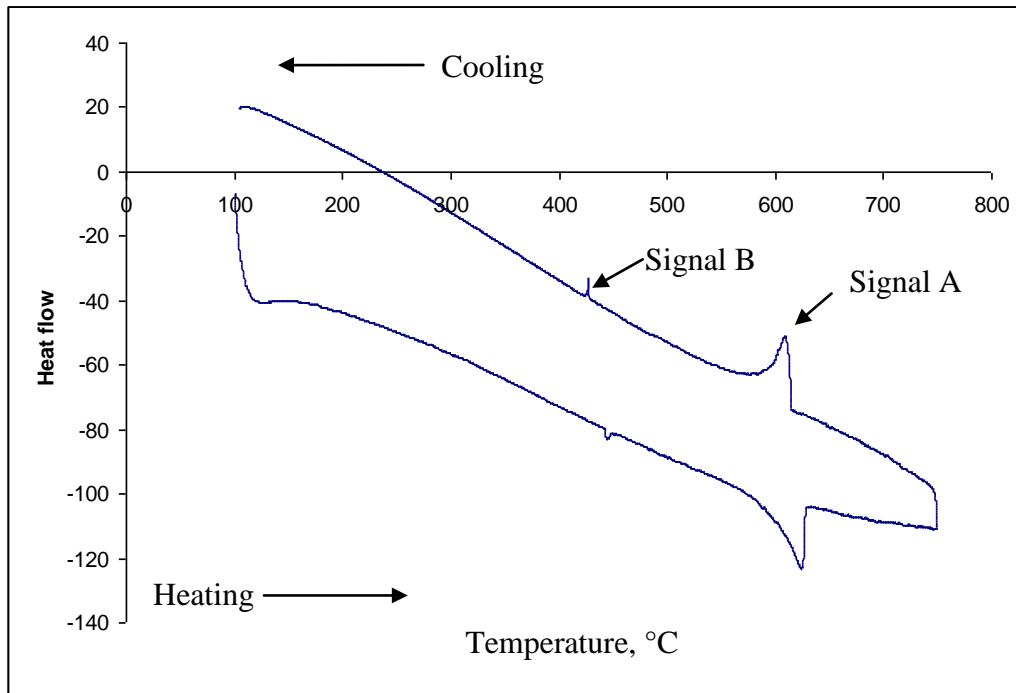


Figure 21: DSC spectra for AM60B at 5°C/min scanning rate

Similar to the AZ91D alloy, information such as transition temperatures for the AM60B alloy are directly obtained from the DSC spectra. The onset of the first peak stands for the liquidus temperature, the onset of the second peak corresponds the eutectic temperature and the solidus temperature has been obtained from the experimental solidification curve. The transition temperatures and latent heat of solidification were recorded in Table 10. The transformation

temperatures are plotted in the Figure 23 and the latent heat of solidification of all the three alloys are reviewed in section 4.1.4. The liquidus temperature obtained at 5°C/min cooling rate is 619.5°C and it decreases a little with increasing the cooling rates. The maximum variation observed in liquidus temperature is +5°C. On the other hand, the cooling rates have similar effect on the eutectic and solidus temperatures. The eutectic formation temperature observed at 5°C/min cooling rate is 427.5°C and it drops up to 419.5°C with increasing the cooling rate. Finally, the solidus temperature observed at 5°C/min cooling rate is 428.1°C and the maximum drop off is 11.3°C in the range of experiment done here. The solidification range at slowest experimental cooling rate is 191°C and it reaches to a maximum of 201°C at higher cooling rate.

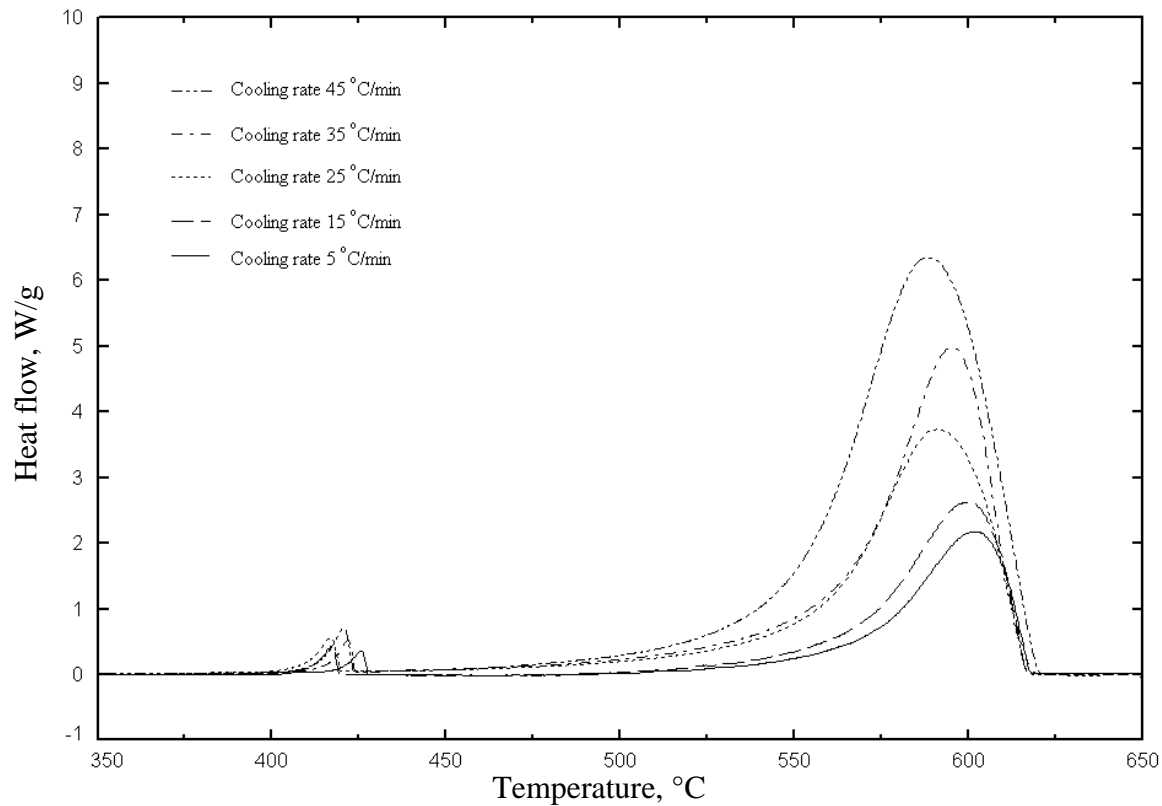


Figure 22: DSC spectra of AM60B alloy at different cooling rates after subtracting the baseline

For the AM60B alloy the liquidus temperature increases slightly with increasing cooling rates, however, the solidus temperature decreases with increasing cooling rate. The cooling effect on the solidus was more than that of the liquidus. The solidification enthalpy also shows an increasing trend with increasing the cooling rate.

Table 10: Transition temperatures and latent heat of solidification of AM60B alloy

Cooling rate, °C/min	Liquidus temp. °C	Eutectic temp. °C	Solidus temp. °C	Latent heat of solidification, J/g
5	619.5	427.5	428.1	354.3
10	622.5	420.1	418.7	433.8
15	620.7	419.2	417.8	488.5
20	621.4	420.9	418.5	549.6
25	617.4	419.5	416.8	620.8
30	621.2	421.8	418.7	657.8
35	622.3	422.4	420.4	688.9
40	619.0	420.2	418.1	706.1
45	621.8	423.3	420.4	716.2

Using the HTM model the solidification curves at different cooling rates of this alloy have been drawn and shown in Figure 24. Solidification starts at around 620°C and the fraction of liquid starts to decrease when  $\alpha$ -(Mg) precipitates and continues to decrease distinctly down to approximately 575°C. Almost 80% of the liquid turns into solid at that temperature then solid formation becomes slower. Finally, at the eutectic temperature all the remaining liquid turns into solid.

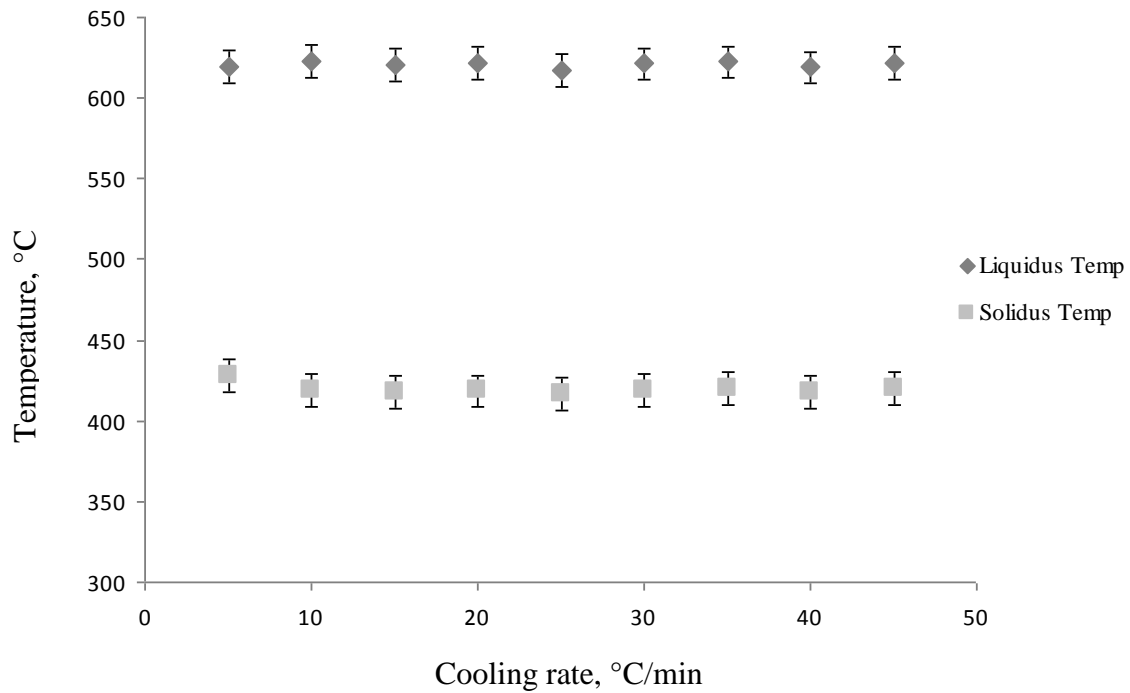


Figure 23: Transformation temperatures of AM60B alloy at different cooling rates

From Figure 24 it is also clear that the alloy ends up with increasing amount of eutectic as the cooling rate increases and similar behavior was observed for AZ91D alloy. The liquidus and solidus temperatures of AM60B are a few degrees higher than that of AZ91D, but AM60B alloy has less the amount of eutectic than that of AZ91D as will be discussed later in the microstructure analysis section (section 4.3). The experimental solidification sequences obtained from DSC experiment are showed in Table 11 which is well supported by literature [27].

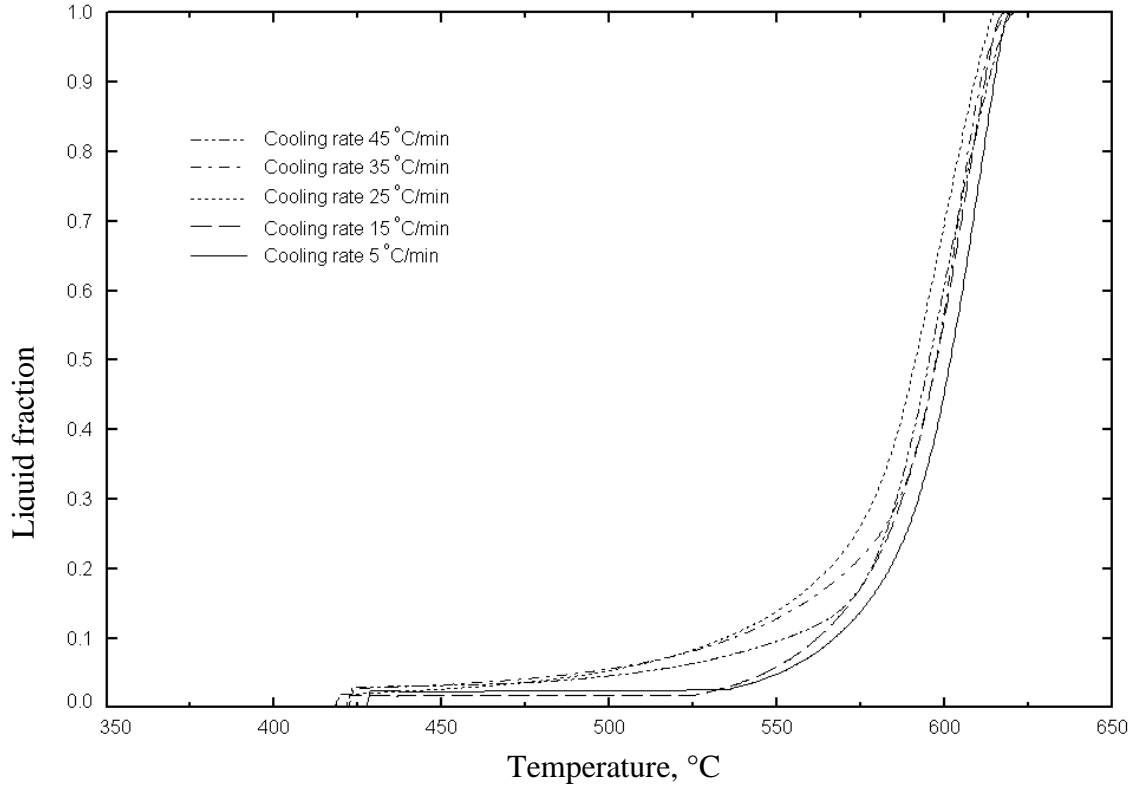


Figure 24: Solidification curve of AM60B alloy drawn from the experimental data using HTM

Table 11: Experimental solidification sequence for AM60B alloy

Temperature	Transformation
TL (614°C-623°C)	Start of $\alpha$ -(Mg) nucleation: $L \longrightarrow \alpha$ -(Mg) + L
TL-TE	Growth of $\alpha$ -(Mg) phase: $L \longrightarrow \alpha$ -(Mg) + L
TE (416°C-428°C)	Eutectic reaction: $L \longrightarrow \alpha$ -(Mg) + $\gamma$ -Mg <sub>17</sub> Al <sub>12</sub>

#### 4.1.3 Experimental Results of AE44 Alloy

The solidification characteristics of AE44 are little bit different than those of AZ91D and AM60B. The DSC curve of the AE44 alloy at 5°C/min is shown in Figure 25. The spectrum has only one peak during cooling which represents the formation of primary  $\alpha$ -(Mg) phase.

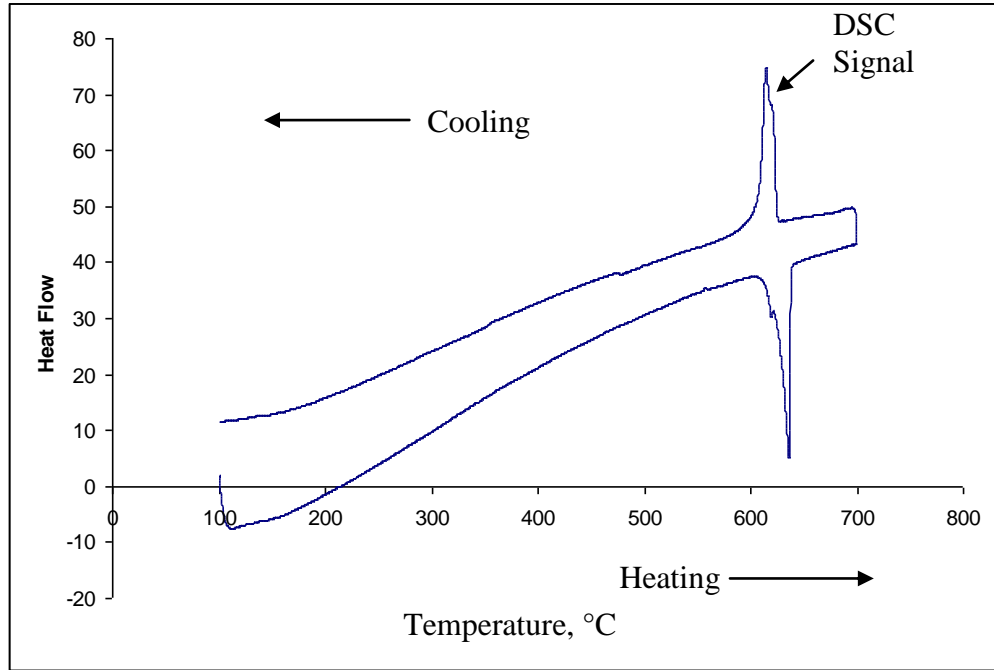


Figure 25: A DSC spectra of the AE44 alloy at 5°C/min scanning rate

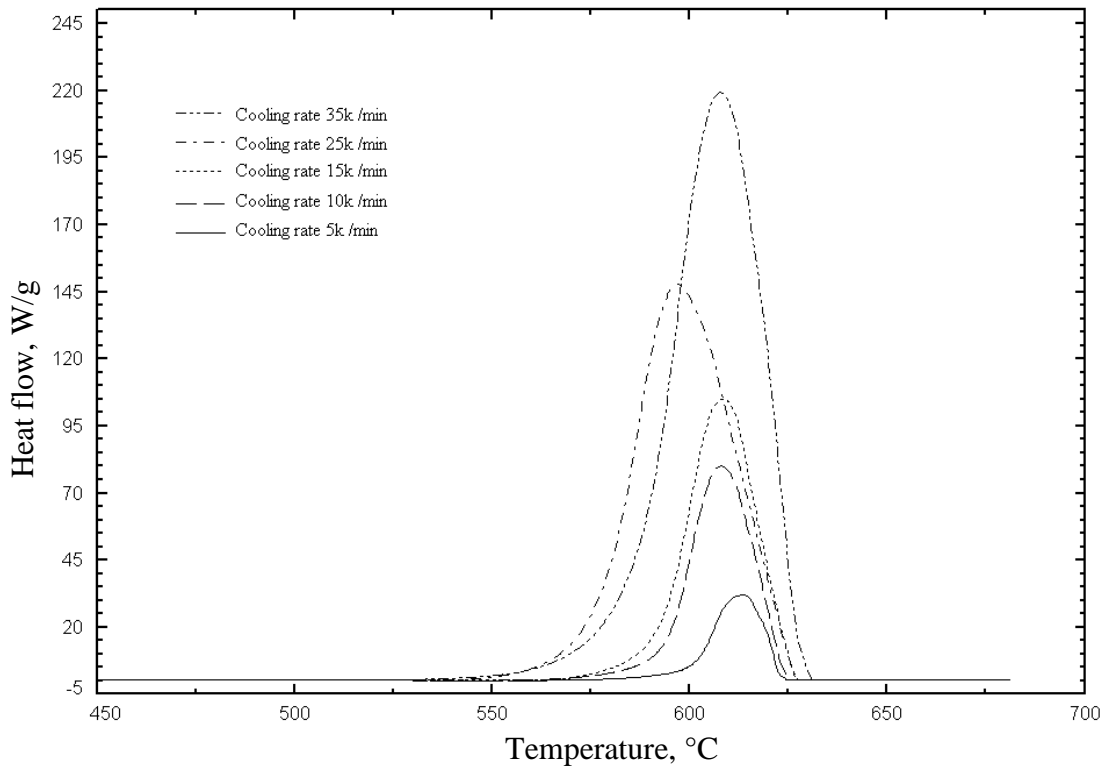


Figure 26: DSC spectra of AE44 alloy at different cooling rates after subtracting the baseline

The absence of the second peak indicates that either no eutectic forms during solidification or the amount of the eutectic is so small that it cannot be detected by the DSC experiment. Other phases of Al-RE are formed during the solidification temperature range. The amount of other phases is also so small that no additional peak was detected in the DSC experiment. After subtracting the base lines, the DSC spectra at different cooling rates are summarized in Figure 26. During cooling, solidification takes place with one exothermic peak over the temperature range from  $627^{\circ}\text{C}\pm 3^{\circ}\text{C}$  to  $584^{\circ}\text{C}\pm 7^{\circ}\text{C}$ .

The recorded transition temperatures and latent heat of solidification are summarized in Table 12. The transformation temperatures are plotted in the Figure 27 and the latent heat of solidification are discussed in section 4.1.4. The liquidus temperature increases to some extent with increasing cooling rates while the solidus temperature decreases with increasing cooling rate. The solidification enthalpy shows an increasing trend with increasing the cooling rates.

Table 12: Transition temperatures and latent heat of solidification of AE44 alloy

Cooling rate, $^{\circ}\text{C}/\text{min}$	Liquidus temp. $^{\circ}\text{C}$	Solidus temp. $^{\circ}\text{C}$	Latent heat of solidification, J/g
5	624.2	590.9	406.1
10	625.1	584.1	427.3
15	626.5	581.9	444.7
20	625.6	576.2	454.0
25	627.7	577.3	467.1
30	630.0	576.9	474.9
35	630.9	576.7	481.6

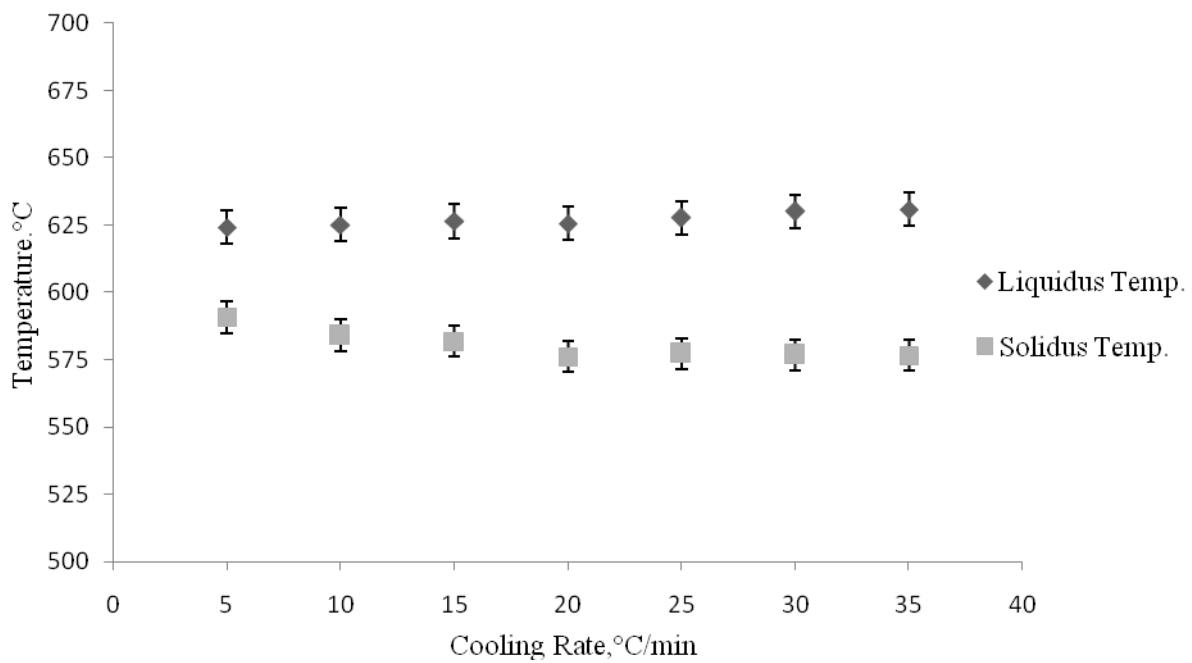


Figure 27: Transformation temperature of AE44 alloy at different cooling rates

The solidification curve of this alloy calculated using HTM model is shown in Figure 28. The fraction of liquid starts to decrease when  $\alpha$ -(Mg) solution precipitates at around 625°C and continues to decrease sharply till the end of solidification. Absence of any kink in the solidification curve indicates that no eutectic reaction occurs during the solidification process of this alloy. The experimental solidification sequences obtained from DSC experiment are summarized in Table 13.

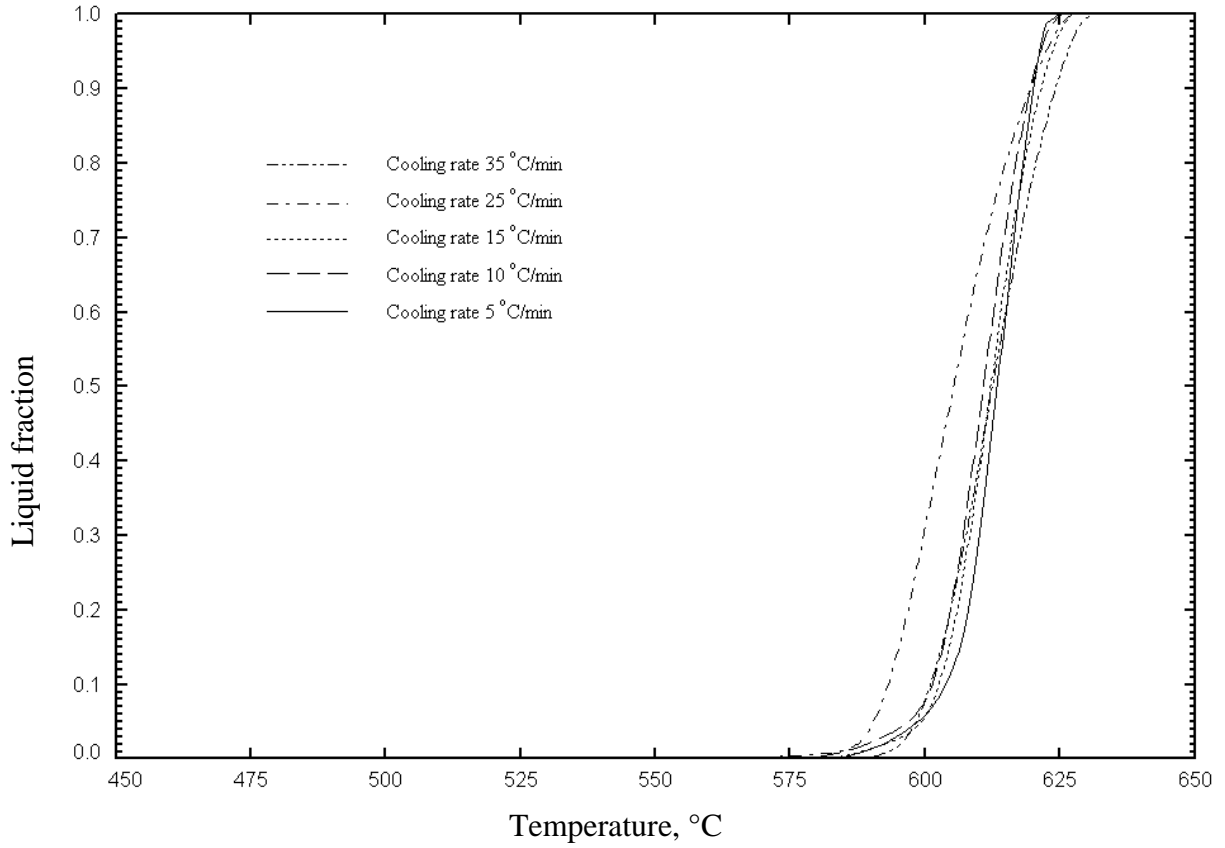


Figure 28: Solidification curve of AE44 drawn from the experimental data using HTM

Table 13: Experimental solidification sequences of AE44 alloy

Temperature	Transformation
TL (624°C-631°C)	Start of $\alpha$ -(Mg) formation: $L \longrightarrow \alpha\text{-(Mg)} + L$
TF	Start of (Al,RE) formation: $L \longrightarrow (\text{Al,RE}) + L$
TS (576°C-593°C)	End of solidification: $L \longrightarrow \alpha\text{-(Mg)} + (\text{Al,RE})$

#### 4.1.4 Latent Heat of Solidification

For the three alloys, the latent heat of solidification versus cooling rate curve is shown in Figure 29. The latent heat of solidification has been measured taking into consideration the area between the DSC curve and the baseline. This area is proportional to the latent heat energy released during solidification. For the three experimental alloys, the latent heat clearly shows an increasing trend with the increasing cooling rates. The rapid growth at the beginning of solidification process gives a solid phase with a large fraction of lattice defects such as vacancies which increases the energy of the solid phase [76]. The fraction of vacancies increases with increasing cooling rate. These vacancies will diffuse and create clusters, form dislocation or move to grain boundaries during solidification resulting in increasing heat release and, therefore, the latent heat of solidification increases [76].

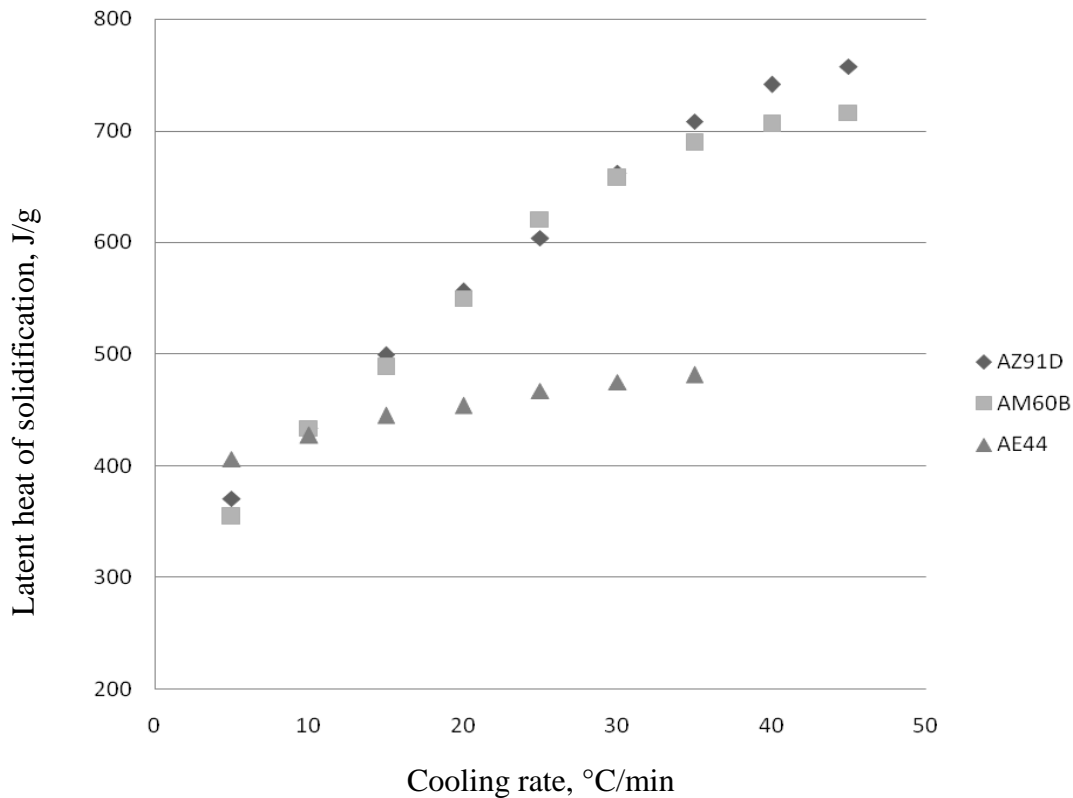


Figure 29: Change of latent heat of solidification of the alloys at different cooling rates

## **4.2 Thermodynamic Calculation of Solidification**

Calculations of solidification curves and phase distribution of the alloys have been done using the software FactSage along with VLGM database. Calculated solidification curves are compared with the experimental results and phase distribution are analyzed to get information about the different phases that form during the final stage of solidification.

### **4.2.1 Calculation of Solidification Curves**

The solidification curves of the AZ91D, AM60B and AE44 alloys have been calculated both in equilibrium and Scheil models and compared with the experimental results.

The solidification curves of AZ91D alloy is calculated and shown in Figure 30. The solid line in Figure 30 stands for the equilibrium cooling and the dashed line represents the Scheil cooling conditions. Three experimental solidification curves at 5°C/min, 25°C/min and 45°C/min cooling rates have also been superimposed in Figure 30 and compared with the calculations. For AZ91D alloy, the experimental solidification process begins at around 600°C and this is consistent with both equilibrium and Scheil cooling condition. This consistency continued until approximately 50% of the liquid turns into solid. Under equilibrium condition the solidification ends at 440°C which is much higher than those of Scheil and experimental cooling. The kink of the Scheil cooling curve, which corresponds to the precipitation of eutectic phase, is observed at around 430°C and this is consistent to the experimental results. However, this alloy solidifies at a higher temperature than the prediction from the Scheil cooling condition.

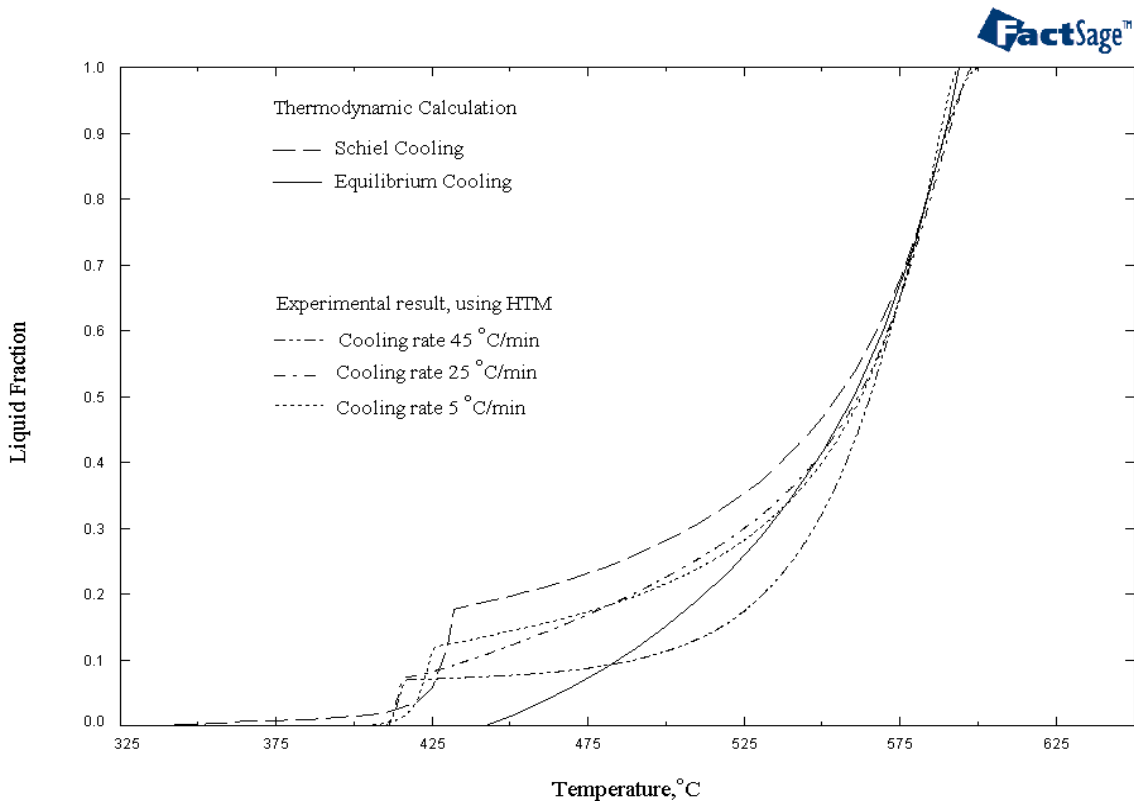


Figure 30: Comparison between experimental and calculated solidification curves of AZ91D

The Figure 31 demonstrates the detailed comparison between the thermodynamic prediction and experimental results of the transition temperatures of AZ91D alloy. The horizontal axis is the measured value, while the vertical axis is the predicted value. In the Figure 31 it is clearly seen that the measured liquidus temperature in excellent agreement with both equilibrium and Scheil prediction. However, the end of solidification under Scheil cooling condition is 355°C whereas the experimental solidification at different cooling rates ends at around 415°C. The difference is because of the residual liquids, which becomes extremely small or negligible in the later stage of solidification and to avoid this big difference a cut-off limit of the residual liquids has been

introduced [73]. A larger cut-off limit value of the residual liquid amount may end the simulation early resulting the liquid phase completely solidified before the simulation reaches the eutectic whereas a small cut-off limit value will produce the eutectic phases. For this current work a 2% cut-off limit has been chosen without affecting the eutectic phases. After applying the residual liquid cut-off limit for the AZ91D alloy the Scheil solidus temperature increased from 362°C to 390°C as shown in Figure 31 and this is much closure to the experimental solidus temperatures.

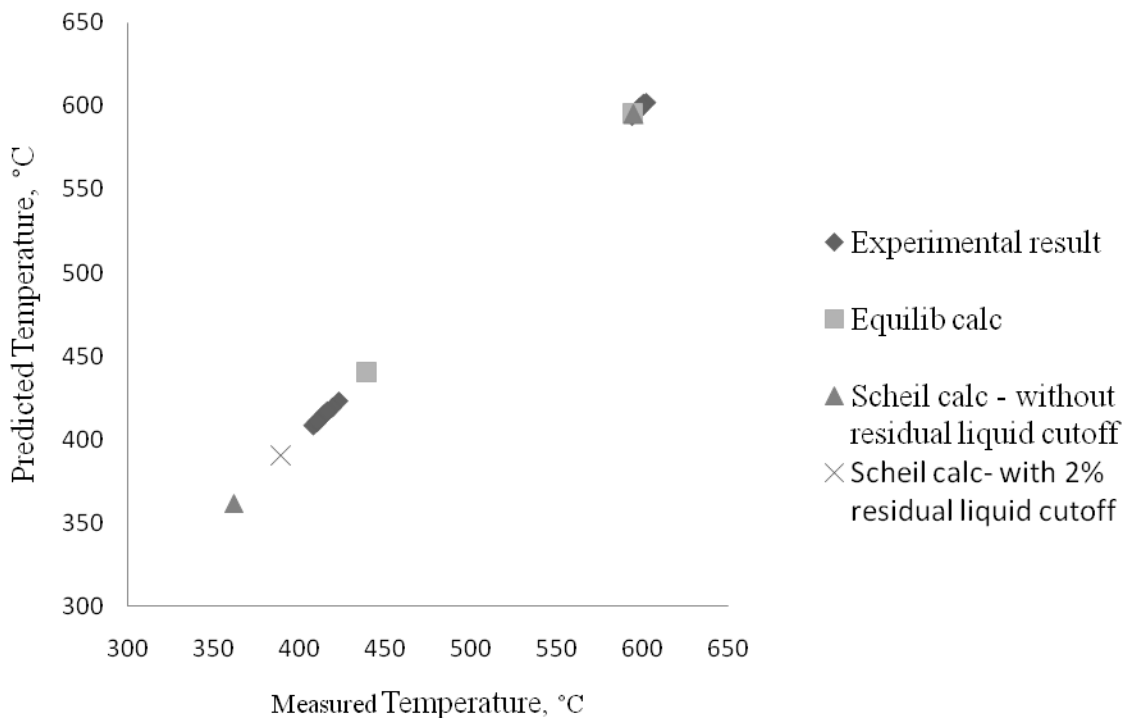


Figure 31: Comparison between experimental and calculated transition temperatures of AZ91D alloy

The solidification curves of AM60B alloy is calculated both in equilibrium and Scheil cooling condition and shown in Figure 32. The solidification curves calculated under equilibrium condition indicated by the solid line in the Figure 32 and the dashed line represents the Scheil

cooling curve. Three experimental solidification curves at 5°C/min, 25°C/min and 45°C/min cooling rates have also been superimposed in Figure 32 and compared with the calculation. The bend observed in the Scheil cooling curve at 430°C corresponds to the precipitation of eutectic phase and this bend is also observed in the experimental solidification curves. According to Scheil cooling the volume fraction of the eutectic forms is 11%, but experimentally it has been found 4% at 5°C/min cooling rate which increases with increasing cooling rates. Microstructure analysis also supports this phenomenon as discussed in the section 4.3.

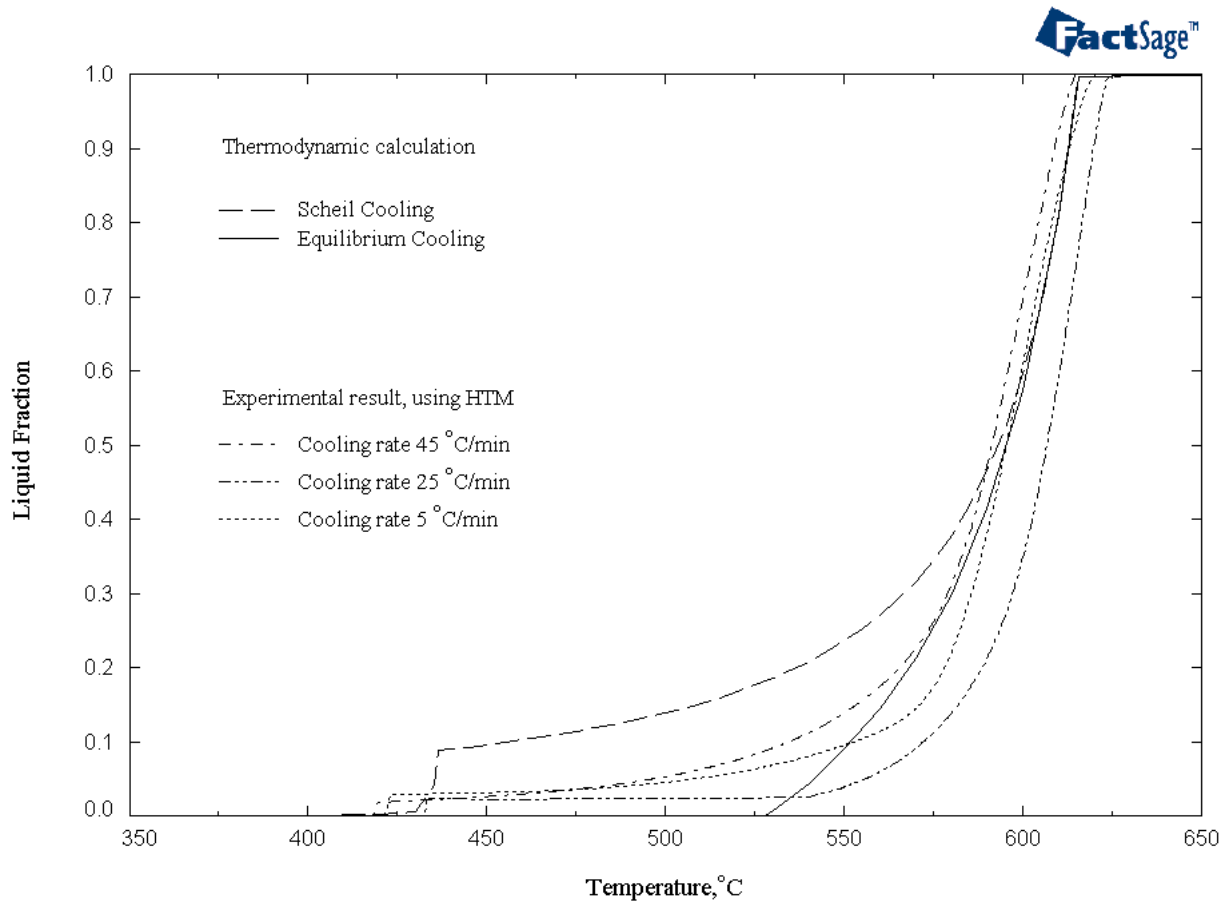


Figure 32: Comparison between experimental and calculated solidification curves of AM60B alloy

Figure 33 compares the thermodynamic predictions with the experimental results of the transition temperatures of AM60B alloy. Good agreement can be seen between the Scheil calculation and the corresponding experimental data. A 2% residual liquid cut-off limit has also been applied for the AM60B alloy and as a result the Scheil solidus temperature shifted for 5°C as shown in Figure 33.

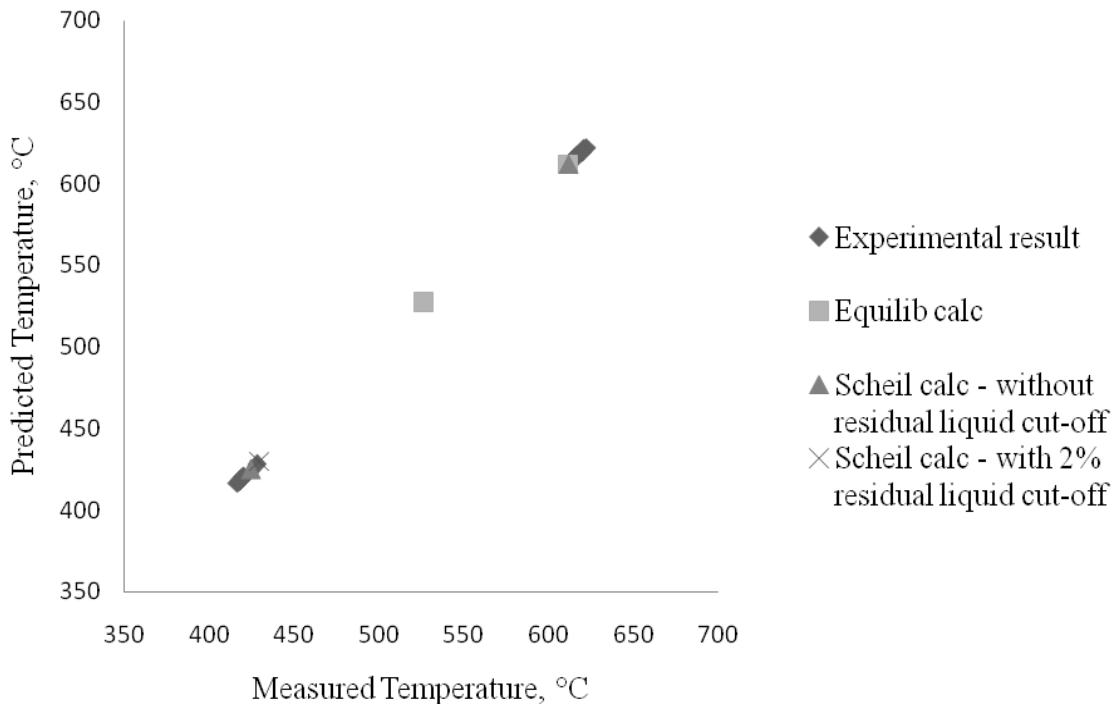


Figure 33: Comparison between experimental and calculated transition temperatures of AM60B alloy of AM60B alloy

The solidification curves of AE44 calculated under equilibrium and Scheil conditions are compared with the experimental curves in the Figure 34. The equilibrium cooling is indicated by solid line and the Scheil cooling is indicated by dashed line. According to both equilibrium and Scheil cooling condition, the solidification start with precipitation of  $Al_3La$  at around 750°C,

however, the amount of precipitation is very small and that is why it was not detected during the thermal analysis by DSC. The experimental results show that this alloy has a narrow solidification range comparing to the other two alloys as well as no bend was observed in the experimental solidification curve. However, the bend in the Scheil solidification curve indicates the formation of other phases such as  $Al_8Mn_5$  and  $Al_3Ce$  as described in the phase distribution section.

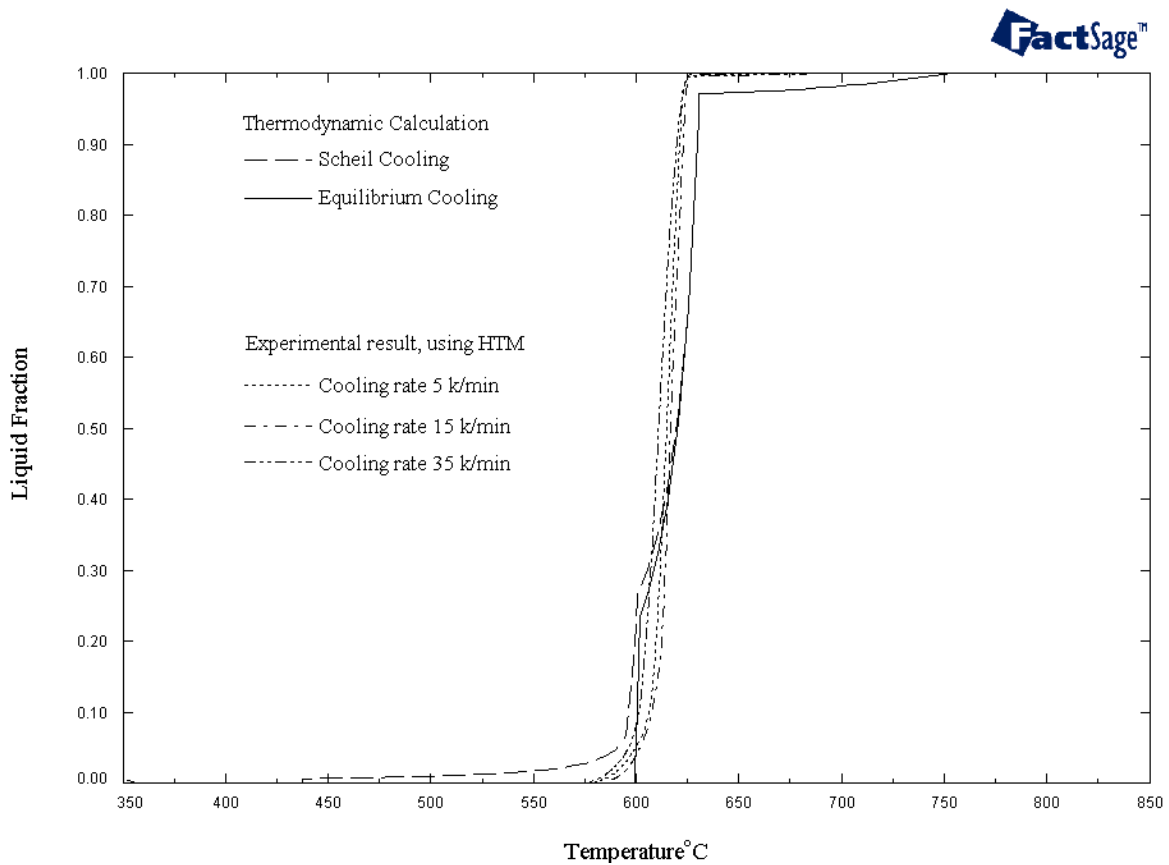


Figure 34: Comparison between experimental and calculated solidification curves of AE44 alloy

Figure 35 demonstrates detailed comparison between the thermodynamic prediction and experimental results of the transition temperatures of AE44 alloy. The difference in liquidus temperature is because of the formation of  $Al_3La$  phase. On the other hand, the difference in solidus temperature between Scheil and experimental results is due to the residual liquids which becomes extremely small or negligible in the later stage of solidification. For this alloy 2% residual liquid cut-off limit has also been applied which has increased the solidus temperature for 75°C as shown in Figure 35 and this has brought the Scheil solidus temperature much closure to the experimental solidus temperatures.

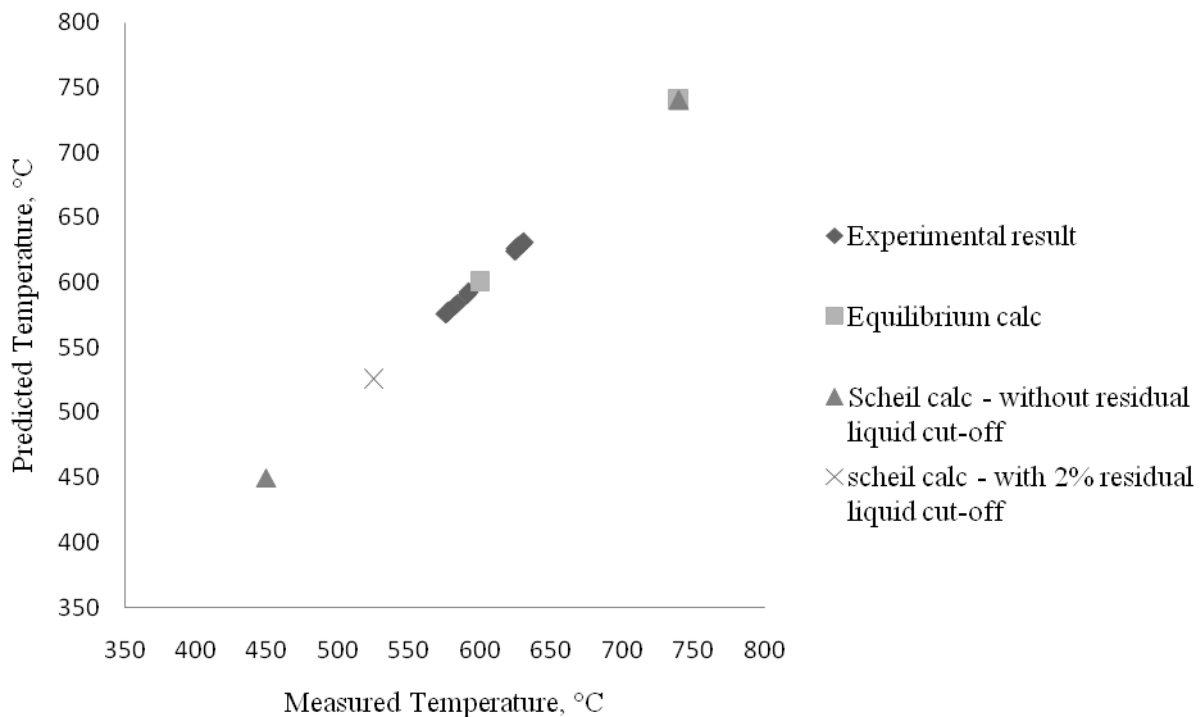


Figure 35: Comparison between experimental and calculated transition temperatures of AE44 alloy

#### 4.2.2 Phase Distribution of the Alloys

For better understanding of the phases that evolve during the course of solidification, phase assemblage diagrams were calculated for the three alloys using equilibrium and Scheil cooling conditions. Equilibrium solidification allows full diffusion in all phases. However, Scheil cooling does not allow diffusion in the precipitated solids; it only allows diffusion in the liquid solution. As the solidification process is a non-equilibrium process, it is expected that solidification during the real casting process will be closer to the Scheil simulation.

Figure 36 demonstrates the equilibrium solidification simulation of AZ91D alloy. During equilibrium cooling the first phase appears is  $\text{Al}_8\text{Mn}_5$ , but it decomposes into another phase and finally  $\text{Al}_6\text{Mn}$  phase appears. The liquid fraction drops significantly when  $\alpha$ -(Mg) starts to form. The equilibrium solidification ends at  $445.3^\circ\text{C}$ ; however because of the diffusion in the solid state  $\gamma$ - $\text{Mg}_{17}\text{Al}_{12}$  phase forms below the solidus temperature. The solidification sequences are shown in Table 14. Based on equilibrium cooling, the following  $\alpha$ -(Mg),  $\gamma$ - $\text{Mg}_{17}\text{Al}_{12}$  and  $\text{Al}_6\text{Mn}$  phases exist in the final stage of solidification of AZ91D alloy.

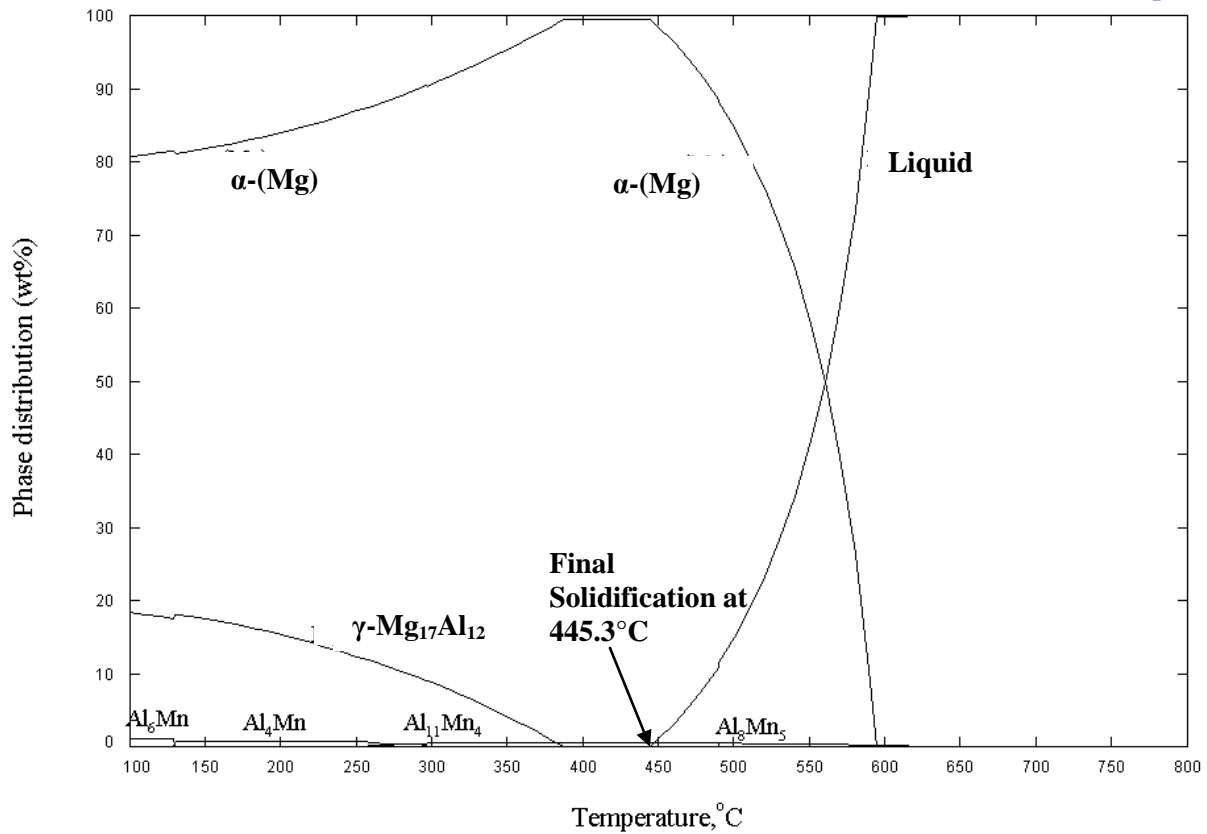


Figure 36: Equilibrium phase distribution of AZ91D alloy

Scheil solidification simulation of AZ91D alloy is shown in Figure 37. During Scheil cooling the first phase appears is Al<sub>8</sub>Mn<sub>5</sub> in a small volume fraction. The liquid fraction drops significantly when  $\alpha$ -(Mg) phase starts to form. The  $\gamma$ -Mg<sub>17</sub>Al<sub>12</sub> phase appears at 431.5°C and at the end of the solidification little amount of Mg<sub>6</sub>(Al,Zn)<sub>5</sub> phase appears; and the solidification ends at 358.5°C. The solidification sequences are shown in Table 14. According to Scheil cooling the existing phases in the final stage of solidification of AZ91D alloy are:  $\alpha$ -(Mg),  $\gamma$ -Mg<sub>17</sub>Al<sub>12</sub>, Al<sub>8</sub>Mn<sub>5</sub> and Mg<sub>6</sub>(Al,Zn)<sub>5</sub>.

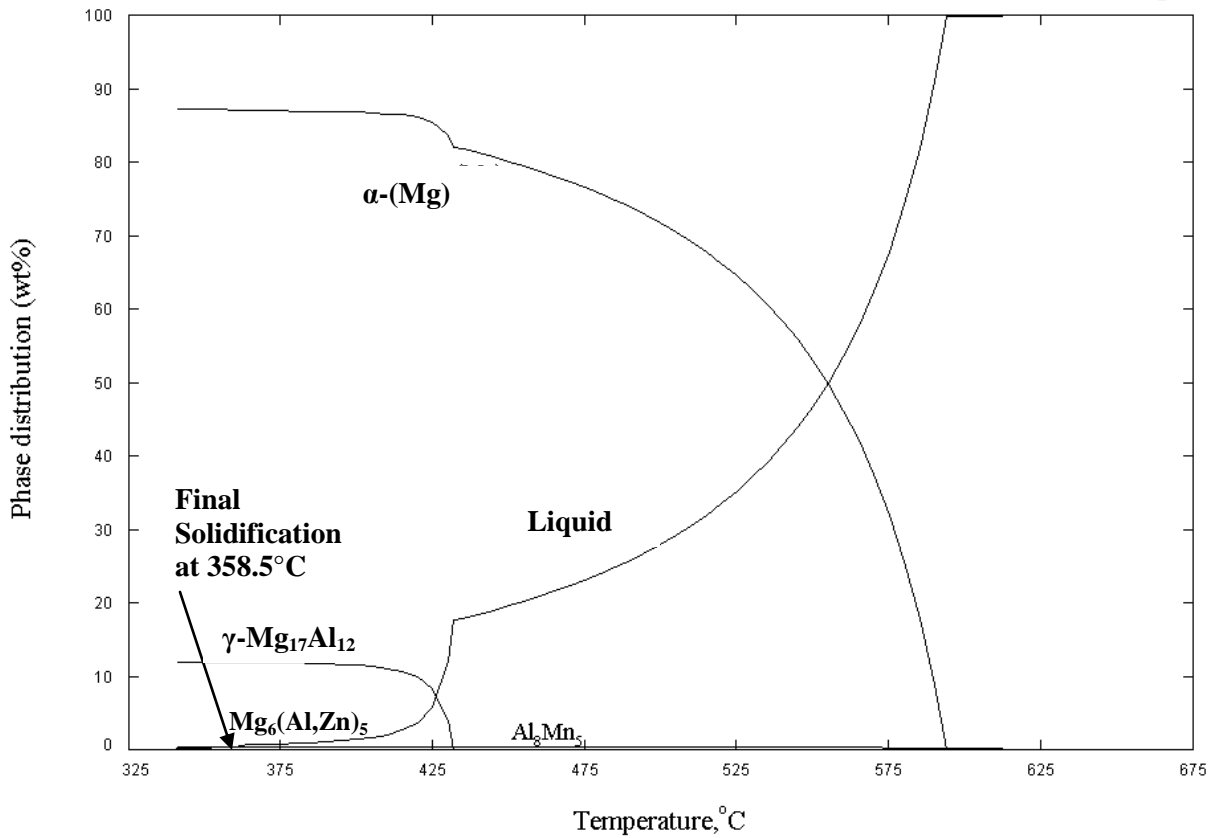


Figure 37: Scheil phase distribution of AZ91D alloy

Table 14: Sequence of Phase formation during equilibrium and Scheil solidification of AZ91D alloy

Equilibrium Cooling	Scheil Cooling
$L \rightarrow Al_8Mn_5$ at 613°C	$L \rightarrow Al_8Mn_5$ at 613°C
$L \rightarrow \alpha-(Mg) + Al_8Mn_5$ at 593°C	$L \rightarrow \alpha-(Mg) + Al_8Mn_5$ at 593°C
$\alpha-(Mg) + Al_8Mn_5 \rightarrow \alpha-(Mg) + \gamma-Mg_{17}Al_{12} + Al_{11}Mn_4$ at 385°C	$L \rightarrow \alpha-(Mg) + \gamma-Mg_{17}Al_{12} + Al_8Mn_5$ at 431°C
$\alpha-(Mg) + Al_{11}Mn_4 \rightarrow \alpha-(Mg) + \gamma-Mg_{17}Al_{12} +$	$L \rightarrow \alpha-(Mg) + \gamma-Mg_{17}Al_{12} + Al_8Mn_5 +$

$\text{Al}_4\text{Mn}$ at $275^\circ\text{C}$ $\alpha\text{-(Mg)} + \text{Al}_4\text{Mn} \rightarrow \alpha\text{-(Mg)} + \gamma\text{-Mg}_{17}\text{Al}_{12} +$ $\text{Al}_6\text{Mn}$ at $129^\circ\text{C}$	$\text{Mg}_6(\text{Al,Zn})_5$ at $420^\circ\text{C}$
--	--

Figure 38 demonstrates the equilibrium solidification simulation of AM60B alloy. Similar to the AZ91D alloy, during equilibrium cooling of AM60B the first phase appears is  $\text{Al}_8\text{Mn}_5$ , but it decomposes into another phase and finally  $\text{Al}_6\text{Mn}$  phase appears. The liquid fraction drops significantly when  $\alpha\text{-(Mg)}$  starts to form. For this alloy the equilibrium solidification ends at  $575.5^\circ\text{C}$ ; however because of the diffusion in the solid state  $\gamma\text{-Mg}_{17}\text{Al}_{12}$  phase forms much below the solidus temperature. The solidification sequences are shown in Table 15. Based on equilibrium cooling, the following  $\alpha\text{-(Mg)}$ ,  $\gamma\text{-Mg}_{17}\text{Al}_{12}$ ,  $\text{Al}_6\text{Mn}$  phases exist in the final stage of solidification of AM60B alloy.

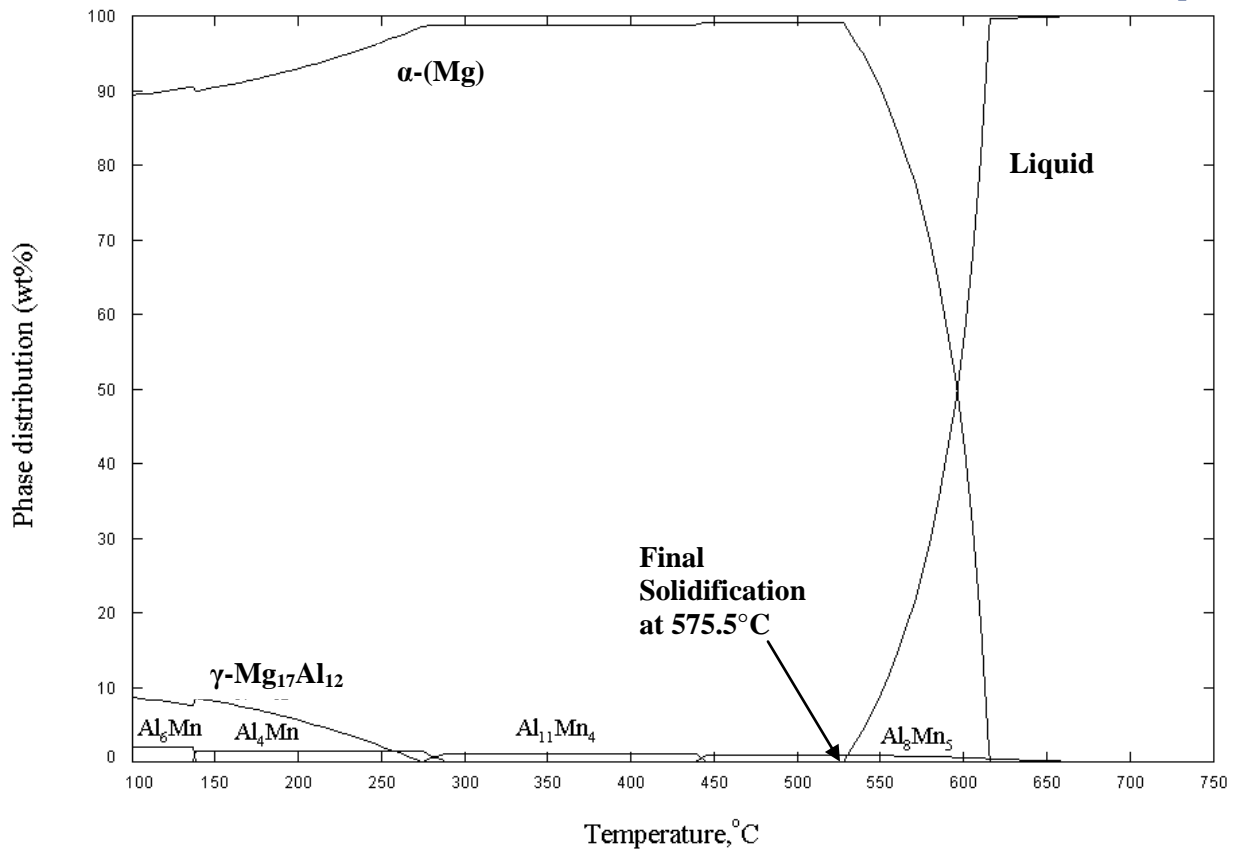


Figure 38: Equilibrium phase distribution of AM60B alloy

Scheil solidification simulation of AM60B alloy is shown in Figure 39. During Scheil cooling Al<sub>8</sub>Mn<sub>5</sub> phase appear at the beginning of solidification. The liquid fraction decreases significantly when  $\alpha$ -(Mg) phase starts to form. The  $\gamma$ -Mg<sub>17</sub>Al<sub>12</sub> phase appears at 435.6°C and at the end of the solidification little amount of Mg<sub>6</sub>(Al,Zn)<sub>5</sub> phase appears; and finally the solidification ends at 423.7°C. The solidification sequences are shown in Table 15. According to Scheil cooling during the solidification of AM60B alloy the existing phases in the final stage of solidification of AM60B alloy are:  $\alpha$ -(Mg),  $\gamma$ -Mg<sub>17</sub>Al<sub>12</sub> and Al<sub>8</sub>Mn<sub>5</sub>.

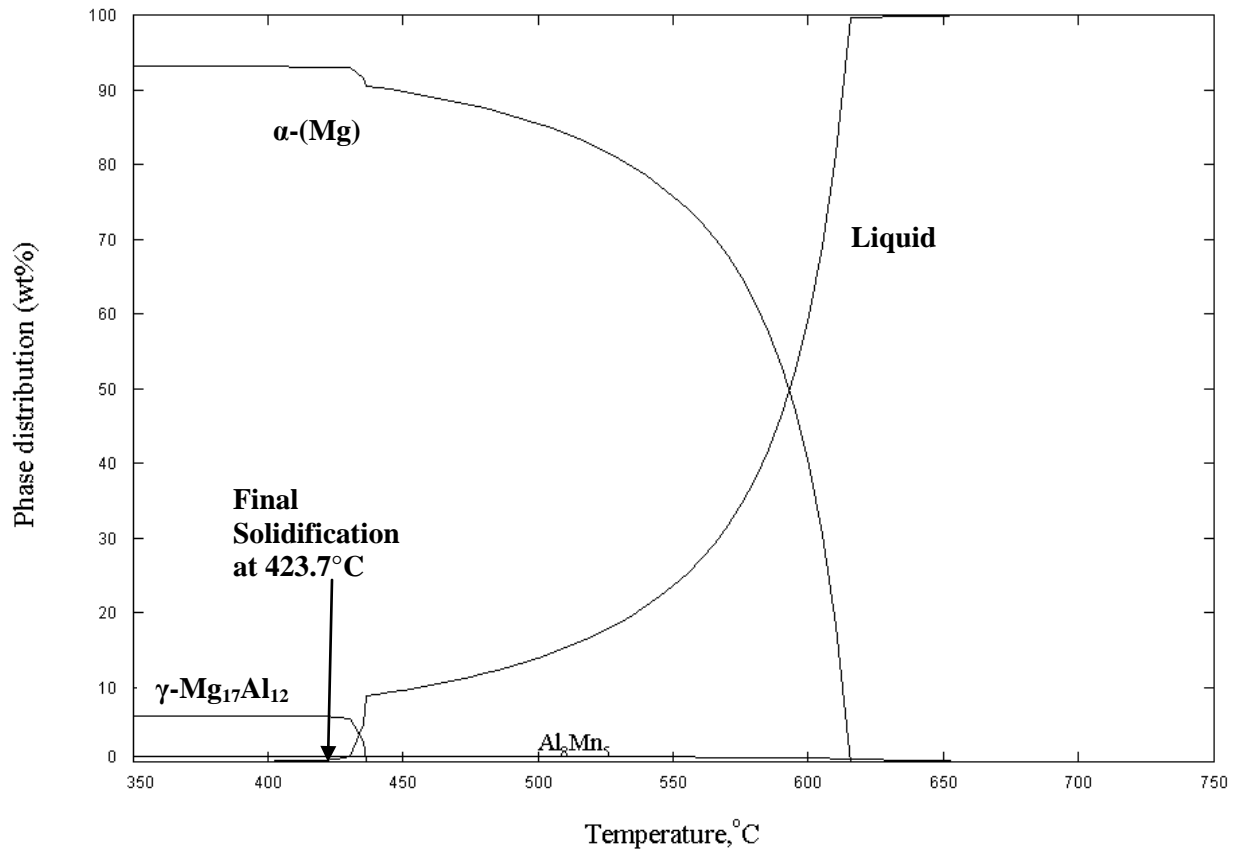


Figure 39: Scheil phase distribution of AM60B alloy

Table 15: Sequence of phase formation during equilibrium and Scheil solidification of AM60B

Equilibrium Cooling	Scheil Cooling
$L \rightarrow Al_8Mn_5$ at 656°C	$L \rightarrow Al_8Mn_5$ at 656°C
$L \rightarrow \alpha-(Mg) + Al_8Mn_5$ at 615°C	$L \rightarrow \alpha-(Mg) + Al_8Mn_5$ at 615°C
$L + Al_8Mn_5 \rightarrow \alpha-(Mg) + Al_{11}Mn_4$ at 442°C	$L \rightarrow \alpha-(Mg) + \gamma-Mg_{17}Al_{12} + Al_8Mn_5$ at 435°C
$\alpha-(Mg) + Al_{11}Mn_4 \rightarrow \alpha-(Mg) + \gamma-Mg_{17}Al_{12} + Al_4Mn$ at 271°C	
$\alpha-(Mg) + Al_4Mn \rightarrow \alpha-(Mg) + \gamma-Mg_{17}Al_{12} + Al_6Mn$ at 136°C	

The equilibrium solidification simulation of AE44 alloy is shown in Figure 40 and the Scheil simulation is shown in Figure 41. For both equilibrium and Scheil condition the beginning of the solidification process is quite similar. In both conditions, the solidification starts at 745°C with the precipitation of Al<sub>3</sub>La phase. A small amount of liquid turns into solid until α-(Mg) starts to form at 630°C. The equilibrium solidification process ends at 600.2°C and Al<sub>8</sub>Mn<sub>5</sub> phase appears right before the end of solidification. Because of the diffusion in the solid state in equilibrium condition Al<sub>11</sub>Ce<sub>3</sub> phase appears right after the solidus temperature. Based on equilibrium cooling α-(Mg), Al<sub>3</sub>La, Al<sub>11</sub>Ce<sub>3</sub> and Al<sub>8</sub>Mn<sub>5</sub> phases exist in the final stage of solidification of AE44 alloy.

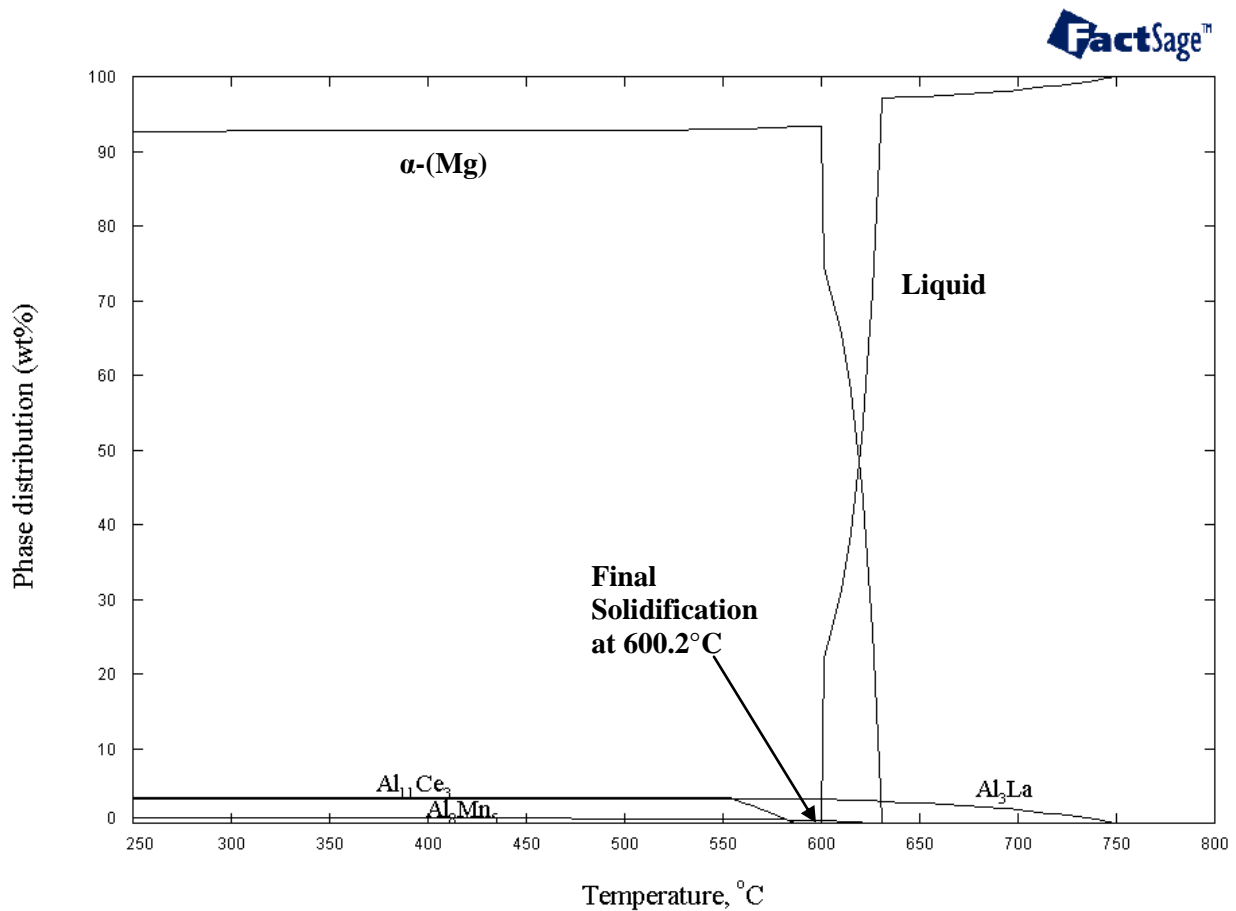


Figure 40: Equilibrium phase distribution of AE44 alloy

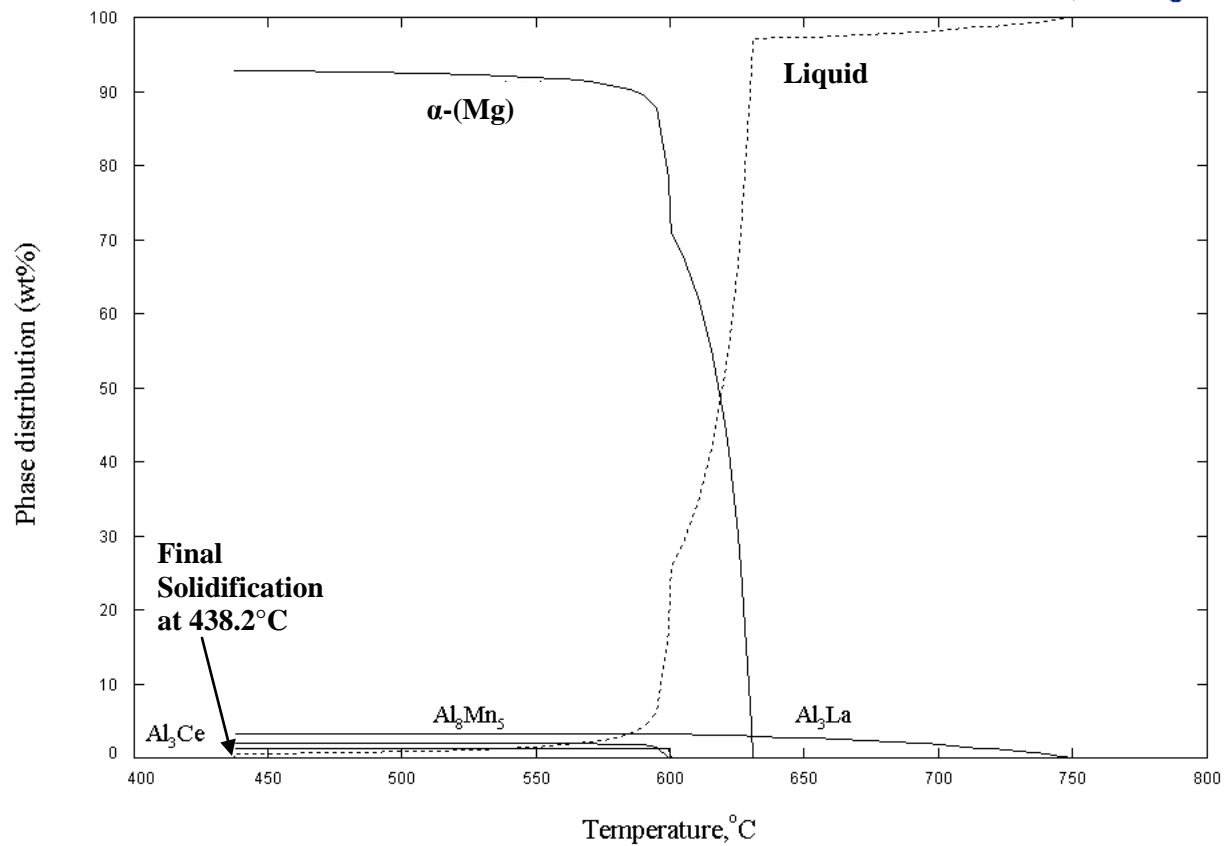


Figure 41: Scheil phase distribution of AE44 alloy

Table 16: Sequence of phase formation during equilibrium and Scheil solidification of AE44

Equilibrium Cooling	Scheil Cooling
$L \rightarrow \text{Al}_3\text{La}$ at 745°C	$L \rightarrow \text{Al}_3\text{La}$ at 745°C
$L \rightarrow \alpha\text{-(Mg)} + \text{Al}_3\text{La}$ at 630°C	$L \rightarrow \alpha\text{-(Mg)} + \text{Al}_3\text{La}$ at 630°C
$L \rightarrow \alpha\text{-(Mg)} + \text{Al}_3\text{La} + \text{Al}_8\text{Mn}_5$ at 612°C	$L \rightarrow \alpha\text{-(Mg)} + \text{Al}_3\text{La} + \text{Al}_8\text{Mn}_5$ at 600°C
$L \rightarrow \alpha\text{-(Mg)} + \text{Al}_3\text{La} + \text{Al}_8\text{Mn}_5 + \text{Al}_{11}\text{Ce}_3$ at 583°C	$L \rightarrow \alpha\text{-(Mg)} + \text{Al}_3\text{La} + \text{Al}_8\text{Mn}_5 + \text{Al}_3\text{Ce}$ at 598°C

On the other hand, during Scheil solidification  $\text{Al}_3\text{Ce}$  phase appears at 598°C and solidification ends at 438.2°C. According to Scheil cooling  $\alpha$ -(Mg),  $\text{Al}_3\text{La}$ ,  $\text{Al}_3\text{Ce}$  and  $\text{Al}_8\text{Mn}_5$  phases exist in

the final stage of solidification of AE44 alloy. The solidification sequences of AE44 alloy are shown in Table 16.

The volume fraction of the three alloys have been calculated both in equilibrium and Scheil cooling conditions and summarized in Tables 17 and 18. Volume fractions under the equilibrium condition have been measured until the room temperature is reached as under equilibrium condition diffusion occurs even after the solidus temperature. However, volume fractions under Scheil simulation have been measured at the solidus temperature.

Table 17: Equilibrium solidification simulation results of the alloys

Alloys	Volume fraction					
	$\alpha$ - (Mg)	$\gamma$ -Mg <sub>17</sub> Al <sub>12</sub>	Al <sub>6</sub> Mn	Al <sub>8</sub> Mn <sub>5</sub>	Al <sub>11</sub> Ce <sub>3</sub>	Al <sub>3</sub> La
AZ91D	80.6	18.3	1.07	-	-	-
AM60B	89.23	8.61	2.15	-	-	-
AE44	92.61	-	-	0.76	3.38	3.23

Table 18: Scheil solidification simulation results of the alloys

Alloys	Volume fraction					
	$\alpha$ - (Mg)	$\gamma$ -Mg <sub>17</sub> Al <sub>12</sub>	Al <sub>8</sub> Mn <sub>5</sub>	Mg <sub>6</sub> (Al,Zn) <sub>5</sub>	Al <sub>3</sub> La	Al <sub>3</sub> Ce
AZ91D	87.1	12.05	0.4	0.45	-	-
AM60B	93.07	6.15	0.62	-	-	-
AE44	92.77	-	2.01	-	3.23	1.23

As the equilibrium condition allows enough time and solid state diffusion to the solidification process, some portion of the primary  $\alpha$ -(Mg) phase contributes in forming  $\gamma$ -Mg<sub>17</sub>Al<sub>12</sub> phase. So, for both AZ91D and AM60B alloys the volume fraction of primary  $\alpha$ -(Mg) phase decreases and the volume fraction of  $\gamma$ -Mg<sub>17</sub>Al<sub>12</sub> phase increases in equilibrium cooling condition comparing with the Scheil cooling condition. For the AE44 alloy the volume fraction of  $\alpha$ -(Mg) phase remains almost same both in equilibrium and Scheil cooling condition; however some change in secondary phases is observed. Some of these behaviors are also supported by the microstructure analysis discussed in section 4.3.

### **4.3 Microstructural Analysis**

The microstructural characterization and phase analysis has been described in this section. Optical microscopy has been used for this purpose. The as-cast samples as well as the post-DSC samples were analyzed and the effect of different cooling rates on microstructure, grain size and eutectic morphology were observed. With higher cooling rate a greater degree of constitutional undercooling is expected, which in turn results in an increase in the number of effective nucleants and a finer grain size.

#### **4.3.1 AZ91D**

The general microstructure of the AZ91D is shown in Figures 42 and 43. This alloy appears to have  $\alpha$ -(Mg) phase and eutectic phase around the primary grain with large dendritic morphology. Both coarse and fine eutectic particles are found in the microstructure. The coarse particles are grown from the liquid and the fine particles are grown as discontinuous precipitation from the supersaturated  $\alpha$ -(Mg) matrix in the high-concentration region. Due to high aluminum content in AZ91D, the fraction of eutectic phase is clearly greater than that of AM60B. With a closer inspection of the eutectic region, its morphology is found to be highly discontinuous. In the as-cast samples the volume fraction of precipitated eutectic phases is comparatively higher than that of the post-DSC samples and it is attributed to the decrease of time for back diffusion in the solid. This is because during solidification, back diffusion in the solid causes a reduction in the eutectic fraction and if the cooling rate increases there is less time available for back diffusion resulting in increasing eutectic fraction [74].

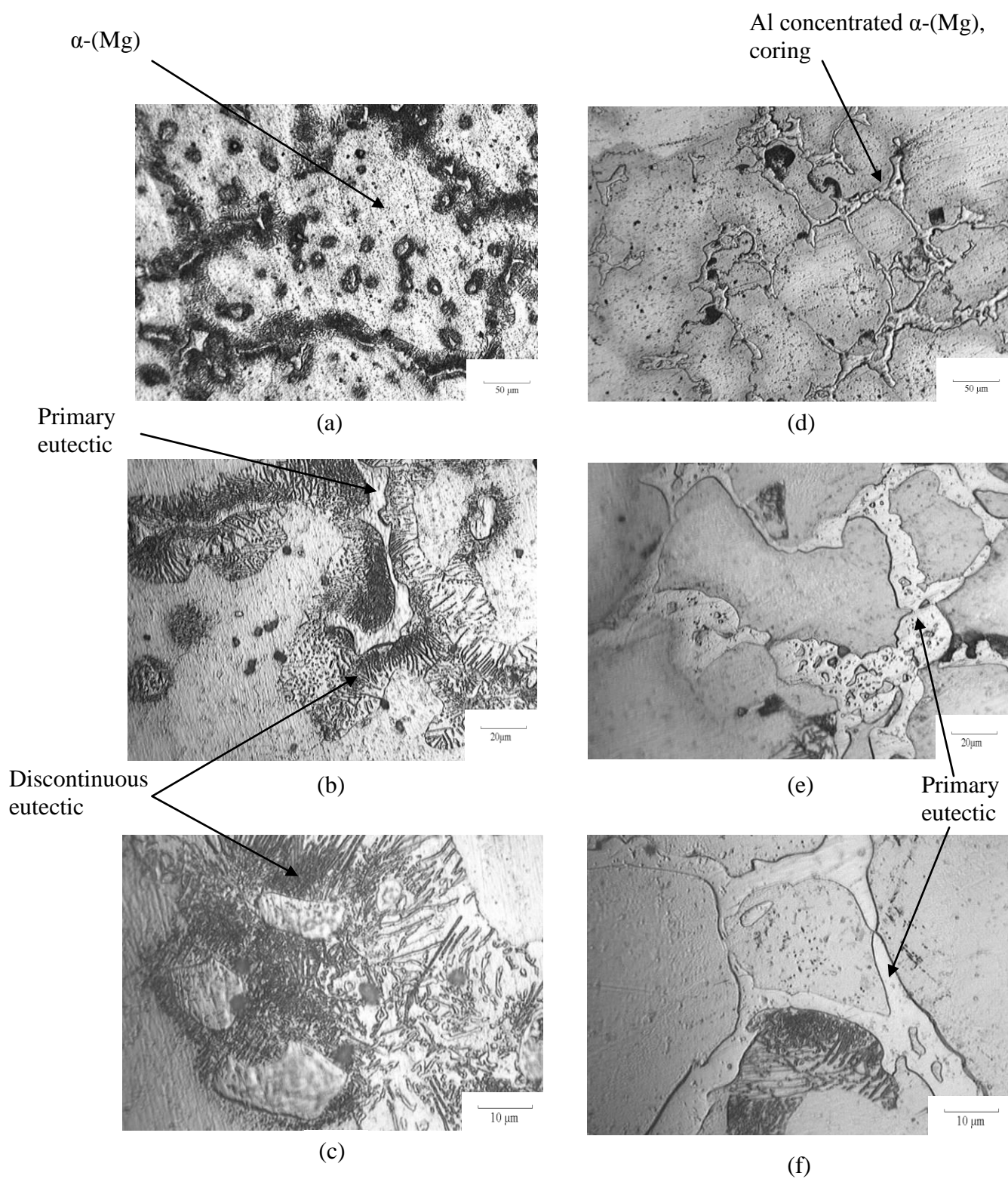


Figure 42: As-cast microstructure of AZ91D: (a)100X (b) 500X (c) 1000X; Post-DSC microstructure of AZ91D, DSC cooling rate 5°C/min: (d) 100X (e) 500X (f) 1000X.

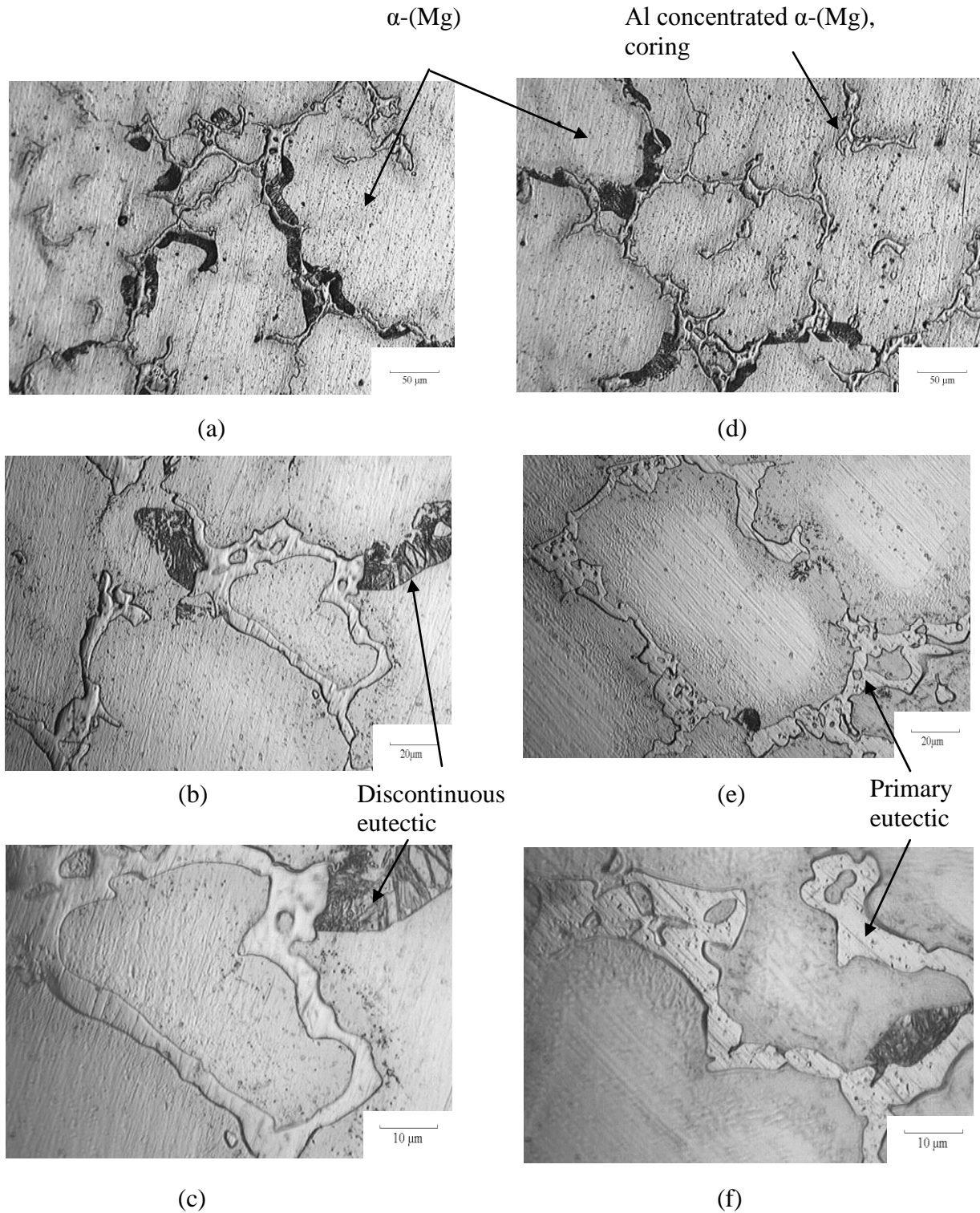


Figure 43: Post-DSC microstructure of AZ91D, DSC cooling rate 25°C/min: (a)100X (b) 500X (c) 1000X; Post-DSC microstructure of AZ91D, DSC cooling rate 45°C/min: (d) 100X (e) 500X (f) 1000X

Thermodynamic calculation also predicted that the volume fraction of the eutectic increases in Scheil cooling condition which is consistent with experimental results. In the post-DSC samples less amount of discontinuous precipitation were observed. The darker region in the surroundings of the primary  $\alpha$ -(Mg) phase in the post-DSC samples is Al concentrated  $\alpha$ -(Mg) and this is indicated by coring [75].

#### **4.3.2 AM60B**

The general microstructure of the as-cast samples of AM60B alloy can be seen Figure 44. The AM60B alloy forms a primary phase of  $\alpha$ -(Mg) matrix, the secondary phases contain Al-Mn compounds, and the eutectic. The secondary phase of Al-Mn appears to have needle like and polygonal morphologies. In the as-cast microstructure Al-concentrated  $\alpha$ -(Mg) is observed and this is because of the rapid cooling rate taking place during HPDC process. In addition, because of the high solidification rate of HPDC, divorced eutectic [ $\alpha$ -(Mg) +  $\gamma$ -Mg<sub>17</sub>Al<sub>12</sub>] structure forms in AM60B alloy. At lower cooling rate the eutectic structure is assumed to be partially divorced as shown in Figures 45 and 46.

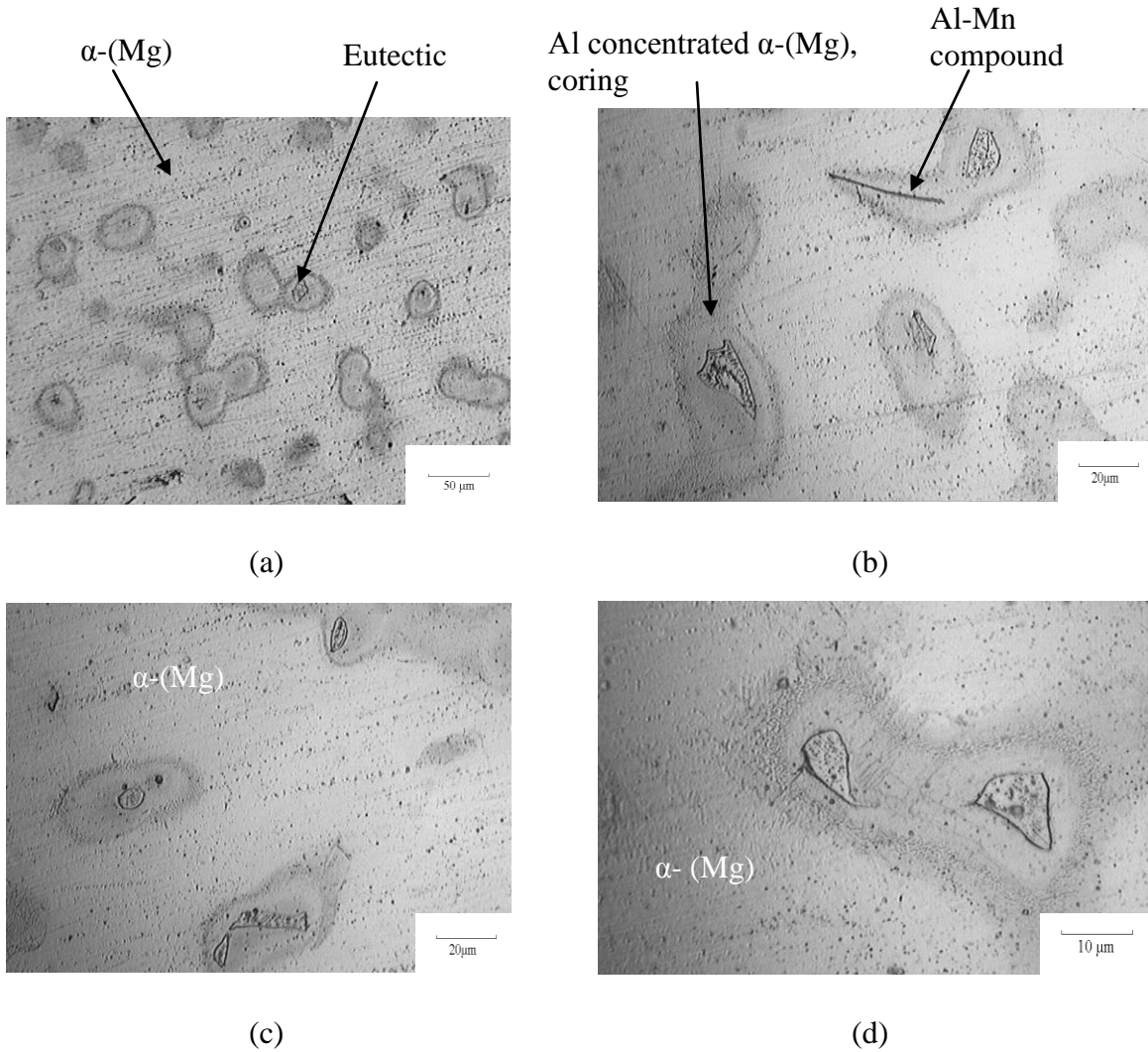


Figure 44: As-cast microstructure of AM60B: (a)100X (b) 500X (c) 500X (d) 1000X

The microstructure analysis of the post-DSC samples was done to observe the effect of different cooling rates on the microstructure and representative micrographs are summarized in Figures 45 and 46. In the slow cooling rate such as  $5^{\circ}\text{C}/\text{min}$ , Figure 45 shows partially divorced eutectic [ $\alpha$ -(Mg) +  $\gamma$ - $\text{Mg}_{17}\text{Al}_{12}$ ] structure and lamellar  $\gamma$ - $\text{Mg}_{17}\text{Al}_{12}$  precipitates. It is believed that the lamellar  $\gamma$ - $\text{Mg}_{17}\text{Al}_{12}$  structure is formed after solidification via discontinuous precipitation from  $\alpha$ -(Mg) supersaturated solution. Such lamellar structure was not observed in the as-cast samples.

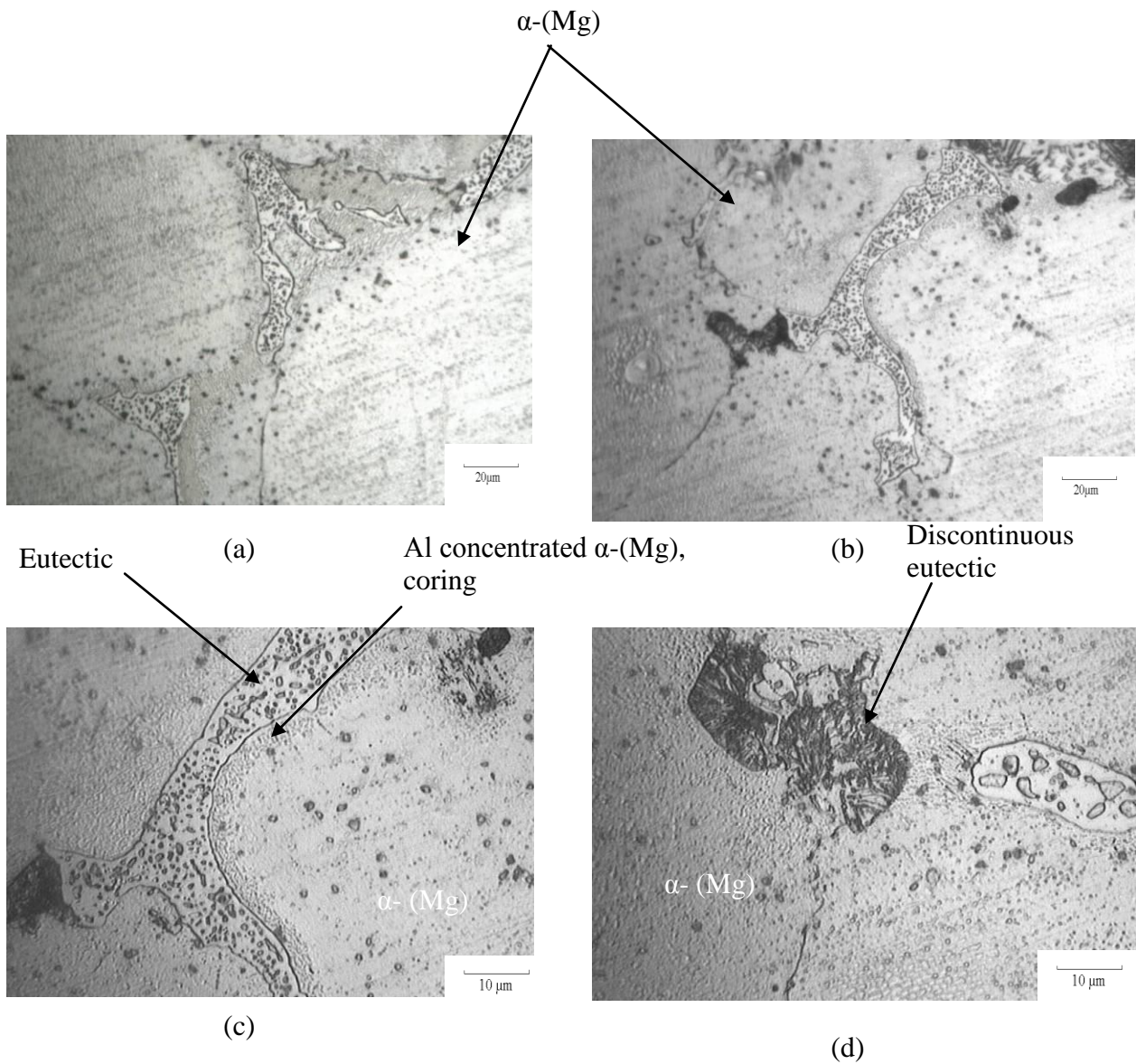


Figure 45: Post-DSC microstructure of AM60B, DSC cooling rate 5°C/min: (a) 500X (b) 500X (c) 1000X (d) 1000X

The post-DSC microstructure shows a large amount of eutectic, however, the presence of eutectic in the post-DSC samples is highly segregated to the grain boundaries and coring was clearly observed.

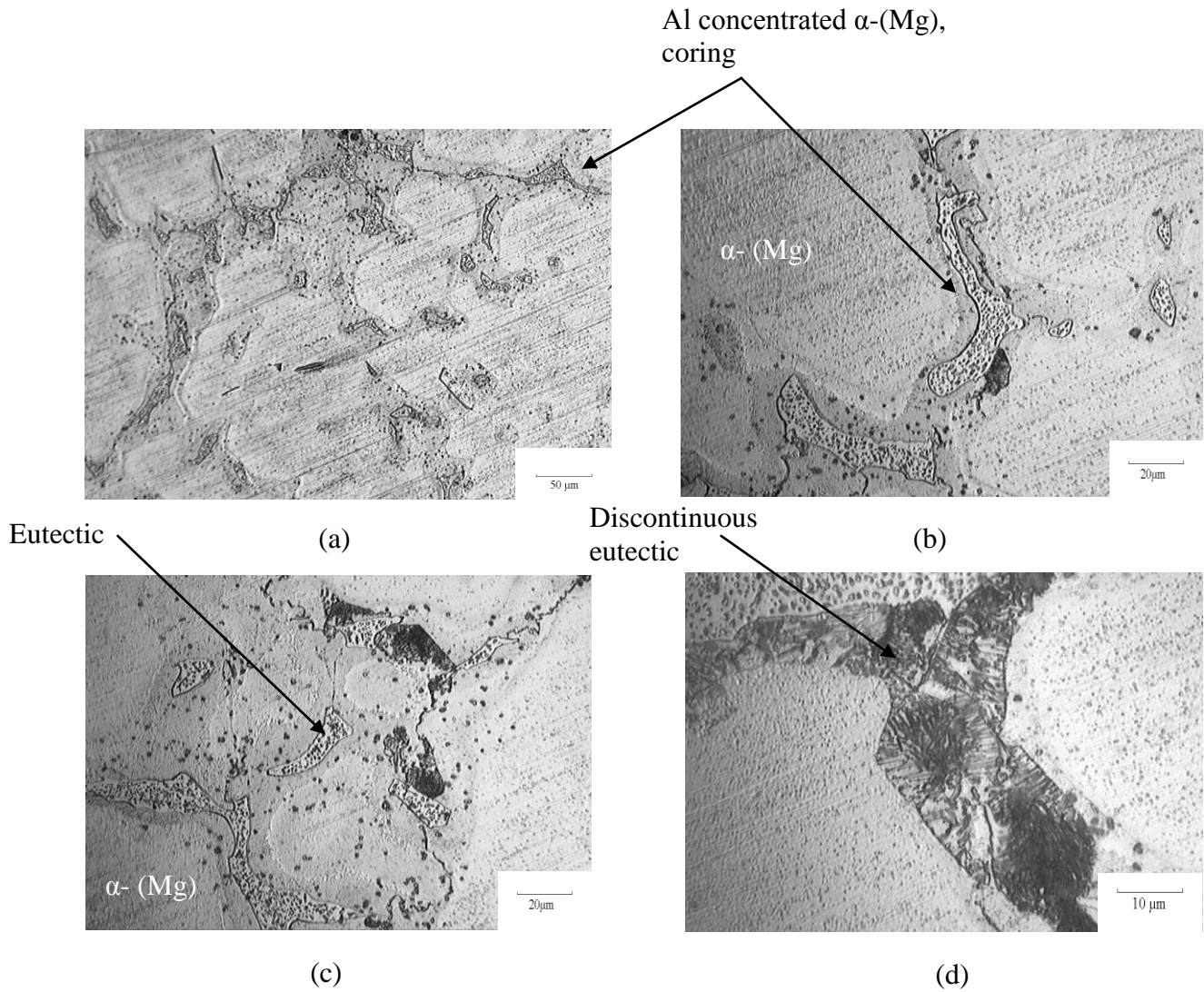


Figure 46: Post-DSC microstructure of AM60B, DSC cooling rate 45°C/min: (a) 100X (b) 500X (c) 500X (d) 1000X

### 4.3.3 AE44

The microstructure of the AE44 alloy is characterized by  $\alpha$ -(Mg) solid solution structure with acicular and irregular precipitations. These secondary phases are composed mainly of Al, Ce and La. The optical images of the AE44 alloy are shown in Figure 47.

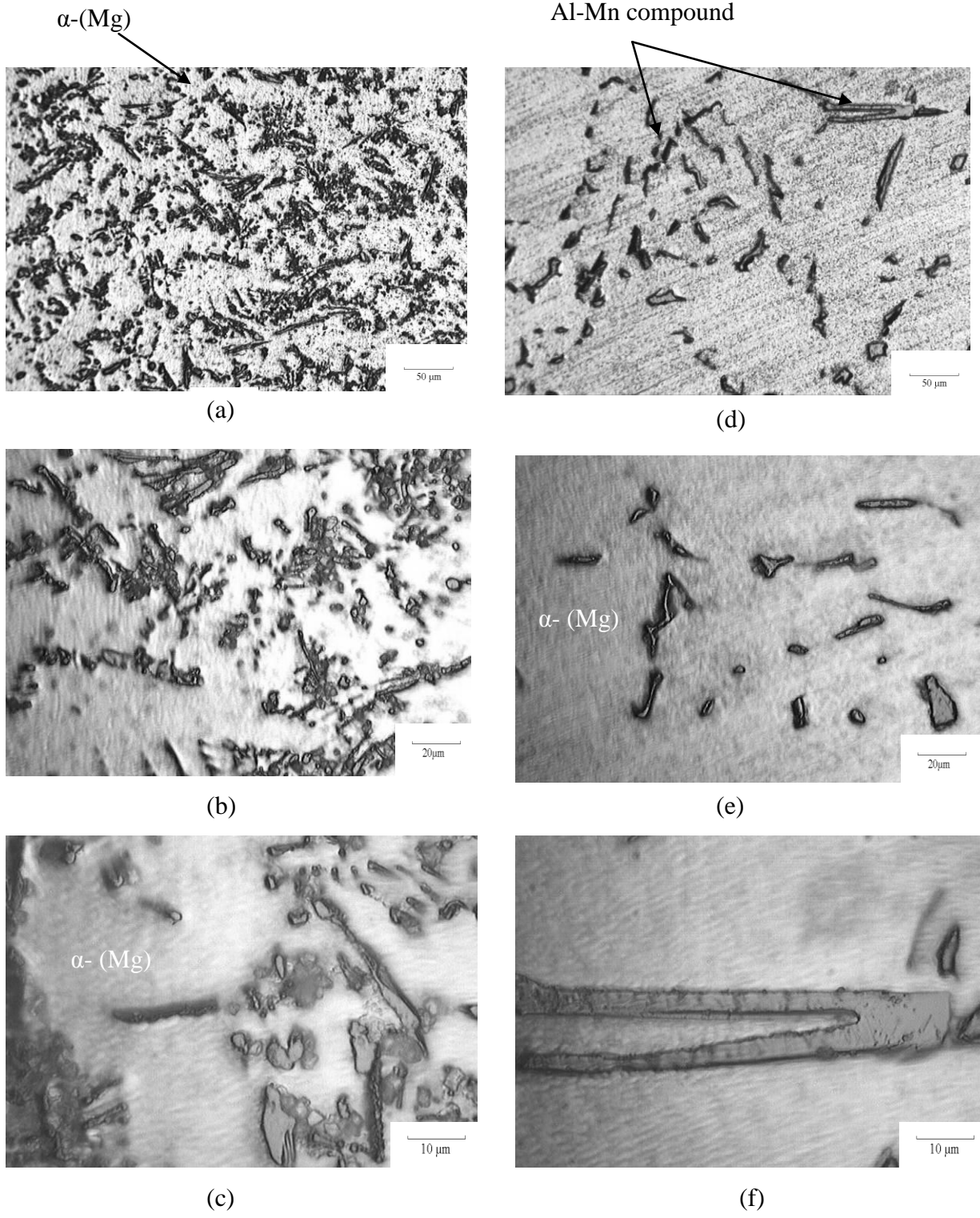


Figure 47: As-cast microstructure of AE44 ( a) 100X (b) 500X (c) 1000X; Post-DSC microstructure of AE44, DSC cooling rate 5°C/min (d) 100X (e) 500X (f) 500X

The as-cast microstructure in Figure 47(a), 47(b) and 47(c) show a large amount of secondary phases randomly distributed in  $\alpha$ -(Mg) phase. Whereas in the post-DSC microstructures of the AE44 alloy solidified at 5°C/min as shown in Figure 47(d), 47(e) and 47(f) reveal the significant reduction of the secondary phases. In addition, more post-DSC microstructures have also been investigated to observe the effect of various cooling rates on the microstructure and the images are summarized in Figures 48 and 49.

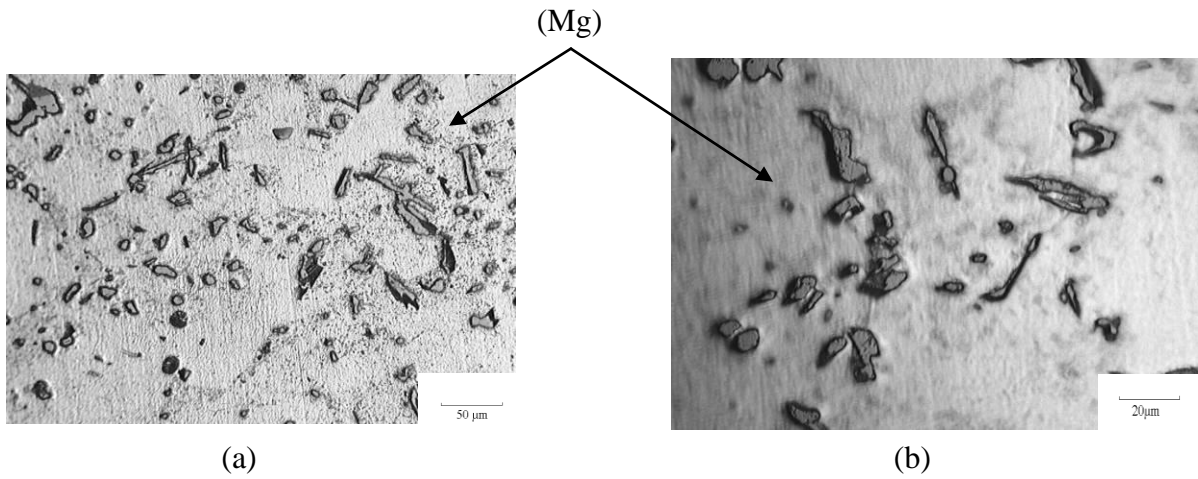


Figure 48: Post-DSC microstructure of AE44, DSC cooling rate 10°C/min, (a) 500X (b) 1000X

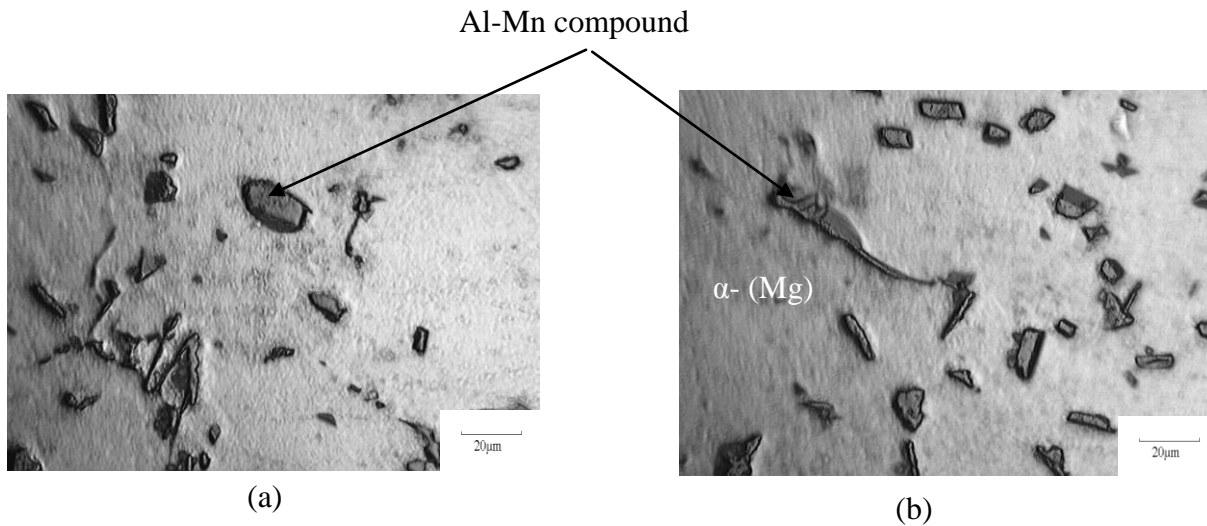


Figure 49: Post-DSC microstructure of AE44, DSC cooling rate 20°C/min, (a) 500X (b) 1000X

The as-cast and post-DSC microstructure reveal the fact that with increasing cooling rate the amount of secondary phase increases as observed in Figures 47, 48 and 49. The fact has been well demonstrated for a number of binary systems both experimentally and theoretically [74], however it has been well demonstrated here for the ternary alloys as well.

#### 4.4 Extrapolation of the Latent Heat of Solidification and Phase Transition Temperatures

In this section, a relation has been developed between cooling rate and latent heat of solidification as well as phase transition temperatures. From the experimental data of latent heat of solidification versus cooling rate, it is obvious that the latent heat of solidification has an increasing trend with increasing the cooling rate. This trend verifies the fact that the latent heat of solidification is sensitive to the transition speed. To develop the relationship between latent heat of solidification and cooling rate a general power equation has been used as suggested by [35, 63-66]:

$$L = L_0 + At^\alpha \dots\dots\dots(5)$$

Where  $\alpha$  is the scaling exponent,  $A$  is constant,  $L_0$  the latent heat at quasistatic state and  $t$  is the cooling rate. The scaling exponent  $\alpha$  and the constant  $A$  are obtained using least square method by putting the experimental data of Tables 8, 10 and 12 in equation (5) and the results are summarized in Table 19. The quasistatic latent heat  $L_0$  was obtained from the experimental data from Figure 29 by extrapolating to zero cooling rate.

After obtaining all the parameters, it is possible to predict the change in latent heat of solidification at high cooling rates as shown in Figures 50 to 52. Some experimental data at extremely high cooling rates using Universal Metallurgical Simulator and Analyzer (UMSA)

equipment are available from Reade [70], University of Windsor through personal communication. Reasonable agreement has been observed between the calculation and experimental data except for AE44 alloy.

Table 19: Extrapolation parameters of Latent heat of solidification

	$\alpha$	$L_0$	A
AZ91D	0.82	305.5	18.8
AM60B	0.86	291.4	16.7
AE44	0.69	379.8	11.6

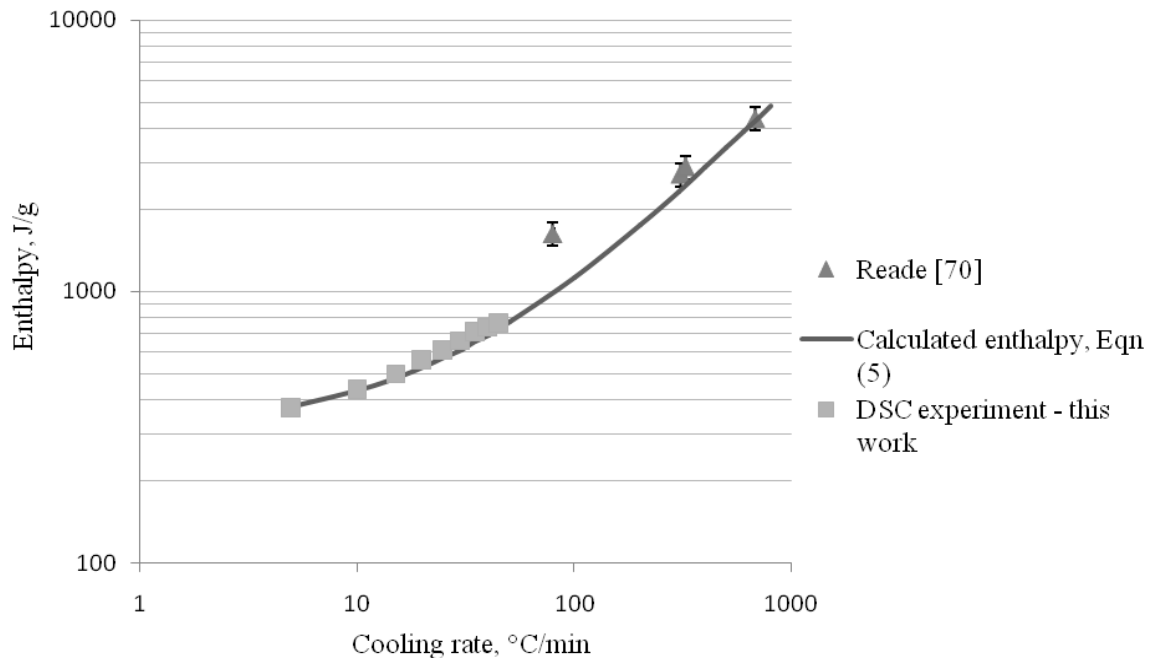


Figure 50: Extrapolation of latent heat of solidification of AZ91D to high cooling rates in double logarithmic graph

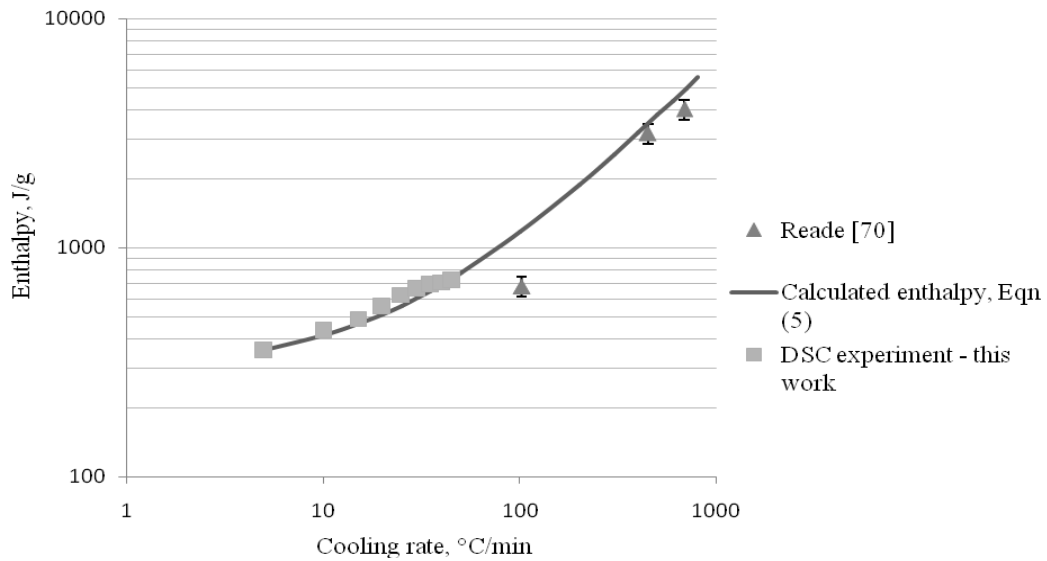


Figure 51: Extrapolation of latent heat of solidification of AM60B to high cooling rates in double logarithmic graph

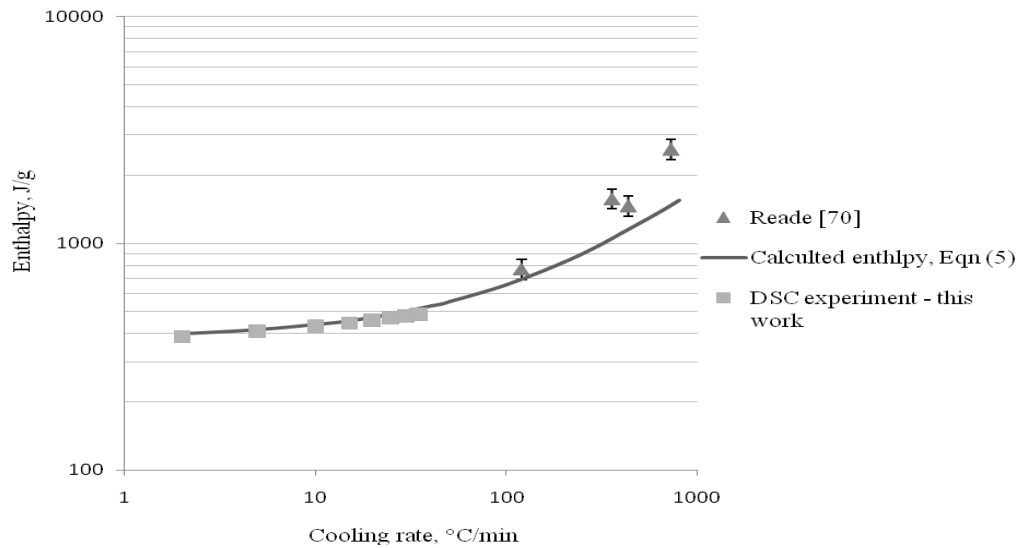


Figure 52: Extrapolation of latent heat of solidification of AE44 to high cooling rates in double logarithmic graph

Similar type of power law equation was used to develop the relationship between transition temperatures and cooling rates:

$$T = T_0 \pm Bt^n \dots\dots\dots(6)$$

Where  $n$  is a scaling exponent,  $t$  is the cooling rate,  $T_0$  ( $T_{0s}$ - *quasistatic solidus temperature* /  $T_{0l}$  - *quasistatic liquidus temperature*) the transition temperature at quasistatic state,  $B$  constant. The scaling exponent  $n$  and the constant  $B$  are obtained by putting the experimental data of Tables 8, 10 and 12 in equation (6) and the results are shown in Tables 20 and 21. The quasistatic transition temperature  $T_{0s}$  and  $T_{0l}$  were obtained from Figures 19, 23 and 27 by extrapolating to zero cooling rate.

Table 20: Liquidus temperature extrapolation parameters

	n	T <sub>0l</sub>	B
AZ91D	0.63	594.5	0.50
AM60B	0.94	615.9	0.07
AE44	0.50	625.4	0.30

Table 21: Solidus temperature extrapolation parameters

	n	T <sub>0s</sub>	B
AZ91D	0.65	427.1	1.05
AM60B	0.41	431.8	3.73
AE44	0.27	595.3	5.76

Finally, after getting all the parameters the transition temperatures were predicted at high cooling rates and compared with the available set of experimental data of Reade [70]. Figures 53 to 55 illustrate these calculations and comparisons. Good agreements have been obtained between the experimental data and the calculations.

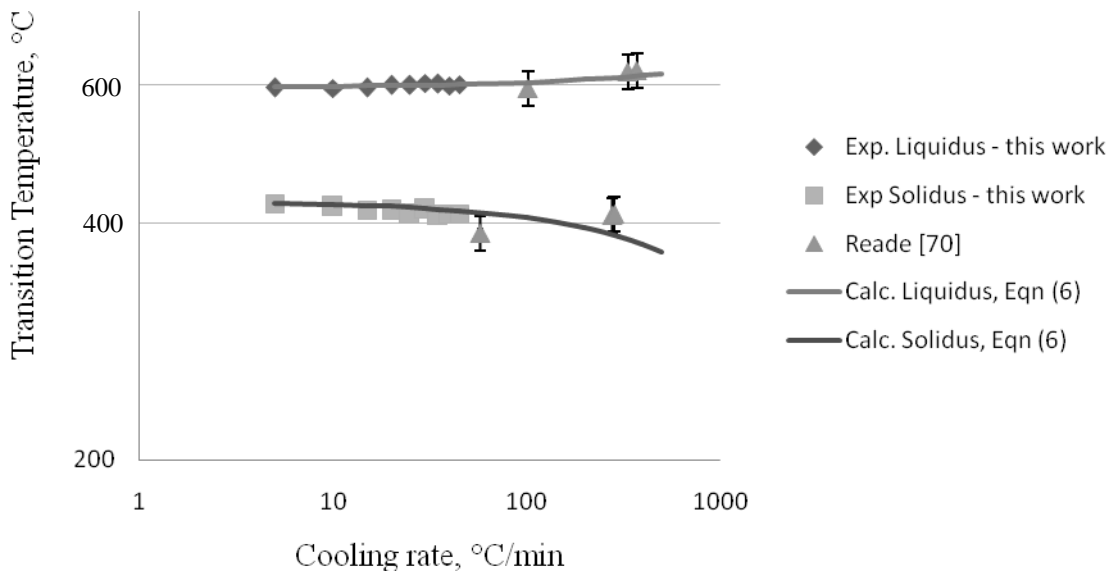


Figure 53: Extrapolation of the transition temperatures of AZ91D to high cooling rates in double logarithmic graph

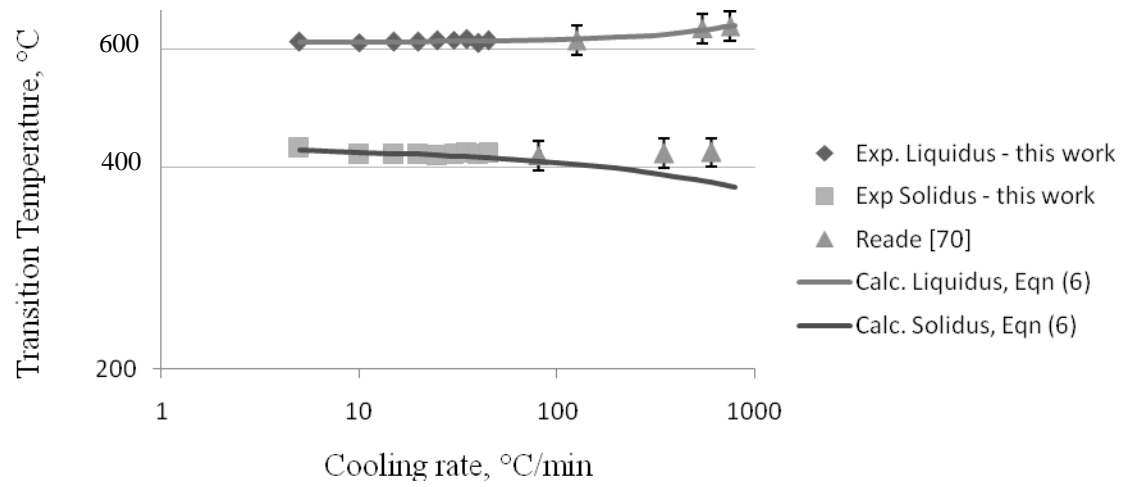


Figure 54: Extrapolation of the transition temperatures of AM60B to high cooling rates in double logarithmic graph

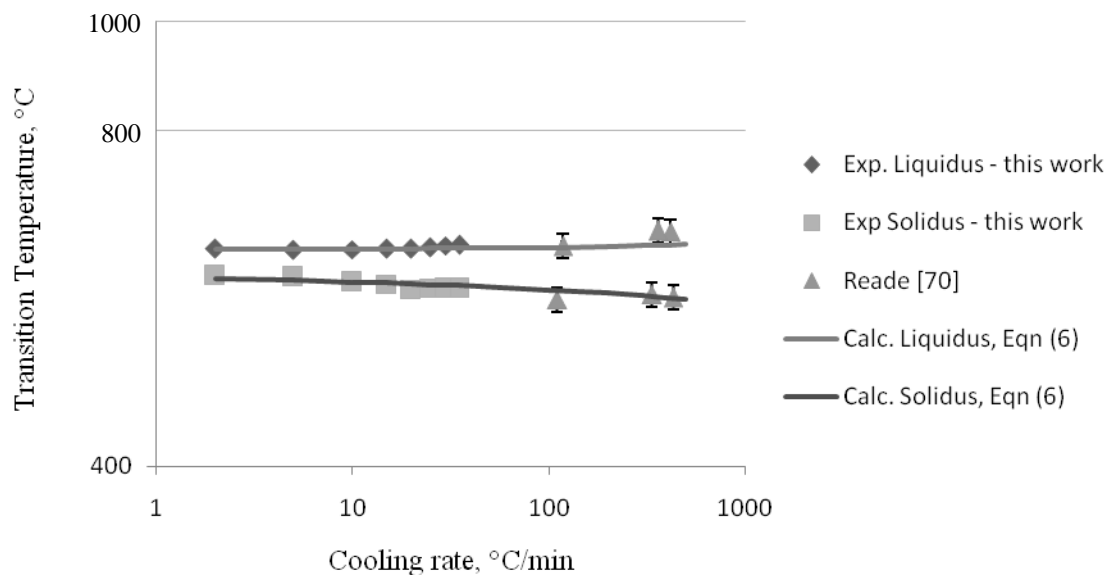


Figure 55: Extrapolation of the transition temperatures of AE44 to high cooling rates in double logarithmic graph

# CHAPTER 5

## *Conclusions, Contributions and Recommendations for Future Work*

---

### **5.1 Conclusions**

Solidification behavior and microstructural analysis have been carried out on three commercial magnesium alloys using both experimental analysis and thermodynamic calculation. Based on the current work the following conclusion can be drawn.

DSC has been used to get the thermo-physical properties such as transition temperatures and solidification enthalpies at different cooling rates. For all the three alloys it is apparent that cooling rate has very little effect on liquidus temperature in the range of cooling rate studied here. However, solidus temperature somewhat decreases with increasing cooling rate. For all the alloys studies here the latent heat of solidification increases significantly with increasing cooling rate.

Solidification curves at different cooling rates have been drawn from the experimental data using HTM. Solidification curves have also been calculated both in equilibrium and Scheil model and good consistency was found between Scheil calculation and experimental results. Phase distributions, volume fraction of the phases and phase formation sequences have also been calculated and analyzed.

Optical microscope has been use to characterize the as-cast and post-DSC microstructures of the alloys. The microstructures of AZ91D alloy show dendritic morphology both in as-cast and post-DSC microstructure. In the as-cast microstructure of AM60B alloys divorced eutectic microstructures were observed, however, the post-DSC microstructures were partially divorced.

For AZ91D and AM60B alloys the volume fraction of the eutectic increases with increasing cooling rate. In the case of AE44 alloy the volume fraction of the secondary phase increases with increasing cooling rates.

Using power law equation extrapolation of the transition temperatures and solidification enthalpies have been made to higher cooling rates based on the DSC slow cooling rate data. The calculated solidification enthalpies are in good agreement with available experimental data except for AE44 alloy. Moreover, calculated transition temperatures are consistent with the available experimental data.

## **5.2 Contributions**

- Extensive experimental work combined with thermodynamic calculations allowed thorough analysis of three potential magnesium alloys resulting in better understanding of the solidification behavior of the alloys.
- These results should prove to be a vital stepping stone for further research in magnesium alloy development or optimizing the casting procedure for magnesium alloys.

## **5.3 Recommendations for Future Work**

- ❖ X-ray Diffractometer (XRD) could be used to identify the phases that form at different cooling conditions.
- ❖ Scanning Electron Microscope (SEM) coupled with Electron Probe Micro Analysis (EPMA) could be used to obtain the detail analysis of the as-cast and post-DSC microstructures.

- ❖ Volume fraction of the different phases could be measured experimentally using image analyzing software and can be compared with the thermodynamic prediction.
- ❖ Finite difference method (FDM) or finite element method (FEM) could be used for further analysis of the solidification behavior.

## References

- [1] H. Watarai: Trend of research and development for magnesium alloys- reducing the weight of structural materials in motor vehicles. *Science & Technology Trends*. Quarterly review no. 18, 2006, pp.84-97.
- [2] E. Aghion, B. Bronfin and D. Eliezer: The role of the magnesium industry in protecting the environment. *Journal of Materials Processing Technology*. Vol. 117, 2001, pp. 381-385.
- [3] H. Friedrich and S. Schumann: Research for a new age of magnesium in the automotive industry. *Journal of Materials Processing Technology*. Vol. 117, 2001, pp. 276-281.
- [4] B.L. Mordike and T. Ebert: Magnesium Properties-application-potential. *Materials Science and Engineering*. Vol. A302, 2001, pp. 37-45.
- [5] E. Aghion and B. Bronfin: Magnesium alloys development towards the 21<sup>st</sup> century. *Materials Science Forum*. Vol.350-351, 2000, pp.19-28.
- [6] A. Wrigley: Automakers going heavy on use of light magnesium. *American Metals Marketplace*, August, 2001.
- [7] S. Sugimoto: 53<sup>rd</sup> Annual Magnesium Congress (Ube City, Japan, 1996),pp.38.
- [8] H.I. Laukli: High pressure die casting of aluminium and magnesium alloys. PhD thesis, Norwegian University of Science and Technology (NTNU), Trondheim, April, 2004.
- [9] M.M. Avedesian and H. Baker: Magnesium & Magnesium alloys. ASM International, 1999.
- [10] I. J. Polmear: Magnesium Alloys and Applications. *Materials Science and Technology*. vol.10,1994, pp. 1-16.
- [11] B. Cantor: Differential scanning calorimetry and the advanced solidification processing of metals and alloys. *Journal of Thermal Analysis*. vol. 42, 1994, pp. 647-665.

- [12] R. Schmid-Fetzer and J. Grobner: Focused Development of Magnesium Alloys Using the Calphad Approach. *Advanced Engineering Materials*. vol. 3, No. 12., 2001, pp. 947-961.
- [13] M Piche, A.D. pelton and C. Brochu: A thermodynamic database or magnesium alloys. *Proceedings of the mineral, metals and materials society (TMS)*, 2003, pp. 295-298.
- [14] Metals Handbook, 10th edn., Vol. 2 (1990) Properties and selection: nonferrous alloys and special-purpose materials. ASM International, Materials Park, OH, USA
- [15] H.E. Friedrich and B.L. Mordike: Magnesium Technology – metallurgy, design data and application. Springer-verlag, Berlin Heidelberg 2006.
- [16] J.S. Waltrip: Fresh Look at Some Old Magnesium Diecasting Alloys for elevated Temperature Applications. *Proceedings of 47th Annual World Magnesium Conf.* IMA, Cannes, May, 1990, pp.124–129
- [17] W.E. Mercer: Magnesium Die cast Alloys for Elevated Temperature Applications, *SAE 900788*, 1990.
- [18] C. Bale, A.D. Pelton and W. Thompson, Factsage Thermochemical Software and Databases, <http://www.crct.polymtl.ca>, 2008.
- [19] M Al-Jarrah: Thermodynamic Modelling and Experimental Investigation of the Mg-Al-Ca-Sr System. PhD Thesis, Concordia University, Montreal, Quebec, 2008.
- [20] A.K. Dahle, Y.C. Lee, M.D. Nave, P.L. Schaffer and D.H. StJohn: Development of the as-cast microstructure in magnesium-aluminum alloys. *Journals of Light Metals*. Vol. 1, 2001, pp. 61-72.
- [21] A. Beck: The Technology of Magnesium and its Alloys. FA Hughes & Co. Ltd, London, UK, 1940.

- [22] Y.C. Lee, A.K. Dahle, D.H. StJohn: Grain refinement of magnesium. *Proceedings of the minerals, metals and materials society (TMS)*, 2000, pp. 211-218
- [23] N Woldman: Magnesium Casting. Magnesium, ASM International, 1946.
- [24] K.U. Kainer: Magnesium-Alloy and Technologies. Wilet-VCH GmbH & Co. 2003.
- [25] P. Bakke and H. Westengen: The role of rare earth elements in structure and property control of magnesium die casting alloys. *Magnesium Technology 2005*, 291-296.
- [26] S.G. Lee, G.R. Patel, A.M. Gokhale, S. Sreerangathan and M.F. Horstemeyer: Quantitative fractographic analysis of variability in the tensile ductility of high-pressure die-cast AE44 Mg-alloy. *Materials Science and Engineering*. vol. A 427, 2006, pp. 255-262.
- [27] A. Luo: Understanding the solidification of magnesium alloys. *Proceedings of the third international magnesium conference*, 1997, pp. 449-464.
- [28] Metals Handbook, 1988, 9th edn., Vol. 15, Casting. ASM International, Materials Park, OH, USA
- [29] D.H. StJohn, A.K. Dahle, T. Abbott, M.D. Nave and M. Qian: Solidification of cast magnesium alloys. *Proceedings of the minerals, metals and materials society (TMS)*, 2003, pp. 95-100.
- [30] Y.W. Riddle and M.M. Makhlof: Characterizing Solidification by Non-Equilibrium Thermal analysis. *Proceedings of the minerals, metals and materials society (TMS)*, 2003, pp. 101-106.
- [31] S. Gowri and F.H. Samuel: Effect of cooling rate on the solidification behavior of Al-7 pct Si-SiCp metal-matrix composites. *Metallurgical Transaction*. Vol. 23A, 1992, pp.3369-3376.
- [32] W.D. Fei and S.B. Kang: Effect of cooling rate on solidification process in Al-Mg-Si alloy. *Journal of Materials Science Letters*. Vol. 14, 1995, pp. 1795-1797.

- [33] J. Dobrovská, S. Dočekalová and B. Smetana: Study of cooling rate effect on transformation temperatures in the course of IN 738LC solidification. *Acta Metallurgica Slovaca*. Vol.13, 2007, 539 – 545.
- [34] A. Lindemann, J. Schmidt, M. Todte and T. Zeuner: Thermal analytical investigations of the magnesium alloys AM60 and AZ91 including the melting range. *Thermochimica Acta*. Vol. 382, 2002, pp. 269-275.
- [35] S. Thompson, S.L. Cockcroft and M.A. Wells: Effect of cooling rate on solidification characteristics of aluminum alloy AA5182. *Materials Science and Technology*. Vol. 20, 2004, pp. 497-504.
- [36] M.B. Djurdjevic, J.H. Sokolowski, W.T. Kierkus and G. Byczynski: The effect of chemistry and cooling rate on the latent heat released during the solidification of the 3XX series of aluminum alloys. *Materials Science Forum*. vol. 539-543, 2007, pp. 299-304.
- [37] Z.Q. kuang, J.X. Zhang, X.H. Zhang, K.F. Liang and P.C.W. Fung: Scaling behaviours in the thermoelastic martensitic transformation of Co. *Solid State Communications*. Vol. 114, 2000, pp. 231-235.
- [38] M.D. Nave, A.K. Dahle and D.H. StJohn: Eutectic growth morphologies in magnesium-aluminium alloys. *Proceedings of the minerals, metals and materials society (TMS)*, 2000, pp. 233-242.
- [39] Lee P. Barber: Characterization of the Solidification Behavior and Resultant Microstructures of Magnesium-Aluminum Alloys. PhD Thesis, Worcester Polytechnic Institute. December, 2004.
- [40] A.K. Dahle, Y.C. Lee, M.D. Nave, P.L. Schaffer and D.H. StJohn: Development of the as-cast microstructure in magnesium – aluminum alloys. *Journal of Light Metals*. 2001, pp. 61-72

- [41] Hydro Magnesium (1996). Die cast magnesium alloys. Data Sheet.
- [42] S. Barbagallo, H.I. Laukli, O. Lohne and E. Cerri: Divorced eutectic in a HPDC magnesium alloy. *Journal of alloys and compounds*, no. 378 , 2004, pp. 226-232.
- [43] M.D. Nave, A.K. Dahle and D.H. StJohn: The effect of solidification rate on the structure of magnesium-aluminium eutectic grains. *International journal cast metals res.*, no. 13, 2000, pp. 1-7.
- [44] P. Bassani, E. Gariboldi and A. Tuissi: Calorimetric analysis of AM60 magnesium alloy. *Journal of Thermal Analysis and Calorimetry*, vol 80, 2005, pp. 739-747.
- [45] Q. Han, E.A. Kenic, S.R. agnew and S. Viswanathan: Solidification behavior of commercial magnesium alloys. *Proceedings of the mineral, metals and materials society (TMS)*, 2001, pp. 81-86.
- [46] Y.W. Riddle, L.P. Barber and M.M. Makhlof: Characterization of Mg alloy solidification and as-cast microstructure. *Proceedings of the mineral, metals and materials society (TMS)*, 2004, pp. 203-208.
- [47] M.A. Parvez, E. Essadiqi and M. Medraj: Thermal analytical investigations of ternary Mg-Al-Sr system by DSC. *CSME 2004 Forum*. pp. 829-838.
- [48] [www.safety-s2s.eu/](http://www.safety-s2s.eu/) dated: 20-04-2009
- [49] M.A. Parvez: Experimental Investigation of the Ternary Mg-Al-Sr System. Masters Thesis, Concordia University, Montreal Quebec, 2004.
- [50] D. Larouche, C. Laroche and M. Bouchard: Analysis of differential scanning calorimetric measurement on a binary aluminum alloy. *Acta Materialia*. Vol. 51, 2003, pp. 2161-2170.
- [51] G.W.H. Hohne, W.F. Hemminger and H.-J. Flammersheim: Differential Scanning Calorimetry. Second Edition, Springer 2003.

- [52] W.J. Boettinger, U.R. Kattner, K.-W. Moon and J.H. Perepezko: DTA and Heat-flux DSC Measurements of Alloy Melting and Freezing. Practice guide, NIST, November 2006.
- [53] D. Mirkovic, J. Grobner and R. Schmid-Fetzer: Solidification Curves of AZ-Magnesium Alloys determined by DSC Experiments and Heat-transfer Model (DSC-HTM). *Magnesium-Proceedings of the 6<sup>th</sup> Int. Conference Magnesium Alloys and their Application 2003*. pp 842-847.
- [54] S.W. Chen and C.C. Huang: Solidification curves of Al-Cu, Al-Mg and Al-Cu-Mg Alloys. *Acta mater.* 1996,vol 44 no 5, pp 1955-1965.
- [55] M. Ohno, D. Mirkovic and R. Schmid-Hetzer: On liquidus and solidus temperature in AZ and AM alloys. *Proceedings of the mineral, metals and materials society (TMS)*, 2006, pp. 129-132.
- [56] M. Ohno, D. Mirkovic and R. Schmid-Hetzer: Liquidus and solidus temperature of Mg-rich Mg-Al-Mn-Zn alloys. *Acta Materials*. Vol.54, 2006, pp. 3883-3891.
- [57] L.Y. Wei and G.L. Dunlop: The solidification behavior of Mg-Al-rare earth alloys. *Journal of Alloy and Compounds*. Vol.232, 1996, pp. 264-268.
- [58] A. Kietbus: Microstructure of AE44 magnesium alloy before and after hot-chamber die casting. *Journal of Achievement in Materials and Manufacturing Engineering*. Vol. 20, issues 1-2, 2007, pp.459-462.
- [59] T. Rzychon and A. Kietbus: The influence of the wall thickness on the microstructure of HPDC alloy. *Archives of Materials Science and Engineering*. Vol. 28, issues 8, 2007, pp.471-474.
- [60] N.D. Saddock, A. Suzuki, K. Wu, S.C. Wildy, Y.A. Chang, T.M. Pollock and J.W. Jones: Solidification and microstructure of Mg-Al-(Ca,Sr,Ce,La) ternary alloys. *Proceedings of the mineral, metals and materials society (TMS)*, 2005, pp. 121-126.

- [61] M.B. Djurdjevic, W.T. Kierkus, R.E. Liliac and J.H. Sokolowski: Extended analysis of cooling curves. *Light Metals 2002 Metaux Legers*. Pp.351-365.
- [62] M.B. Djurdjevic, J. Chen and J.H. Sokolowski: A novel approach for the calculation of latent heat of solidification for multi-component aluminium alloys. *AFS Transactions 2003*. American Foundry Society, Des Plaines IL USA.2003, pp.205-215.
- [63] G. Levi, S. Avraham, A. Zilberov and M. Bamberger: Solidification solution treatment and age hardening of a Mg-1.6wt% Ca-3.2wt%Zn alloy. *Acta Materialia*. Vol. 54, 2006, pp. 523-530.
- [64] N. Saunders, X.Li, A.P. Miodownik and J.P. Schille: Modeling of the thermo-physical and physical properties for solidification of magnesium alloys. *Proceedings of the mineral, metals and materials society (TMS)*, 2003, pp. 135-139.
- [65] E. Charrier, E.L. Charsley, P.G. Laye, H.M. Markham, B. Berger and T.T. Griffiths: Determination of the temperature and enthalpy of the solid-solid phase transition of caesium nitrate by differential scanning calorimetry. *Thermochimica Acta*. Vol. 445, 2006, pp.36-39.
- [66] J.X. Zhang, F. Zhong and G.G. Siu: The scanning-rate dependence of energy dissipation in first-order phase transition of solids. *Solid State Communication*. Vol. 97, no. 10, 1996, pp. 847-850.
- [67] V. Raghavan: Some characteristics of first-order phase transformations. *Bull. Mater. Science*. Vol. 1, no. 3& 4, Dec. 1979, pp. 171-179.
- [68] J. Liu and J.X. Zhang: Temperature dependent kinetics of martensitic transformation in MnCu alloy. *Solid State Communication*. Vol. 98, no. 6, 1996, pp. 539-542.
- [69] Z.Q. kuang, J.X. Zhang, X.H. Zhang, K.F. Liang and P.C.W. Fung: Latent heat in the thermoelastic martensitic transformation of Co. *Scripta Mater*. Vol. 42, 2000, pp. 795-799.

- [70] N. Reade and J.H. Sokolowski; University of Windsor, Canada: Personal communication.
- [71] GH Gulliver: *J Inst Metals*. 1913;v. 9, pp.120–57.
- [72] E. Z. Scheil: *Metallkd* 1942; v. 34, pp.70–72.
- [73] Yang-Zi Zhao, Yun-He Zhao, Qian Li, Shuang-Lin Chen, Jie-Yu Zhang and Kuo-Chih Chou: Effects of step size and cut-off limit of residual liquid amount on solidification simulation of Al–Mg–Zn system with Scheil model. *Intermetallics*. v 17 (2009) pp. 491- 495.
- [74] B. Dutta and M. Rettenmayr: Effect of cooling rate on the solidification behavior of Al-Fe-Si alloys. *Materials Science and Engineering*. A283 (2000), pp: 218-224.
- [75] Y.C. Guan and W. Zhou: Calorimetric analysis of AZ91D magnesium alloy. *Materials Leter*. v. 62 (2008), pp: 4494-4496.
- [76] J. Mahamoudi and H. Fredriksson: Thermal analysis of copper-tin alloys during rapid solidification. *Journal of Materials Science*. V.35 (2000), pp. 4977-4987.